5-2010

Characterization of Contaminant and Biomass-Derived Organic Matter in Sediments from the Lower Passaic River, New Jersey, USA

Nicole Michelle Bujalski
Montclair State University

MONTCLAIR STATE UNIVERSITY

Characterization of Contaminant and Biomass-Derived Organic Matter in Sediments from the Lower Passaic River, New Jersey, USA

by

NICOLE MICHELLE BUJALSKI

A Master's Thesis Submitted to the Faculty of

Montclair State University

In Partial Fulfillment of the Requirements

For the Degree of

Master of Science

May 2010

School College of Science and Mathematics

Department Earth and Environmental Studies

[redacted]

Dean Dr. Robert S. Prezant

(May 5, 2010)

Thesis Committee:

[redacted]

Thesis Sponsor Dr. Michael A. Kruge

[redacted]

Committee Member Dr. Huan E. Feng

[redacted]

Committee Member Dr. Joshua C. Galster

[redacted]

Department Chair Dr. Duke U. Ophori

CHARACTERIZATION OF CONTAMINANT AND BIOMASS-DERIVED ORGANIC MATTER IN SEDIMENTS FROM THE LOWER PASSAIC RIVER, NEW JERSEY, USA

A THESIS

Submitted in partial fulfillment of the requirements

for the degree of

Master of Science, Geoscience

by

NICOLE MICHELLE BUJALSKI

Montclair State University

Montclair, NJ

2010

ABSTRACT

CHARACTERIZATION OF CONTAMINANT AND BIOMASS-DERIVED ORGANIC MATTER IN SEDIMENTS FROM THE LOWER PASSAIC RIVER, NEW JERSEY, USA

By Nicole Michelle Bujalski

The lower Passaic River has been heavily contaminated during the twentieth century due to the industrial activity within its watershed. The geochemistry of four deep cores was explored using an environmental forensics approach. Pyrolysis gas-chromatography/mass spectrometry (Py-GC/MS) and grain size analysis was performed in conjunction with radiometric analysis to understand the sediment and contaminant transport patterns. The distinctive molecular finger prints were identified by employing chromatogram fingerprints, polycyclic aromatic hydrocarbon distribution, principal component analysis, and chemostratigraphy. Radiometric analysis and observations of chlorinated contaminant patterns allowed for average sample depths to be correlated to approximate ages. Additionally three distinct zones were observed in all cores including a disturbed ^{137}Cs layer mid core, and a relatively undisturbed profile in the upper and deeper section of the cores. The main focus of the geochemistry was on organic material, including more precisely the investigation of possible anthropogenic hydrocarbon sources by identifying petrogenic and pyrogenic signatures and observing trends in biomass input. Two trends emerged with respect to the former. The two cores were observed to have zones with a relatively natural signature and zones with a mixed combustion/petroleum signature and two cores were observed to contain separate zones which were impacted more heavily by petrogenic sources or pyrogenic sources. Grain size analysis confirmed that the majority of the samples were comprised of silt, but a sand

lens was observed around 5 meters depth. This sand lens correlates with polycyclic aromatic hydrocarbon concentrations and may reflect a subsurface migration of coal tar, possibly from a nearby site of a former manufactured gas plant. Biomass relationships were evaluated using the VGI ratio, which compares terrestrial to aquatic inputs in order to observe background trends in sediment transport and erosional/depositional events. The general observation is an oscillating pattern displaying the system significantly impacted during flood events.

ACKNOWLEDGEMENTS

I would like to acknowledge Malcolm Pirnie, Inc. for donating the cores analyzed in this work to the Passaic River Institute at Montclair State University and more specifically Edward Garvey and Juliana Atmadja for providing data and helpful comments. Additionally, I would like to recognize the Passaic River Institute for granting access to the cores used in this project and for providing images. Sandra Passchier has contributed to this work through her much appreciated advice and assistance with grain size analysis. The insights which Eric Stern added to this work should also be recognized.

The essential academic expertise of my committee members Josh Galster and Huan Feng has greatly improved this manuscript and I am extremely grateful for all of their invaluable input.

I would like to thank my friends, colleagues, and family who have greatly supported this effort indirectly. In particular I would like to express my gratitude to my mother, my father, my brother Philip, and my beloved sister Natalie.

I dedicate this work to my major advisor Michael Kruge for his earnest commitment to my education. He has pushed me to do my best in the most constructive way. Without his superior guidance and efforts I would not be the person I am today. Most importantly he has always believed in me and in doing so encouraged me to reach for the sky. Thank you for all that you do.

Table of Contents

List of Figures:

Tables:

Introduction

The lower Passaic River comprises an extremely complex urban estuarine system. Tidal exchange, navigational dredging, and changing sedimentation rates contribute to the dynamics of the system, along with major, heterogeneous contaminant loadings. Shipping activities, urban runoff, airfall combustion debris, sewer outfalls, and additional point sources all contribute to its extraordinarily high contaminant burden. The river is part of the New York/New Jersey harbor estuary, important geographically due to its proximity to dense urban populations and high volume of commodity transport. These human activities have impacted the river, and there are currently fish and shellfish advisories in place for the lower Passaic due to extremely degraded water quality. Recognizing this severe degradation, i the lower Passaic was added to the national priorities list by the United States Environmental Protection Agency (USEPA) in 1989.

In an effort to create an effective remediation management plan, the USEPA and its contractor Malcolm Pirnie, Inc. have invested in an extensive background research program, including investigation of heavy metals, 2,3,7,8-–tetrachlorodibenzo-*p*-dioxin (TCDD), polychlorinated biphenyls (PCBs), dichlorodiphenyltrichloroethane (DDT), and polycyclic aromatic hydrocarbons (PAHs) (Malcolm Pirnie, Inc. 2006, 2007, USEPA 1995), as part of the Lower Passaic River Restoration Program (LPRRP). Additional federal agencies and university laboratories have also taken part in these research efforts. However there has been less work done on hydrocarbon contaminants, which can make up a significant portion of the contaminant load. To help remedy this deficiency, this work focuses on petroleum biomarkers and source specific PAH investigation, as well as biomass and sewage inputs.

1. Background

1.1 Geologic History

The Newark Basin was formed during the breakup of the supercontinent of Pangaea in the late Triassic Period. At the beginning of the breakup, the Atlantic Ocean was formed by rifting between the North American and African plates. However, the extension of the Newark Basin was aborted, creating a half graben which filled with fluvial sediments eroded from large footwalls of the border faults, particularly the Ramapo Fault on the western side (Tankard and Balkwill 2003). This sediment compacted to create the Passaic Formation (Fig. 1) which underlies much of today's Passaic River watershed. The Passaic Formation is comprised of predominantly of siltstone, sandstone, and shale (Dalton et al. 1999, USEPA 1995).

The impact of Pleistocene glaciation is still apparent in the Passaic watershed. During the most recent ice age, large glaciers formed and retreated at least three times in New Jersey. Twenty one thousand years ago, during the third and latest period of glaciation known as the late Wisconsinan substage, melt water formed proglacial Lake Passaic. The glaciations deposited till over bedrock in the Passaic River Basin and cut lowlands which later became drainage areas including rivers and wetlands. The Passaic River was initially formed by the drainage of the former glacial Lake Passaic. This origin makes the Passaic susceptible to flooding in present times (United States Geological Survey 2003).

1.2 Historical Background: Changing Landscapes

The Lenni Lenape Native American Indians were the first known peoples to inhabit the region around the Passaic River. It is estimated that these people were present in the area for centuries before the arrival of Europeans. It is presumable that the environment was minimally impacted by the hunting, fishing and farming of the Lenape peoples. The Newark and Hackensack meadows still consisted of a diverse area of wetlands surrounding the lower Passaic river before the arrival of Europeans in the mid 1660s (Marshall 2005).

European settlers as well as Native Americans used resources from the meadowlands such as oysters, fish, water fowl, and small mammals until recently, when it became a health concern to continue the practice. Presently the area harbors only pollutant-tolerant species and the general ecologic diversity has dwindled, including the loss of extensive cedar forests which can no longer survive the increasingly saline conditions. The salinity of the meadowlands has been altered by both natural and anthropogenic impacts. The slow rise in sea level has caused an increase in saline waters reaching further inland. The construction of dams began on the Passaic in the late 1660s, reducing the flow in order to supply drinking water (Marshall 2005).

Public opinion was negative towards wetlands in general from the 1660s until the 1960s. The general attitude perceived wetlands to be useless land which compromised public health. The solution was 'reclaiming' the areas by altering the landscape to better suit human needs. This translated to creating dry land above sea level by combinations of carving dikes and ditches for drainage and adding dredged material, municipal waste, and construction debris to 'permanently' elevate the land. Various urban infrastructural features in the 20th century were created this way, including the Newark/Elizabeth sea

port (1914) , Newark Liberty International Airport (1927), the New Jersey Turnpike (1952), and other roadways (Marshall 2005).

During the late 1960s and early 1970s public opinion of wetlands was altered. In 1968 the Hackensack Meadowlands Development Act was written to protect the remaining wetlands. The Meadowlands boundary was defined to include 83 km^2, only 33 km^2 of which are still wetlands. Under the administration of Governor Brendan Byrne, elected in 1972, the development of the remaining wetlands slowed and eventually halted, due in part to his support of stricter environmental protection laws (Marshall 2005).

1.3 Early Industry along the Passaic

In 1624 New Amsterdam was founded by the Dutch West India Company and shortly thereafter the Passaic and Hackensack rivers were used as highways for fur trading with the Native Americans. Once population allowed, merchants established landings along the rivers. From the mid 1700s until the age of the railroad, the Passaic was used to ship agricultural products into Manhattan and in return, lumber, coal, liquor, and manufactured goods were imported inland via the river and its tributaries (Fig. 2). Newark harbor began its expansion in the late nineteenth century as the Port of New York became increasingly overwhelmed with traffic. At this time shipyards and ocean terminals appeared along the Passaic, with additional routes for cargo provided by inland bound railroads (Olsen 2008).

The Great Falls of the Passaic, located in Paterson (NJ) are a historical landmark for good reason. In 1792 Alexander Hamilton commissioned the construction of a water

powered system at the site of the great falls. Paterson thus became one of America's very first major manufacturing cities. The industries which utilized the hydropower of the falls were textiles, paper, and machinery (Historic American Engineering Record, Office of Archeology and Historic Preservation, National Park Service 1973).

Early coal gasification processes were developed by the mid 1800s along the Passaic. This is also when the attendant byproduct coal tar first began to contaminate the river. Coal was also falling off barges by the 1920s when it was unloaded at Passaic River docks en route to gasworks in Newark. The Paterson Gas Light Company and the Newark Gas Light Company began operations in 1847. The People's Light and Power Company also installed coal-fired electrical generators on the banks of the Passaic in Newark. The Harrison Gas Works began burning coal on the Passaic in 1926 and became a successful coke plant (Olsen 2008). Chemicals, paints, and pigments were manufactured along the banks of the Passaic as early as 1850 and by 1950 paint and pigment manufacturers numbered more than 130 in New Jersey (Dinkins and Tice 1998).

Companies which manufactured pesticides and herbicides also took advantage of this prime real-estate and established themselves along the lower Passaic. As a result of their manufacturing byproducts, large quantities of toxins contaminated the river. A prime example is the Diamond Alkali site (located on Lister Ave. in Newark, NJ), which manufactured Agent Orange during the Vietnam Conflict (USEPA 1994). During a comprehensive study of the area, Unites States Army Corps of Engineers (USACE) , USEPA, and the private sector have previously detected high concentration of contaminants including distinctively the human carcinogen 2,3,7,8-tetrachlorodibenzo-*p*-

dioxin (TCDD) and heavy metals in lower Passaic River sediments (Malcolm Pirnie, Inc. 2006). As a result, this site was added to the Superfund National Priorities List in 1984.

1.4 Combined Sewer Overflow (CSO) and Sewerage History

Sewage effluent began to be a problem as early as 1894, when it was thought that up to one third of the river flow was raw sewage. In 1902 the Passaic Valley Sewerage Commission (PVSC) was formed as an agency of the state by a special act of the legislature, to reduce pollution of the Passaic River and its tributaries. In 1924 a trunk sewer line was completed in order to serve 22 municipalities and 1 million people (discharging at Upper New York Bay) to reduce the amount of raw sewage directly discharged to the Passaic River. In 1937 the PVSC built a primary treatment facility at the terminal of the main trunk line and finally in the 1950s industrial facilities were connected to the sewer line. Many materials are present in CSO effluent that are detrimental to human health, including high levels of suspended solids, microbial pathogens, heavy metals (including mercury), floatables, nutrients (notably nitrogen and phosphorous), oil, and grease. These compounds come from both residential/industrial waste streams and storm water (Shear et al. 1996, Iannuzzi et al. 1997). Therefore, CSOs are known to have a major impact on water quality in urban areas. EPA's National CSO Control Strategy implemented in 1989 included restricting CSO discharge to wet weather conditions only and additionally required those discharges to be in compliance with Clean Water Act regulations.

Despite the EPA's National CSO Control Strategy, sewage discharge is still a problem today. Currently the PVSC operates seventy-three CSO outfalls in the lower

Passaic and thirty-six CSO outfalls below the Second River confluence (Fig. 3). Half of the CSOs are expected to overflow during at least fifty percent of the rainfall events. The PVSC found that overflows generally occurred within 15 to 20 minutes after rainfall intensity exceeds 1 mm h^{-1} (Sharp 1996). This is an ongoing source of contamination, and has been affecting the system since the Industrial Revolution.

1.5 Navigational Dredging History

Prior to the early twentieth century the Passaic River was a relatively shallow estuarine system. With the growing of industry and population in Newark, it became desirable to open the Passaic to larger commercial vessels, joining the city to the industry already booming in Newark Bay. Figure 3 shows the federal navigation channel (USACE 2008). Table 1 provides a thorough history of all recorded dredging operations from the USACE 2008 report. In short, in 1874 the USACE first dredged the river and in 1884, the lower 8 km of the river was deepened to 3 m. Until the 1920s dredging maintenance was steady, thereafter most removal occurred only in the lower 3 km (USACE, New York District 2008).

The grain size of deposited sediment varies along the entirety of the river. Above RK 13 the formerly dredged channel was narrower, leading to a higher energy environment which could transport coarser grained material. Conversely, below RK 13 the channel was wider leading to the deposition of finer grained sediment. This concept was validated by correlating cross-sectional area and grain size data i.e., a smaller

channel cross sectional area lent itself to deposition of coarser material Malcolm Pirnie, Inc. 2006, 2007).

Tidal influence and sediment resuspension further contribute to variations and complexity of the sediment accumulation rate. Sediments and adsorbed contaminants are thought to be constantly reworked and homogenized via tidal mixing at least up to RK 19 as the salt water front advances upstream twice a day with the tide (Malcolm Pirnie, Inc. 2006, 2007).

1.6 Current Conditions

Land use along the lower Passaic has been primarily industrial from RK 11 downriver to the mouth (Fig. 8). The materials produced and required by these industries also comprised the majority of the freight formerly transported on the river itself. In brief, transportation on the lower Passaic has been dominated by petroleum companies since the 1980s, most notably in the lower 3 km: Motiva, Stratus, Hess, Sunoco and Getty. This is in part due to the limitations on vessel transport on the Passaic. Additional active industries in 2008 include PVSC which transports primarily sewage sludge, Darling International which transports primarily animal lard and sodium hydroxide (during 2005-2006), and General Chemical which transports primarily sulfuric acid/oleum and ethyl alcohol. A descriptive berth by berth analysis is included in the USACE 2008 report.

Deepening of the channel for navigation creates an unstable environment which can lead to conditions of increased rates of sediment deposition both from upstream and the shoals adjacent to the channel. During flood events this tendency can be exacerbated. Regardless of the mechanism driving the deposition, over time without channel

maintenance, thick beds accumulated. This deposition occurred around the same time that many contaminants were entering the system, creating major accumulations of contaminated material (Malcolm Pirnie, Inc. 2007, 2006). As of 2009 the consumption of all fish and shellfish is prohibited from the tidal Passaic River (New Jersey Department of Environmental Protection 2009).

2. Methods

2.1 Sampling

As part of the Lower Passaic River Restoration Project, Malcolm Pirnie Inc., a nationwide environmental consulting firm, collected sediment cores in triplicate from the lower Passaic in September, 2005 by Vibracoring and ultimately donated the replicates to the Passaic River Institute at Montclair State University. Four cores (5A, 7A, 9A, 10A) ranging from approximately 4 to 7 m long were employed in this study (Table 3, Figs. 11, 12). Malcolm Pirnie had divided one of the replicates (the "A" series) into sub-samples ("slices") covering depth intervals ranging from 4 to 20 cm, placing the wet samples in glass jars and freezing them. The Passaic River Institute received these samples in the frozen state. Samples (Tables 4-7) were thawed, dried overnight in a Fisher Scientific Isotemp Oven at 35 °C and ground using a mortar and pestle to prep for pyrolysis.

2.2 Grain Size Analysis

Sediment granulometrywas determined using a Particle Mastersizer 2000. The sample was gravimetrically sieved to remove anything larger than 2000μm in order to protect the instrument. Approximately 100 mg of sample were soaked overnight with 100 ml hydrogen peroxide (30%) to remove the organic material. Sodium pyrophosphate ($Na_4P_2O_7 \cdot 10H_2O$) was added to act as an anti-flocculating agent directly before the sample was boiled for approximately 10 minutes to ensure the removal of all remaining organic material. The sample was then run on the instrument using the standard settings for sediments (Passchier, 2005). The Malvern Mastersizer 2000 software reports volume percent of twenty-six particle sizes ranges from 0.24 to 2000 μm.

2.3 Radionuclide and chlorinated compound analysis

The Lower Passaic River Restoration Project placed radiometric and chlorinated compound data for the subject cores in the public domain (LPRRP, 2008). These include raw data from the isotopic analysis of ^{137}Cs, ^{210}Po (surrogate for ^{210}Pb, except for Core 5A wherein ^{210}Pb is provided) , total PCB concentrations, and total TCDD concentration for cores 7A and 9A.

2.4 Pyrolysis – Gas Chromatography/Mass Spectrometry (Py-GC/MS)

Measured amounts (several mg) of the ground samples were loaded into a quartz tube containing glass wool. Five µl of an internal standard solution of perdeuterated PAHs (naphthalene ($C_{10}D_8$) 4.9 ng/µl, anthracene ($C_{14}D_{10}$) 5.4 ng/µl, pyrene ($C_{16}D_{10}$) 4.9 ng/µl, Chrysene ($C_{18}D_{12}$) 2.2 ng/µl in hexane) was added to the glass wool with a syringe prior to injection.

Samples were analyzed using a CDS 1500 pyroprobe (operating at 610 °C for 20 seconds) coupled to a Thermo Finnigan Focus DSQ GC/MS instrument containing a 30 m J&W Scientific DB-1MS column (0.25mm I.D., film thickness 0.25 µm). The GC program was operated for 5 minutes at 50 °C followed by increments of 5 °C increase per minute until reaching 300 °C. The temperature was isothermal for the 5 remaining minutes. The MS was operated in full scan (50-550 Da, 1.08 scans per second, 70eV ionization voltage) for all data analyzed in this work.

Absolute quantification was not executed; rather comparative semi-quantitation was accomplished by reference to the internal deuterated standards described aboveand Agilent software (MSD ChemStation Data Analysis E.02.00.493). Correction of all raw data was performed using previously determined mass spectral response factors unique to

each compound. These values have been normalized to the maximum peak area in each sample. Quantitated compounds are listed in Table 2.

2.5 Multivariate Analysis

With such a large number of variables (138 compounds and groups of compounds determined by Py-GC/MS) it was expedient to use principal components analysis (PCA) as a data exploration tool. Prior to PCA, all data values below the instrumental detection limit of approximately 10,000 corrected area counts were replaced with a random integer between 1,000 and 10,000. The dataset was then further prepared using logratio transformation and autoscaling (Yunker and Macdonald, 2003; Blackledge, 2007; Varmuza and Filzmoser, 2009). To accomplish this, the geometric mean of all values was obtained for each sample, by taking the arithmetic mean of the base 10 logarithms of the data points, then raising the arithmetic mean to power of 10. Then the base 10 logarithm of the ratio of the corrected values to the geometric mean was computed, generating the "logratio". The values were then autoscaled by subtracting the mean of all values of a particular compound in all samples from the logratio values, then dividing by the standard deviation of all the values for this compound. Principal component analysis was performed on the logratio-transformed, autoscaled Py-GC/MS data using JMP version 7.0 software.

2.6 Vinylguaiacol/Indole (VGI) Ratio

The Vinylguaiacol/Indole (VGI) ratio is a parameter recently proposed (Micić et al., in press) to assess relative terrestrial vs. aquatic biomass contributions to sediments. Vinylguaiacol is typically one of the most abundant lignin pyrolysis products, thus a proxy for higher plant material, while indole is produced upon pyrolysis of the amino

acid tryptophan, thus a proxy for proteinaceous aquatic biomass (Micić et al., in press). Using Py-GC/MS data, the area of the uncorrected m/z 150 4-vinylguaiacol peak (VG) is divided by the uncorrected area of the m/z 117 indole peak (I) plus the area of the 4-vinylguaiacol peak to attain a numerical value constrained between zero and one (VGI = VG / (I + VG)).

3. Results and Discussion:

3.1 Sediment Age and Sedimentation Rate Estimation

Due to a lack of maintenance, the Passic River navigational channels began to fill with sediment once dredging ceased. Figure 4 displays average sedimentation rates per 400 m river segment. The sediment accumulation averages are based on 8 separate bathymetric surveys from years 1989 through 2004 and compared to radiometric data. Below river kilometer (RK) 11 the system experiences variability, but the lower section has overall higher sediment accumulation rates compared to zones upriver (Fig. 5). Below RK 3.2 the deposition rate is much higher probably due to the increased amount of dredging occurring in that area until 1983. The channel walls have also become sloped, most likely due to the changing state of unstable, oversteepened deep (6-9 m depending on RK) channels (Malcolm Pirnie, Inc, 2007, 2006).

^{137}Cs, ^{210}Pb, and ^{210}Po are often used to radiometrically date recent sediment cores. ^{210}Pb is the product of naturally occurring atmospheric fallout which has a half life of approximately 22 years. ^{210}Po occurs two steps down the decay chain from ^{210}Pb in the Uranium 238 series and has a half life of 138 days. Therefore the activity can be used to observe general chronostratigraphic trends in a sediment column. A logarithmically decreasing trend would be observed if the sediment was uniformly deposited and undisturbed. ^{137}Cs is a byproduct of atmospheric nuclear weapons testing and is not naturally occurring (Eby 2004). The majority of nuclear tests occurred during the 1950s and 1960s, with the Chernobyl accident occurring in 1986. In an undisturbed sediment profile the peak activity for ^{137}Cs would be expected to occur sometime between the 1950s and 1960s and a second peak in activity would be observed as a result of the

Chrnobyl accident. The extent of activity reflected for each event is also dependent on geographic location. In the United States the highest activity should be observed between 1954 and 1963 which are the years the USA performed the majority of atmospheric nuclear testing domestically.

In this work the three isotopes were used to observe general trends in depositional history and estimate approximate age ranges rather than assign definitive dates. The ^{137}Cs maximum is stretched from 1.25 – 3.25 meters in core 7A, and from 1.2 - 5.1 meters in core 9A (Fig. 6 A, B). This occurrence is also reflected in the log excess ^{210}Po results. This ^{210}Po trend is near vertical from approximately 1.25 – 3.25 meters in core 7A and from 1 – 5 meters in core 9A (Fig. 6 C, D). Cores 5A and 10A also have a disturbed ^{137}Cs window (0.75 – 2.75 m in Core 5A and 1.3 – 3.4 m in Core 10A) which correlates to the log excess ^{210}Po data in Core 10A and log excess ^{210}Pb in Core 5A (Fig. 7). ^{210}Pb data was available in place of ^{210}Po for core 5A only.

One interpretation of the radionuclide data is that during the period of peak ^{137}Cs deposition the sediment column was mixed in all cores resulting in a thick interval of sediment with high, yet diluted ^{137}Cs concentrations (Figs. 6, 7). These profiles suggest that relatively rapid sediment deposition occurred sometime between the mid 1950s through the mid 1960s. There are many natural and anthropogenic circumstances which further complicate interpretations. The Core 10 A site was last dredged in 1937, the Core 9A site was last dredged in 1946, while the navigation channel at site 7A and 5A was maintained in 1946, 1951, 1957, 1965, 1971, 1972, and 1983 (Table 1). This introduces two possible scenarios: first the dredging action may have disturbed the peak ^{137}Cs by removing sediment which contained high concentrations. This would be most likely to

have occurred in 5A and 7A given the dredging history. Second, as discussed in Section 1.5, Malcolm Pirnie, Inc. has previously found that after a dredging event higher than natural sedimentation rates can occur, possibly leading to the smearing observed in the radionuclide profiles (ref). Additionally two notably intense hurricanes affected the area, Diane in 1955 and Donna in 1960. The high flooding events occurring during that time could have lead to higher than average erosion and redeposition of sediment, coincidently during the years of maximum ^{137}Cs fallout.

PCBs and TCDD may similarly be used to constrain approximate sediment ages to peak areas within the cores. This application can only be applied to cores 7A and 9A since PCB and TCDD concentration data are only available for those cores. PCB production began in North America in 1930 and was banned by Congress in the United States in 1979. TCDD concentrations would have been highest from 1951 – 1969 which corresponds to the dates during which the Diamond Alkali Company was manufacturing herbicides (EPA 2008). Therefore approximate constrains can be assigned based on the chlorinated compound peaks to serve as an additional support if correlated with the radionuclide profiles. The spike in PCBs occurs in core 7A just above 3 meters and in core 9A as two consecutive spikes just below 3 meters and 5 meters (Fig. 6 (E, F)). TCDD concentrations reflect the same trend in both cores (Fig. 6 (G, H)) but occur slightly higher in 7A.

The sharpness of the 7A spike suggests that the depositional environment was different at the site of core 9A which produces two concentration spikes. It is possible that a second, deeper spike may exist at the core 7A site, but was not encountered because the coring did not go deep enough. However tidal mixing as well as dredging

operations can greatly affect the sediment column so this is only one possible interpretation. These sharp spikes may also have been a result of the two flood events mentioned above occurring within the time frame of the marker years,he later of which occurred soon after an important historical release of these compounds. In 1960 an explosion occurred at the Diamond Alkali Chemical Company, causing the release of many contaminants including these chlorinated compounds. Overall it is concluded that there are many possible causes, but it is evident from the profiles and history that the peak ^{137}Cs zones were certainly disturbed and remixed in all four cores. Furthurmore this zone represents a distinct area (termed herein the "Mid Section") which is affected and related to various anthropogenic inputs discussed below.

3.2 Sediment Grain Size Analysis:

The average volume weighted mean grain size for each sample in all four cores is plotted against depth in Figure 12. The majority of samples are below the silt/sand line (64 μm) particularly in cores 5A and 7A, which are closest to the mouth of the river (Figs. 5, 6). Core 9A and 10A are slightly coarser, especially near the surface, although most samples are still below the silt/sand line. All three cores (5A, 7A, and 9A) which reach a depth of 4.5 m dramatically coarsen at that point. Core 10A does not exhibit this trend, although it does begin to coarsen before it terminates less than 4 m in depth. Core 9A is the only core which penetrated beyond the sandy lens and fines again around 5.5 m. All samples consisted entirely of particles less than 2 millimeters except for the one sample in each of the three cores peaking around 4.5 m. In those three samples gravel was observed as approximately 5 – 10 % of the total sample. These three samples will be referred to as representing the sandy lens throughout this work.

A possible explanation for Cores 9A and 10A exhibiting a slightly coarser lithology is their geographical location comparatively upstream and on the bend of the river (Fig. 12). The sandy lens is an important change in lithology which will be compared to contaminant concentrations in consecutive sections.

3.3 Organic Geochemistry

3.3.1 Total Organic Carbon:

Total organic carbon (TOC) values are lowest in core 5A with the majority of the samples ranging from 3.5 – 5.0 %. As the location of the cores moves upstream, TOC content increases with the majority of the samples ranging between 5 and 10 %. TOC is correlated with grain size, as the three cores which approach the sandy lens demonstrate a marked decrease in TOC at that point (Fig. 13).

3.3.2. Molecular Organic Geochemistry

3.3.2.1 General Observations:

In this work pyrogram fingerprints, PAH ratio analysis, and comparisons of contaminant concentrations have been utilized in an environmental forensics approach to attempt further clarification of anthropogenic inputs. Furthermore the novel vinyl guaiacol to indole (VGI) ratio, along with sediment grain size and TOC data, has been utilized in an attempt to understand the natural inputs and transport systems affecting the area. Given the large data set generated, principal components analysis (PCA) was employed to tie together these diverse trends.

The raw mass chromatograms were evaluated for characterization of the pyrolyzates of all samples. In this work Core 7A chromatograms from (A) surface sample

01, 0.00 – 0.08 m depth segment; (B) sample 25, 3.00 – 3.15 m depth segment; (C) sample 37, 4.80 – 4.88 m depth segment are employed as representative examples. Core 7A was chosen because of the extensive public domain data available for it (LPRRP, 2008) and additionally it is located downstream of the former Diamond Alkali site and adjacent to a former manufactured gas plant and the Getty petroleum terminal (Fig. 7). Within Core 7A, the three samples were chosen because of their stratigraphic positions within the three distinctive zones delineated by the radiometric analysis (Fig. 10). The change in the compound distribution in the pyrolyzates from sample 01 down to sample 25 is gradual and persists until a depth of approximately 4.5 m, at which point, the distribution pattern typified by the pyrolyzate of sample 37 is evident, although it is not as pronounced in any other sample in the core. These three distinct zones were generally observed in all four cores.

Sample 01 (0.00 – 0.08 m) provides information on the surficial environment at the time of core extraction (September 2005). It is readily apparent from its total ion chromatogram (TIC) (Fig. 14 (A)) that this sample is characterized by the highest level of biomass input of the three examples shown. The evidence includes lignin pyrolysis products such as vinylguaiacol, vanillin, and cis iso-eugenol; cellulose markers including methylfurancarboxaldehyde; and aquatic biomass markers including indole (Saiz-Jimenez and de Leeuw, 1986; Peulvé et al., 1996). The general odd carbon number predominance of normal alkanes ($> C_{22}$) also suggests input from higher plants. (Killops and Killops 2005). This is to be expected of recently deposited samples since the material has had the least time to degrade. Elemental sulfur is also highest in this sample suggesting recent sewage input (Kruge and Permanyer 2004) or altered redox conditions

transforming either primary sulfates or sulfides. Parent PAH compounds do occur including benzo(a)anthracene and fluoranthene along with the biodegraded petroleum-derived unresolved complex mixture (UCM) indicating anthropogenic contamination.

Sample 25 (3.00 – 3.15 m) provides a representative example of the middle zone of the core (Fig. 14 (B)). Similar biomass markers are present in the pyrolyzate but are relatively less abundant than for sample 01. The petroleum biomarkers pristane and phytane are evident, along with a pronounced double UCM hump, indicating the presence of biodegraded petroleum products. PAH compounds are observed in higher variety and relative abundance than sample 01, including the parent compounds naphthalene, phenanthrene, anthracene, phenanthrene, pyrene, benzo[*a*]anthracene, chrysene, and a cluster from the benzopyrene group. In addition, the methylated PAHs such as dimethyl phenanthrenes are present. The polycyclic aromatic sulfur compounds (parent and alkylated dibenzothiophenes) are observed as well, which could derive from petroleum or coal sources. The phthalate was likely introduced in the laboratory during sample handling.

The pyrolyzate of sample 37 (Fig. 14 (C)) provides evidence for a case of extreme contamination by parent and alkyl PAHs. The next highest in abundance are multiple phthalates and elemental sulfur. Indole alone appears as the only significant biomass pyrolysis product in the total ion trace. These features indicate an overwhelming degree of anthropogenic input with a combustion signature.

The m/z 71 mass chromatograms provides offer a more detailed view of the normal and isoprenoid alkane and alkene distributions in the pyrolyzates (Fig.15 (A-C)). In sample 01 the odd predominance of normal alkanes can be more clearly observed,

especially C_{29} and C_{31}. The isoprenoid alkanes pristane and phytane, which are resistant to biodegradation, are present but in similar abundance to the normal alkanes, additionally confirming that little biodegradation has taken place (Fig. 15 (A)). The sample 25 pyrolyzate has a different signature on the m/z 71 trace (Fig. 15 (B)). Pristane and phytane are in high relative abundance while the odd carbon number predominance is less pronounced, indicating biodegraded petroleum products. In the pyrolyzate of sample 37 (Fig. 15 (C)), the normal alkanes are less important as they are harder to distinguish from the background compared to the previous two samples. The odd number normal alkane predominance is lower than both shallower samples and pristane and phytane are at approximately the same abundance as the normal alkanes. This signature is one of degraded biomass without the petroleum input present in sample 25.

The petroleum biomarkers of the hopane type are best seen on the m/z 191 trace. In Figure 16 (A-C) the general petroleum influence trend observed on the m/z 71 trace is supported. The sample 01 pyrolyzate exhibits some hopanes in relatively low abundance, while sample 25 displays a wider variety of hopanes in greater relative abundance, confirming a petroleum component. The sample 37 pyrolyzate contains no hopanes which can be observed above the detection limit.

Like the hopanes, the C_{27}-C_{29} steranes and diasteranes are biomarkers indicative of the presence of heavy petroleum fractions in the sediments. While they are clearly present, they occur in very low relative abundances in these sediment pyrolzates (Fig. 17).

3.3.2.2. PAH Distributions

The distribution of parent PAH compounds compared to their alkylated counterparts is an important diagnostic tool in environmental forensics. Strong parent PAH signatures represent "pyrogenic" (combustion-derived) sources while more alkylated PAH signatures usually indicate "petrogenic" (petroleum-derived) inputs (Yunker at al. 2002, Yan et al. 2004, Yan et al. 2006). Note the term "pyrogenic", which refers to the origin of the organic contaminants in the sediment, should not be confused with "pyrolysis" and "pyrolyzate" which refer to the Py-GC/MS analytical method employed in this study. These indicators will be assessed in detail in this section.
The first step is to observe the relative abundance in the composite chromatograms produced in Figures 18 through 21. The general trend observed is a high abundance of methylated PAH groups compared to parent compounds in the pyrolyzate of sample 25, low abundance of methylated PAH groups in sample 37, and an intermediate distribution for sample 01. This observation further supports the hypothesized petrogenic input to the middle zone of the core and pyrogenic input to the lower zone of the core. The distinction is particularly clear for the two and three ring PAHs, while less pronounced for the 4 ring compounds. The five ring benzopyrene group compounds displayed in Figure 22 (A-C) are plotted on the m/z 252 trace. The peaks representing these compounds are clearest in sample 37.

Figure 23 (A-C) is a composite chromatogram displaying the 16 PAH compounds listed on the USEPA priority pollutant list. All compounds were above the detection limit except the six ring PAHs, which were only visible in sample 01. This is most likely due to the bias against high molecular weight compounds due to using the instrumental conditions employed in this study. All three samples have a predominance of 178 and

202 Da molecular weight compounds, alluding to anthropogenic sources (Yunker et al. 2002). Closer investigation can provide additional information to discriminate between petrogenic and pyrogenic inputs. Sample 01 (Fig. 23 (A)) contains the most even distribution of compounds, still fluoranthene and pyrene showed the highest abundance. Sample 25 (Fig. 23(B)) displays a dominance of the same 4 ring parents and additionally naphthalene. Particularly fluoranthene is relatively more abundant than pyrene, signifying petrogenic input (Yunker et al. 2002). The pyrolyzate of sample 37 (Fig. 23 (C)) is particularly enriched in 3 and 4 ring PAHs, which dwarf the other compounds. In particular phenanthrene is by far the most abundant, again suggesting combustion input (Yunker et al. 2002).

PAH compounds are derived from both natural and anthropogenic sources. In the highly industrialized setting of the Passaic River it is inferred that only a minor fraction of total PAH quantities are of natural origin (e.g., from forest fires) (Yen et al. 2006). Anthropogenic sources include both 'pyrogenic' and 'petrogenic' sources. Pyrogenic sources are incomplete combustion of carbon sources such as biomass and various fossil fuels while petrogenic sources include petroleum related sediment contamination. In previous work it has been asserted that the primary source of PAH compounds found in the New York/New Jersey Harbor estuary system is pyrogenic in nature (Yen et al. 2004, Yen et al. 2006). Parent PAHs, especially those with higher molecular weights (i.e. four, five and six ring compounds) are usually more abundant in combustion related sources, while alkylated homologues and lower weight PAHs usually indicate a petroleum source. Based on this information PAH ratios have been proposed in the literature to distinguish between sources (Yunker et al. 2002, Yan et al. 2006). To assess their applicability to the

present study, these parameters were computed using the Py-GC/MS results and are discussed below.

The first plot evaluated (Fig. 24): Fluranthene (FLA) divided by pyrene (PYR) on the x-axis and phenanthrene (PHN) divided by anthracene (ANT) on the y-axis shows that the samples are clustered around the dividing line, except for some samples from Core 5A and 7A. Figure 25 provides a detail of the Figure 24, displaying the sample core number and depth for each data point(e.g., sample "7307" is from the 307 cm depth interval in Core 7A). In this plot three clusters can be observed, cluster (1) contains samples from Cores 7A, 9A, and 5A all corresponding to depths in which PAHs were observed in high quantities. Core 7A samples include those from 3.8 – 5 meter depths, Core 9A samples include those from just below 3 m and just above 6 m, and Core 5A samples include depths from 3 – 4 meters. In cluster (2) samples are represented from core 5A from the 2 – 3.5 m depth correlating with high PAH concentrations. The rest of the samples (3) are clustered very close about the line and seem to show influence from both sources. This basic ratio has been proven effective but additional ratios were employed to gather further information.

Figure 26 (A) displays fluranthene (FLA) divide by the sum of fluranthene (FLA) and pyrene (PYR) on the x-axis and phenanthrene (PHN) divided by anthracene(ANT) on the y-axis. In Figure 26 (B) there is benzo(a)anthracene (BAN) divided by the sum of benzo(a)anthracene (BAN) and chrysene (CHR) on the y-axis. Figures 27 and 28 respectively show the same plots at greater detail. These two ratios produced similar

results with the majority of samples displaying mixed input from both sources and the same two groups plotting in the combustion zone.

Since methylated PAHs are relatively abundant in petroleum, ratios employing them have been found to be useful in detecting petrogenic inputs (Yunker, Macdonald 2003). (Reference). Figure 29 displays the sum of PHN and ANT divided by the sum of PHN, ANT, and their respective methyl groups on the x-axis and (A): ANT divided by the sum of PHN and ANT on the y-axis; (B): FLA divided by the sum of FLA and PYR on the y-axis. Looking in closer detail (Figs. 30, 31), the former group (3) includes samples which show a combustion signature, while group (4) contains compounds which have a petroleum signature. In the latter; groups (1) and (2) represent the same samples explained throughout this section while group (4) contains a new group of samples emerging with particularly heavy petroleum input.

Figure 32 displays the sum of FLA and PYR divided by the sum of FLA, PYR, and methylpyrenes on the x-axis and FLA divided by the sum of FLA and PYR on the y-axis. This ratio again displays the same groups (1) and (2) with significant combustion input with the rest of the samples plotting as mixed source contribution, as seen in detail on Figure 33.

Overall the groups specified above correlate very well to the chromatogram fingerprints as well as the total concentration plots which will be discussed below. Samples which were not grouped in this section are thought to consist of mixed input, or the complex trends which exist were not apparent enough to be supported by ratio analysis alone.

3.3.2.3 Comparison of Py-GC/MS and Conventional PAH Analyses

Care must be taken in quantification exercises given that PAHs can be generated during the analytical pyrolysis of the sample. In particular phenanthrene and anthracene may be produced by the cleavage of covalent bonds in cellulosic material such as lignin (Kruge and Permanyer 2004). The PAH concentrations produced via pyrolysis may be evaluated if compared to solvent extraction analysis. The publicly-available data set produced by the Lower Passaic River Restoration Project (LPRRP) contains PAH analytical results generated in the conventionally accepted way, using EPA method 8270 on many of the same samples used in this work (LPRRP, 2008). Briefly, this EPA method requires solvent extraction, extract clean-up, and subsequent GC/MS analysis of sediment samples (USEPA, 1998), a time-consuming series of procedures employing hazardous organic solvents. These conventional data from the LPRRP were only available for two of the four cores evaluated in this work (9A and 7A) for which comparisons with the Py-GC/MS results are shown (Figs. 34 - 36). It is evident by visual inspection that the pyrolysis data are strongly correlated with the conventional EPA method 8270 data. Generally the conventional method produced apparently higher yields, most notably in the higher molecular weight PAHs. This is likely caused, at least in part, by the bias against high molecular weight compounds due to the instrumental conditions set on the Py-GC/MS instrument used in this study. Note that for the LPRRP data, most (but not all) results are for pairs of adjacent core slices combined prior to analysis. The Py-GC/MS results are from individual slices, usually only every other slice. This means that the two data sets should be compared in most instances on the basis of general trends only.

Figure 34 (A) illustrates the concentrations for the 4 ring PAH pyrene in core 7A. Overall the Py-GC/MS quantitations were slightly underestimated relative to the conventional. The two deepest slices were analyzed individually by Py-GCMS and show low PAH concentrations but a large spike in concentrations in the slice just above, at 4.95 and 4.84 m depth respectively, whereas for the conventional analysis, these two slices were composited, yielding an intermediate value. The higher sampling resolution employed in the Py-GC/MS work fortunately permitted the recognition of this geochemical transition. Figure 34 (B) follows the same trend for phenanthrene. Figure 34 (C) and (D) plot pyrene and phenanthrene respectively in Core 9A. The results from the two techniques are extremely well correlated, with slightly lower concentrations and higher resolution for the pyrolysis method. In Figure 35 (A, B, C, and D) the same trend holds true. Chrysene shows a similar underestimation in concentration as its 5 ring PAH benzo(a) pyrene displays a more significant underestimation in quantity. Figure 36 plots dibenzothiophene against depth for core 7A and core 9A. These concentrations are more comparable to phenanthrene most likely due to the similarity in molecular size of these two compounds. Dibenzothiophene concentrations in 9A were the only to result in concentrations higher than EPA method 8270, yet are still relatively low overall.

A small number of the conventional analyses were performed on individual samples in common with the Py-GC/MS sample set. Also for a small number of the conventional analyses done on paired, adjacent core slices, there are Py-GC/MS data available for both slices individually, permitting the latter to be averaged. Using this subset of the results, direct, one-for-one comparisons can be made (Fig. 37). It is evident that the results from the two techniques have a strong linear correlation ($r^2 = 0.86$),

however the data fall below the 1:1 ratio line. Instead they tightly cluster around the 1:2 ratio line, which approximates the slope produced by linear regression. This implies that the correction factors applied to the raw Py-GC/MS results cause the underestimation. Simply doubling them across the board would yield results quite in tune with the conventional method, which has presumably been repeatedly validated by USEPA laboratories. For this work the quantitations are referred to as estimated quantities or 'semi-quantitative' due to the slight underestimations observed, however confidence is high in the trends observed. The Py-GC/MS correction factors presented here should be reevaluated in future projects.

3.3.2.4 Principal Components Analysis

The principal components result from multivariate analysis taking *n* input variables and computing *n* new composite variables, ranked in order of significance (ref). Typically, the first several principal components that result (i.e., those ranked highest) will reflect a significantly large fraction of the variance present in the data set, thereby offering a small number of new, composite variables for the convenient visualization of data trends. Each principal component has its corresponding eigenvector, which shows the relative contribution, positive or negative, of each of the input variables. Principal components analysis (PCA) is particularly helpful in the exploration of datasets containing large numbers of variables and/or samples. In the present case, there are 138 variables generated from the Py-GC/MS analysis of 90 samples, thus it was anticipated that PCA would provide useful insights.

The full Py-GC/MS data set was employed in the first PCA attempt, for which the first principal component accounted for 26% of the variance (Fig. 38A). Examination of the

corresponding eigenvector showed a strong positive contribution from the pyrolysis products of natural occurring biomass versus a strong negative contribution from PAHs (Fig. 38B). The samples from the upper zones of the cores tend to have high positive values of the first principal component, while those from the lower tend to have strong negative values, indicating a depth-related trend (Fig. 38A) In an attempt to differentiate between pyrogenic (combustion) and pyrogenic (unburned petroleum product) inputs, a second PCA was undertaken, using a subset of the Py-GC/MS data containing only polycyclic aromatic compounds and petroleum biomarkers. The resulting second principal component (accounting for 15% of the variance), and to a lesser extent, the fourth principal component (8% of the variance) appeared to best show separation between the biomarkers and the PAHs, by examination of its eigenvector. The upper left area of the eigenvector cross-plot (Fig. 39 (B)) is populated mainly by parent PAHs, the central area by alkylated PAHs, and the lower right by petroleum biomarkers. Correspondingly, samples in and adjacent to the lower left quadrant of the principal components cross-plot (Fig. 39 (A)) are likely to be the recipients of a greater petrogenic input. These tend to be samples from the mid sections of the cores.

3.3.5 Chemostratigraphy

Visualizing the estimated concentrations of individual compounds as a function of sediment depth provides a chemostratigraphic perspective on the accumulation of sedimentary contaminants over time. All parent PAH compounds followed a similar depth trend; phenanthrene, pyrene, chrysene, and benzo[*a*]pyrene are representative (Figs. 43-46). Core 5A contains by far the highest concentrations of these compounds at a

depth range of 2-4 m. The 3 – 4 ring PAHs were seen in concentrations ranging from 80 – 120 mg/kg, while benzo[*a*]pyrene was observed near 25 mg/kg just above 3 m. The high concentrations are attributed to the core location near the mouth of the river, where it empties into Newark Bay. It has been observed that due to the tidal influence sediments are constantly resuspended and transported out to the bay. The most intense deposition occurs near to the mouth due to a reduction in velocity as the river opens into Newark Bay (Malcolm Pirnie, Inc. 2006, 2007). Additionally the lower 3.2 RK received relatively thick deposits of sediments in recent decades, as discussed in Section 1.5. Therefore a significant contaminant load carried with sediments appears to have been transported downstream and deposited near the mouth.

Core 7A exhibits a PAH spike between 4.5 and 5 m depth, which is particularly pronounced in sample 37 (discussed in Section 3.3.2.3). Sample 37 occurs at a change in lithology from the sand lens occurring in sample 38 to a silty matrix (sample 37) (Fig. 12). The concentrations in these spikes range from 40 mg/kg (phenanthrene) to about 8 mg/kg (benzo[*a*]pyrene) (Fig. 40 - 43). The higher porosity sandy lens could serve as subsurface pathway for hydrocarbon migration, which then accumulates in the immediately superjacent silty sediments. Based on the chromatographic fingerprint of sample 37 (Fig. 14 (C)), a coal tar source is likely, perhaps originating from the manufactured gas plant formerly sited on the adjacent river bank (Fig. 7). A secondary spike is also observed near 0.5 m depth particularly in the 4 and 5 ring PAHs.

Core 9A displays two spikes in phenanthrene and pyrene concentration occurring just below 3 m and at 6 m depth (Figs. 40, 41) with a range of 10 – 30 mg/kg. The two spikes in Core 9A also corresponds to a change in lithology, occurring above and below the

sandy lens. Although the spikes are not sharply delineated in the samples directly adjacent to the sandy lens, trends towards increasing concentration are evident moving both upwards and downwards away from the sand. One possible explanation is again a subsurface hydrocarbon migration occurring via the sandy lens. Core 5A also has an area of increased grain size at the bottom of the core in which the concentrations increase as the grain size decreases but this relationship is not as well defined. Core 10A is located furthest upstream. The concentrations range from 8 – 40 mg/kg and are highest near to the surface of the core (0 - 1 m). One possible explanation is more recent anthropogenic input. Possible sources include nearby CSO outfalls and the proximity to the Diamond Alkali site, the New Jersey Turnpike, and downtown Newark (Fig. 3).

Petroleum biomarker concentrations were also estimated, including the C_{29} and C_{30} hopanes, as well as the isoprenoids pristane and phytane (Figs. 44, 45). Core 5A displays high concentrations of the sum of the isoprenoids and hopanes in a window from 2 – 3 m depth. Core 7A contains a similar window of high concentrations from 2.5 – 3.5 m depth, with a second slight spike occurring for hopanes near 0.5 m depth. Core 9A contains a concentration spike in the 4 – 6 m section for all four petroleum biomarkers. Core 10A appears to be affected throughout the entirety of the core, with hopanes dominating near the surface (close to 120 mg/kg) and the isoprenoids oscillating in concentrations from 0 – 30 mg/kg from 1.5 m through to the bottom of the core. The pristane/*n*-C_{17} alkane ratio was employed to assess the extent of biodegradation occurring in the cores (Fig. 46). The ratio values in Cores 7A and 9A display a positive correlation to petroleum marker concentrations, while the other two cores do not . The ratio for 5A displayed two peak values occurring at 2.15 m and 4.3 m depth, where as the overall

concentration plot suggested a window of high concentration throughout the respective segment 2.35 -2.95 m depth for hopanes. Isoprenoids concentration oscillated throughout the core. Core 10A exhibited an area of high hopane concentration (surface to 1 m depth) and high concentrations of isoprenoids and a high pristane/*n*-C_{17} alkane below 1 m depth.

The depth-related trends in the first principal component (full Py-GC/MS data set) noted in Sec. 3.3.2.4 are evident when plotted as a function of depth (Figs. 47(A,B), 48 (A,B)). This sensitivity to biomass versus hydrocarbon contaminant input suggested a ratio of the sum of indole and guaiacol divided by the sum of phenanthrene and pyrene plus indole and vinyl guaiacol. The first principal component and this ratio produced to check the geochemical inference were positively correlated (Figs. 47, 48). In core 5A the first principal component is high in value (around 5) near the surface (0 – 1 m), transitions to mid values(near 0) in the middle zone (1-2.95 m), and low in the lower zone (3.15 – 4.3 m). Core 7A ,9A, and 10A follow a similar zoning pattern with the uppermost zone highest in biological input, followed by a mid transition zone, and finally more fossil fuel input near the bottom of each. Some of the finer points include the following: in core 7A a markedly low values occur below 4.6 meters, in Core 9A there is also a marked drop in value below 5.6 m and a less dramatic drop in value at 3.3 m. Core 10A has a distinctive signature in the first zone (surface – 1 m). There is an oscillating pattern between high values (approximately 5) and mid values (approximately -1). These first principal component values positively correlate with the values in the derived ratio in all cores.

The three zones reported in core 5A suggest high natural biomass in the upper part of the core, followed by a transition mid core which could be a result of mixed input

or a dilution of anthropogenic inputs (Figs. 10, 11 (A-D)). This zone corresponds to the highlighted ^{137}Cs zone (Section 3.1); therefore it may be disturbed by remixing therefore diluting the area. The lower zone appears to be most affected by anthropogenic input, except for the deepest sample. One possible explanation for the oddity of this sample could be that the core penetrated through to preindustrial sediment. Although this is unlikely given that the core is < 5 m deep, the high volume of dredging occurring at this location could be an explanation. All trends in additional cores support the same fundamental explanations. The markedly low values in core 5A (except the single odd sample) and 7A in the deepest part of the core are occurring near to the sand lens suggesting again a secondary migration pattern. Core 9A also has low values occurring above the sandy lens and below it. The lowest values in core 10A also correlate with the coarsening in grain size. The oscillations occurring in many variables in this core are further evidence for influence of erosional and depositional events, or possibly influence from periodic flooding event. One possible explanation is that this core is especially near to a CSO outfall.

The apparent pyrogenic-petrogenic selectivity of the second principal component (PCA using only the polycyclic aromatic compounds and petroleum biomarkers; Fig. 39) makes it also interesting to view as a function of depth (Figs. 47, 48 (E, F)). The simple ratio suggested by this component was trimethyl phenanthrene divided by the sum of trimethyl phenanthrene and phenanthrene, with higher values indicating relatively greater contamination by petroleum products compared to combustion inputs. In all cores the second principal component was positively correlated to this ratio (Figs. 47, 48 (E-H)). Cores 7A and 9A follow the same general trend displayed in the first principal

component and its respective ratio. Cores 5A and 10A follow a similar pattern to the first principal component in with the highest values occurring in the upper section followed by a gradual change to lower values in the deepest section. However an oscillating trend emerges throughout the entirety of core 5A and the oscillating trend becomes more pronounced in the upper zone of Core 10A.

The corresponding trends in Cores 7A and 9A to those in the second principal component suggest that the areas most impacted by anthropogenic sources are those of a pyrogenic nature, additionally high values in the mid section of core 7A(particularly 3.15, sample 25) and 9A (5.2 – 5.9 m) suggest an area where petrogenic inputs are also occurring but are not as dramatic as the pyrogenic influences . The trends in cores 5A and 10A support the hypothesis that the most anthropogenically impacted sections of both cores are affected by a mixed input from pyrogenic and petrogenic sources (upper section in core 10A and lower-mid and lower section of 5A (excluding the lowest sample in 5A). Absolute amounts of petroleum biomarkers (hopanes) tend to decrease along with the values of the first principal component (full data set) and second principal component (hydrocarbon subset), while the absolute amounts of parent PAHs (e.g., pyrene) increases (Figs. 49, 50).

One possible explanation is that Cores 7A and 9A have petroleum contaminated zones which are also biodegraded. In core 5A significant evidence for petroleum is present in a distinct zone mid core and biodegradation of both petroleum sources and higher plant material is occurring throughout. Core 10A is high in hopane concentration above 1 meter depth, and the opposite is true for isoprenoid concentration and the pristane/*n*-C_{17} alkane ratio. This would suggest that there is a zone which is affected by

petroleum (surface to 1 meter depth) and the lower zone is exhibiting biodegradation of biomass. Overall two trends emerged. Cores 5A and 10A appear to have segments of the cores affected by all anthropogenic parameters, with relatively unaffected segments. Cores 7A and 9A appear to have segments affected by petroleum inputs and separate segments affected by combustion related sources interrelated to grain size. The high hydrocarbon concentrations (Figs. 40-45) occur either at the very bottom of the core (5A and 10A) in which the sandy lens is not penetrated, or directly above or below the sandy lens. This causes a potential concern that there may be a ground water source of hydrocarbons. The most likely source would be coal tar contamination, probably a byproduct of the former manufactured gas plant adjacent to core 7A (Fig. 7) which

The vinylguaiacol/indole (VGI or "veggie") ratio is a novel approach for discriminating between the inputs of biomass from aquatic or terrestrial sources (Micić et al., in press). The VGI for all cores averages around 0.3 - 0.5, an intermediate value to be expected in an estuarine system (Fig. 51). Core 5A, which is located near the mouth of the river, contains the highest aquatic biomass concentrations. Only in the very last sample (correlating with the sand lens) is there significant terrestrial input. As the locations move upstream terrestrial input becomes more apparent with 10A values closest to 0.5. The TOC vs depth plots (Fig. 13) display an oscillatory pattern in all four cores, which is reflected in the VGI ratio.

The higher TOC concentrations in cores 9A and 10A are therefore likely due to a more abundant terrestrial biomass input (Fig. 13). This may be correlated to erosional and depositional events which include periodic flooding resulting from various storm events.

4. Conclusions & Recommendations

The theme which is most pronounced throughout the entirety of the data analyzed in this work is of the separate zones occurring in each of the four cores. The diluted ^{137}Cs maximum zone occurring in the mid section of all cores happens to coincide with a catastrophic release of chlorinated compounds from the explosion at the Diamond Alkali Chemical site followed by a category 2 hurricane, which both occurred in 1960. The 1960s were also the period of peak nuclear testing in the United States which would result in the highest concentration of atmospheric fallout (i.e. ^{137}Cs). This zone is correlated to spikes in both PCB and TCDD concentrations (Fig. 10) in Core 7A and 9A. Unfortunately data for these chlorinate compounds is not available for cores 5A and 10A. Regardless there is enough evidence to support that the release of contamination followed by the storm surge caused thick beds of contaminated sediment to build up in the study area which also coincide with the reworking of the radionuclide fallout.

Core 5A, which is located the furthest downstream, appears to be the most impacted by anthropogenic influences. This is most likely due to its proximity to the mouth of the river. Large volumes of sediment are known to settle out of the water column as it empties into Newark Bay. Additionally during the tidal influence this sediment is often resuspended and pushed back upstream. Despite the reworking, separate zones can still be observed with the mid and lower sections most affected by contamination, including a mixture of pyrogenic and petrogenic sources. One possible interpretation is that the sources were released simultaneously or perhaps major releases are not observed as the spikes which occur in Cores 7A and 9A (Figs. 44 - 47) due to the tidal nature of the river providing a better environment for remixing. Cores 7A and 9A

have very distinct zones characterized by spikes in combustion related compounds occurring adjacent to the sand lens. The sediment deposited in these locations is also affected by resuspension since they are geographically inside the tidal influence zone; however the most notable pyrogenic concentration spikes occur adjacent to the observed sand lens. This evidence supports subsurface migration occurring chemically consistent with coal tar residue as a potential source, given that a manufactured gas plant was formerly in operation adjacent to core 7A. Both cores also have zones reflecting high petrogenic input, the most probable source being general outwash, given that the industrial land use on the banks of the study area is dominated by petroleum storage and transport operations. These zones generally coincide with the elevated ^{137}Cs section, which further shows evidence of high dilution/remixing. This could be interpreted as petrogenic inputs being deposited as part of normal sedimentation patterns and additional pyrogenic contamination occurring downcore via the sand lens.

Core 10A is the shortest of all four cores. Although the deepest section of this core does begin to coarsen, the sand lens is not penetrated. This core does not display the spikes in pyrogenic input readily visible in cores 7A and 9A, but the pyrogenic signature does increase downcore, suggesting that if a send lens is located below the segment of core, received combustion contamination may be migrating upward. Core 10A has the most highly contaminated upper section of all the cores. This may be a result of significant impact from a nearby CSO outfall which is constantly introducing fresh contaminants. This conclusion is additional supported by the pronounced oscillating pattern which suggests periodic flood events are directly influencing the contamination pattern.

The TOC% and VGI ratios are correlated with an increase in terrestrial input being a possible source of increased amonts of organic carbon in the upstream cores. This conclusion is supported by the grain size analysis results. It would be expected that the percent TOC would be increased in areas of lowest grain size. The organic carbon tends to adsorb to the smaller particles due to the larger surface area. The oscillation in VGI further supports the importance of flood events affecting the primary sedimentation pattern.

Overall it is concluded that the primary mechanism for sedimentation and therefore inadvertent contaminant deposition is settling of material which has been mixed and resuspended. A subsurface migration path occurring via the sand lens could be an explanation for the pronounced peaks in coal tar-derived material at the base of Cores 7A and 9A. A similar peak is not observed in core 5A or 10A presumable because the cores were not recovered deep enough to observe the full extent of sand lens or are too distance from the suspected coal tar source. However, both cores do show an increase in pyrogenic input down core where the samples begin to coarsen. The ^{137}Cs radiometric analysis resulted in the defining of three zones. The middle of which is significantly affected by some mechanism of dilution and remixing and the surface zone is also affected but to a lower extent. The deep zone is the only section of all cores which appears to be only marginally affected by remixing. This again supports the conclusion that the primary mechanism for sedimentation in this study area is affected by remixing. Upon analysis of the oscillating nature of the VGI ratio throughout all cores an influence of flood events also becomes apparent effecting both the transport of sediment from upstream sources as well as CSO outfall input.

References:

Blackledge RD. 2007. *Forensic Analysis on the Cutting Edge: New Methods for Trace Evidence Analysis*, Wiley-Interscience.

Dinkins CE, Tice KM. 1998. New solutions for old problems in Newark Bay. Seton Hall Law Review 29/1: 60-75.

Eby GN. 2004. *Principles of Environmental Geochemistry*. Thompson Brooks/Cole, 514 p.

Iannuzzi TJ, Huntley SL, Schmidt CW, Finley BL, McNutt RP, Burton SJ. 1997. Combined sewer overflows (CSOs) as sources of sediment contamination in the Lower Passaic River, New Jersey. I. Priority pollutants and inorganic chemicals. Chemosphere 34, 2: 213-231.

Killops S, Killops V. 2005. Introduction to organic geochemistry second ed. Malden (MA): Blackwell Science Ltd.

Kruge MA, Permanyer A. 2004. Application of pyrolysis-GC/MS for rapid assessment of organic contamination in sediments from Barcelona harbor. Organic Geochemistry 35: 1395 – 1408.

Lower Passaic River Restoration Project (LPRRP), 2008. PremisDownloadFinal_NonHistorical.mdb. Microsoft Access database file from http://www.ourpassaic.org/projectsites/premis_public/index.cfm?fuseaction=contaminants. Lower Passaic River Restoration Project.

Malcolm Pirnie, Inc. 2006. Lower Passaic River Restoration Project, Draft Geochemical Evaluation, Step 2. Version 2006/03/06

Malcolm Pirnie, Inc. 2007. Lower Passaic River Restoration Project Conceptual Site Model. Version 2007/02/28

Marshall S. 2004. The Meadowlands before the Commission: Three Centuries of Human Use and Alteration of the Newark and Hackensack Meadows. Urban Habitats, ISSN 1541-7115

Micić V, Kruge MA, Körner P, Bujalski NM, Hofmann T. Organic geochemistry of Danube River sediments from Pančevo (Serbia) to the Iron Gate dam (Serbia-Romania). *Organic Geochemistry* (in press).

New Jersey Department of Environmental Protection. 1999. The geology of New Jersey. Trenton (NJ): Division of Science, Research, and Technology Geological Survey.

New Jersey Department of Environmental Protection. 2009. Fish smart, eat smart: a guide to health advisories for eating fish and crabs caught in New Jersey waters. 2009 update. Trenton (NJ)

Olsen KK. 2008. A great conveniency; a maritime history of the Passaic River, Hackensack River, and Newark Bay. Franklin (TN). American History Imprints.

Olsen PE. 1986. A 40-Million-Year lake record of early Mesozoic orbital climatic forcing. Science 234: 789-912.

Passchier S. 2005. Particle size analysis (granulometry) of sediment samples. *Review of standards and protocols for seabed habitat mapping. NO-NITG, The Netherlands*

Paterson Friends of the Great Falls, Inc. 2010. History of Patterson, City of Industry (26 April 2010; www.patersongreatfalls.org/cityofindustry.html)

Peulvé S., de Leeuw J.W., Sicre M.-A., Bass M., Saliot A., 1996. Characterization of macromolecular organic matter in sediment traps from the northwestern Mediterranean sea. Geochimica et Cosmochimica Acta, 60: 1239-1259.

Saiz-Jimenez C., de Leeuw, J.W., (1986) Ligin pyrolysis products: Their structures and significance as biomarkers. Organic Geochemistry, 10(4-6), 869-876.

Shear NM, Schmidt CW, Huntley SL, Crawford DW, Finley BL. 1996. Evaluation of the factors relating combined sewer overflows with sediment contamination of the Lower Passaic River. Marine Pollution Bulletin 32, 3: 288-304.

Tankard A, Balkwill H. 2003. Extensional tectonics and stratigraphy of the North Atlantic margins. American Association of Petroleum Geologists Memoir 46: 155-174.

United States Army Corps of Engineers. 2008. Lower Passaic River Commercial Navigation Analysis. New York: New York District, Operations Division.

United States Environmental Protection Agency (USEPA). 1994. Diamond Alkali Superfund site Passaic River study area megasite management plan. Report no. 82658002

United States Environmental Protection Agency (USEPA). 1995. Feasibility Study for the Passaic River Study Area. Report no. EPA/23508-22089/R10.2.

United States Environmental Protection Agency (USEPA), 1998. Method 8270D - Semivolatile Organic Compounds by Gas Chromatography/Mass Spectrometry (GC/MS). Revision 4.

United States Environmental Protection Agency (USEPA). 2008. NPL Listing History. Report - EPA ID#: NJD980528996

United States Geological Survey. 2003. Quaternary lakes and river systems. (26 April 26 2010; http://3dparks.wr.usgs.gov/nyc/morraines/rivers.htm)

Varmuza K., Filzmoser P., 2009. *Introduction to Multivariate Statistical Analysis in Chemometrics*, CRC Press.

Yan B, Abrajano TA, Bopp RF, Benedict LA, Chaky DA, Perry E, Song J, Keane DP. 2006. Combined application of 13C and molecular ratios in sediment cores for PAH source appointment in the New York/New Jersey harbor complex. *Organic Geochemistry* 37: 674-687.

Yan B, Benedict LA, Chaky DA, Bopp RF, Abrajano TA. 2004. Levels and patterns of PAH distribution in sediments of the New York/New Jersey Harbor complex. *Northeastern Geology & Environmental Sciences* 26, 1&2: 113-122.

Yunker MB, MacDonald RW, Vingarzan R, Mitchell RM, Goyette D, Sylvestre S. 2002. PAHs in the Fraser River basin: a critical appraisal of PAH ratios as indicators of PAH source and comparison. Organic Geochemistry 33: 489-515.

Yunker M.B., Macdonald R.W., 2003. Alkane and PAH depositional history, sources and fluxes in sediments from the Fraser River Basin and Straight of Georgia, Canada. *Organic Geochemistry* 34:1429-1454.

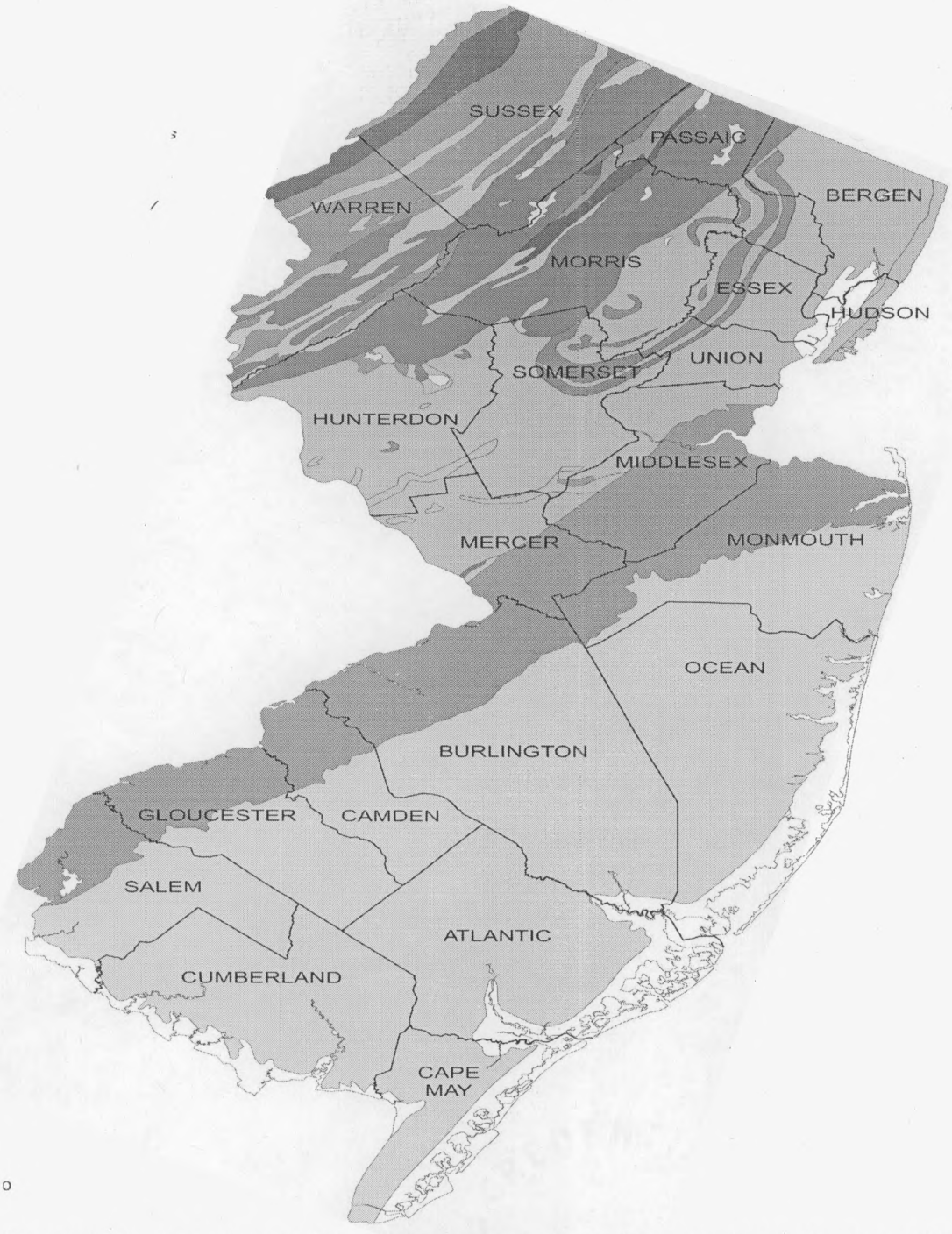

Figure 1. Geological map of New Jersey containing rock type and age. Courtesy of New Jersey Department of Environmental Protection (NJDEP), 1999. The yellow box highlights the general area of the Passaic River drainage basin (Fig. 2). Specifically the blue area refers to the Passaic Formation which underlies the lower Passaic River. The green and red areas refer to the basaltic formations which dictate flow of the headwaters of the river.

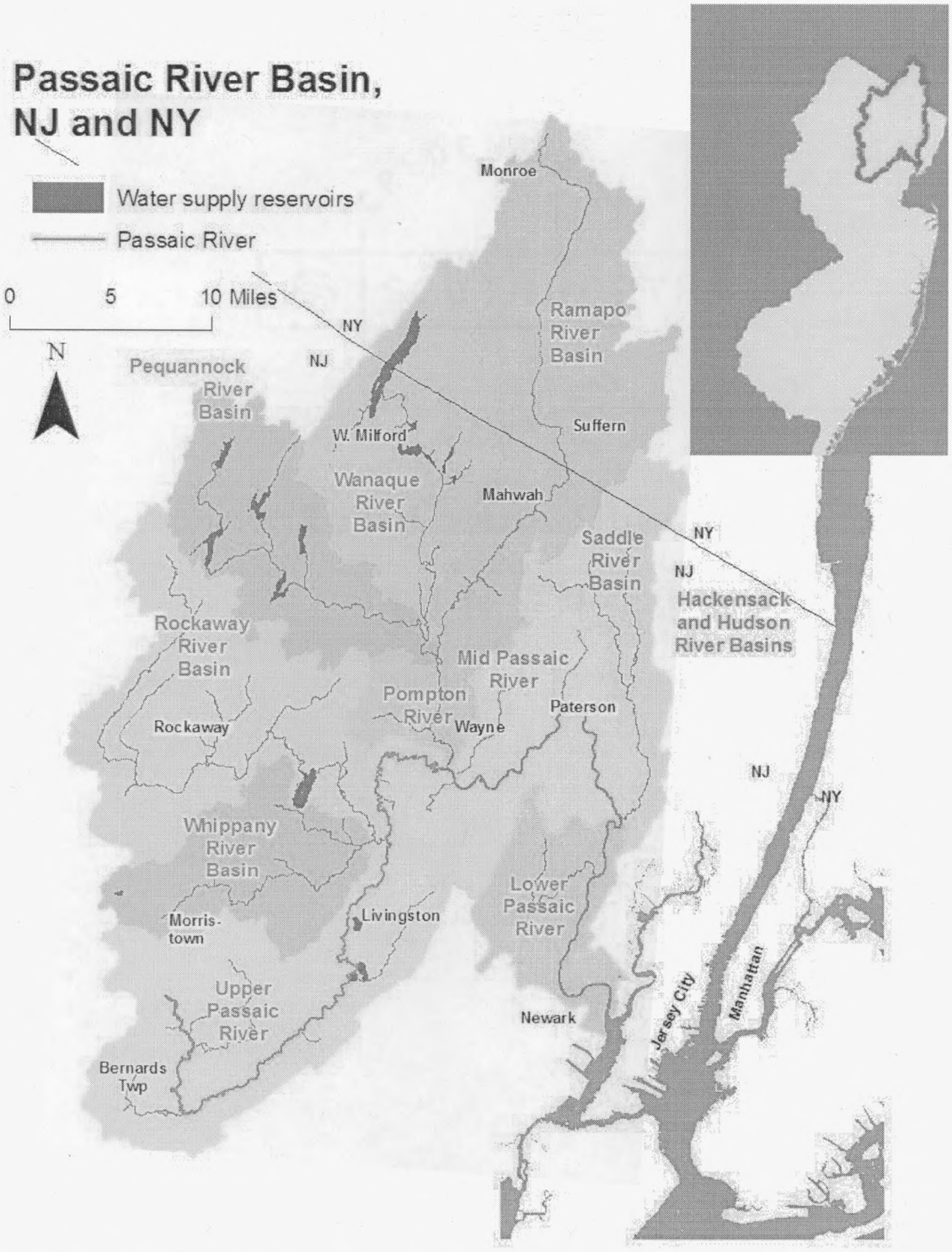

Figure 2. GIS (Geographic Information Systems) image of the Passaic River drainage basin, including tributary names and the New Jersey (NJ)/ New York (NY) harbor estuary system, courtesy of the Passaic River Institute. The upper corner displays the basin area relative to the whole of NJ. Figure courtesy of Passaic River Institute.

Figure 3. GIS image of the Passaic River CSO outfall locations. Figure courtesy of the Passaic River Institute. It should be noted that the outfalls are numerous with 37 occurring below the second river confluence.

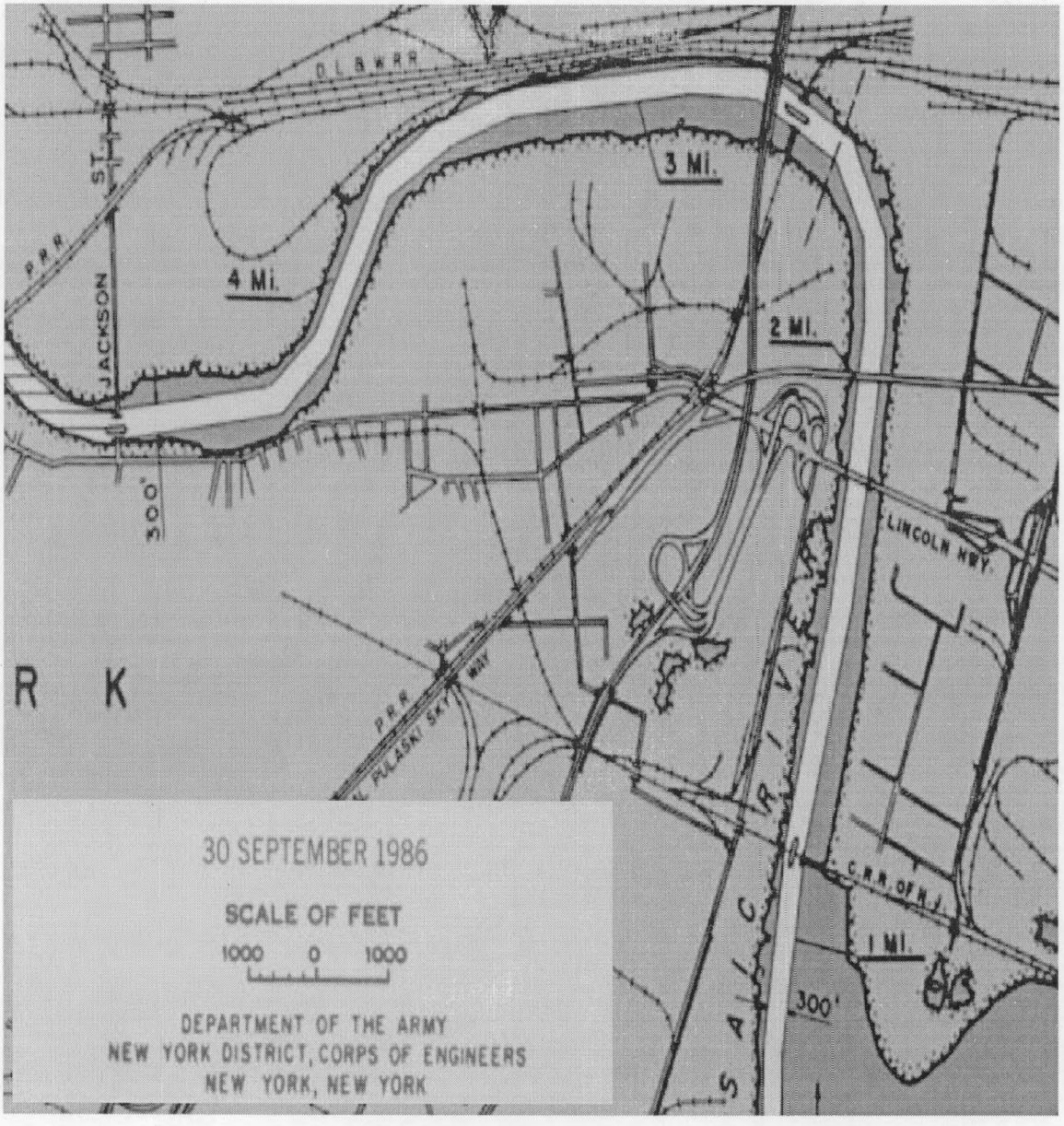

Figure 4. Image of the Passaic River federal navigation channel (New York Districtt, Corp of Engineers, New York, NY 1986). The area which is dredged to navigable depth is highlighted in white. It can be observed that dredging does not take place from bank to bank and the deepened area of the channel is not always directly in the center of the river.

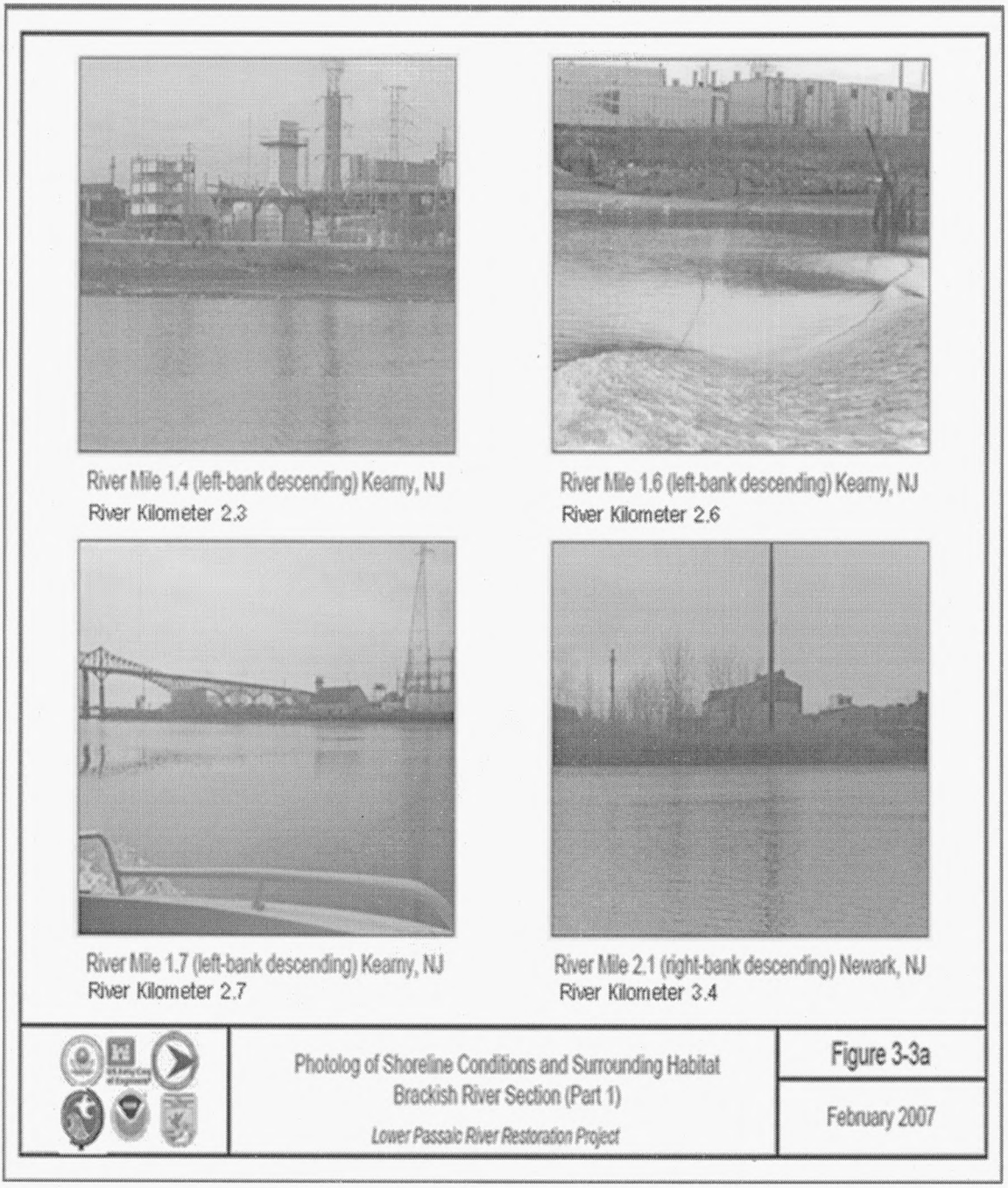

Figure 5. Images of the Passaic River lower 3 River Kilometers (RK) represented from Malcolm Pirnie, Inc. 2007. This image displays the predominant industrial land use along the banks of the lower Passaic.

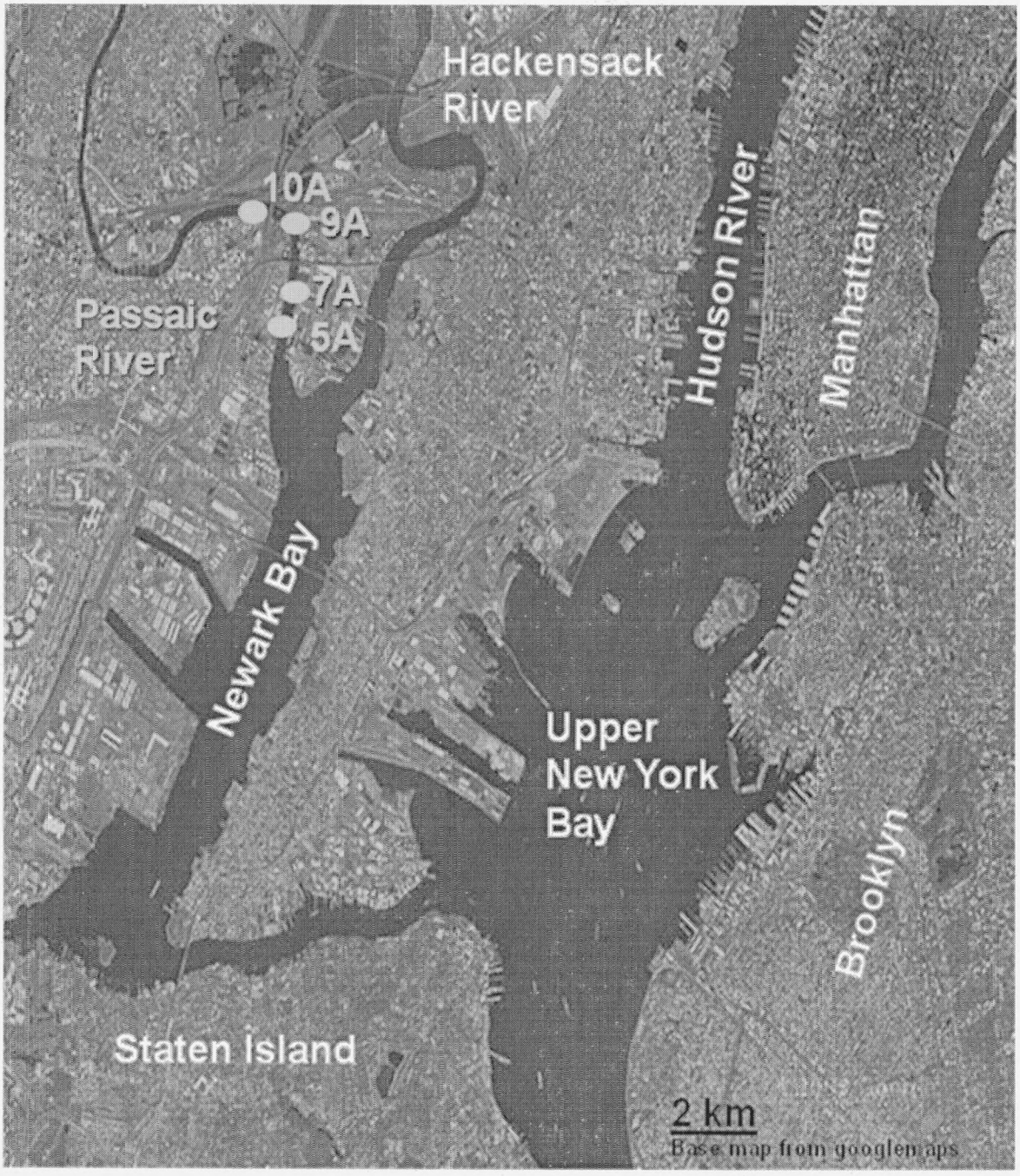

Figure 6. Satellite image of the NY/NJ harbor estuary system with core locations. Core 5A is located at RK 1.8, Core 7A is located at RK 2.3, Core 9A is located at RK 3.5, and RK for Core 10A 2.6 RK.

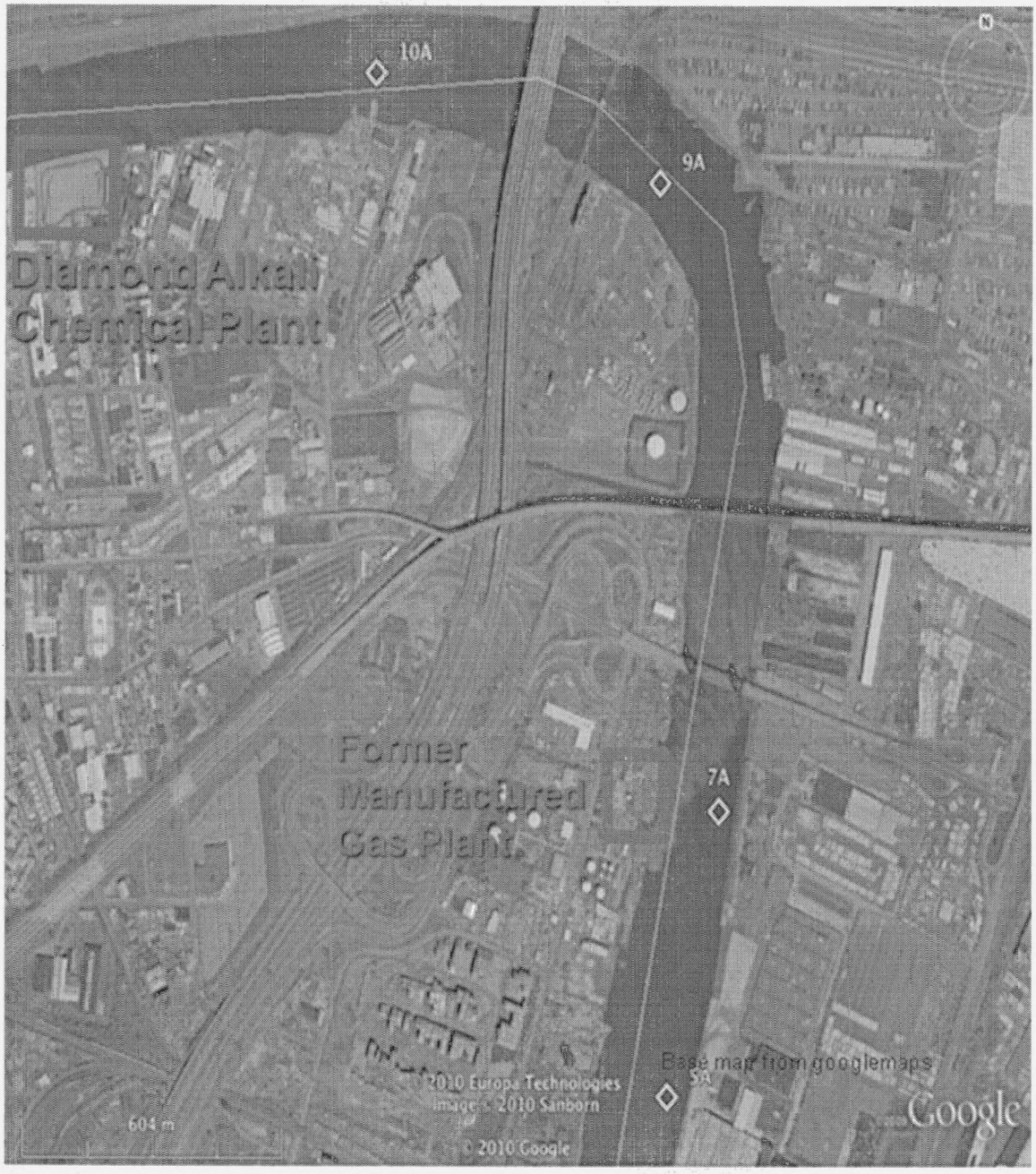

Figure 7. Satellite map of the Passaic River providing core locations in respect to the former manufactured gas plant and Diamond Alkali chemical plant. It can be observed that the cores are not located within the federal navigation channel when compared to Figure 3.

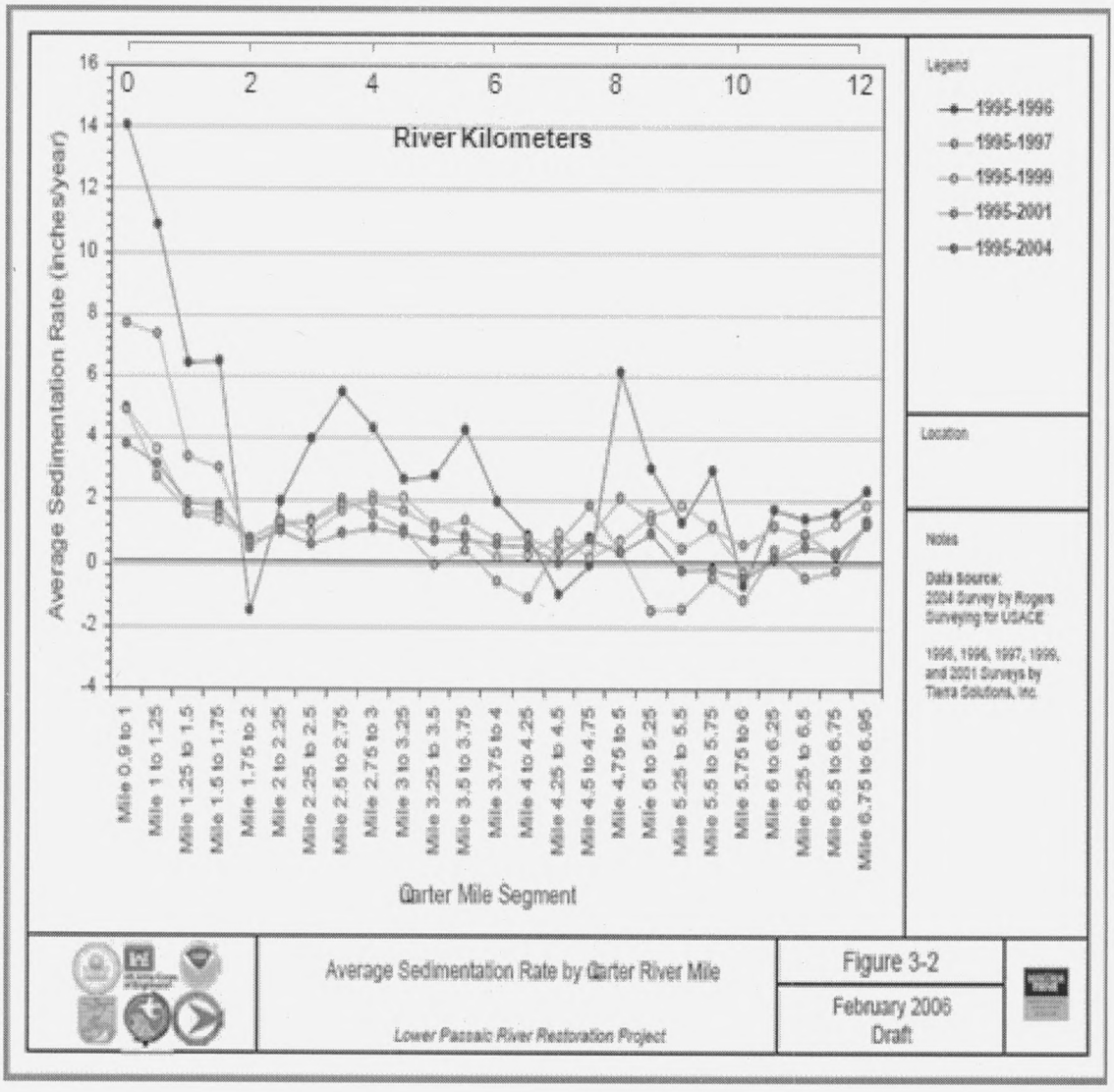

Figure 8. The average sedimentation rates plotted against river mile (RM). This data was estimated by Malcolm Pirnie, Inc. through comparing bathymetric data from 1995, 1996, 1997, 1999, 2001, and 2004 as well as 137Cs analysis completed for marker years (Malcolm Pirnie, Inc. 2006). The sedimentation rate plotted in red was calculated from bathymetric surveys completed in 1995 and 1996 which was taken as the change in depth over that year. Yellow represents an average change in depth per year from 1995 through 1997; green represents the average rate for years 1995 –2001; and blue represents averages from 1995 –2004. This data suggests a general decrease in sedimentation rates from 1995 through 2004.

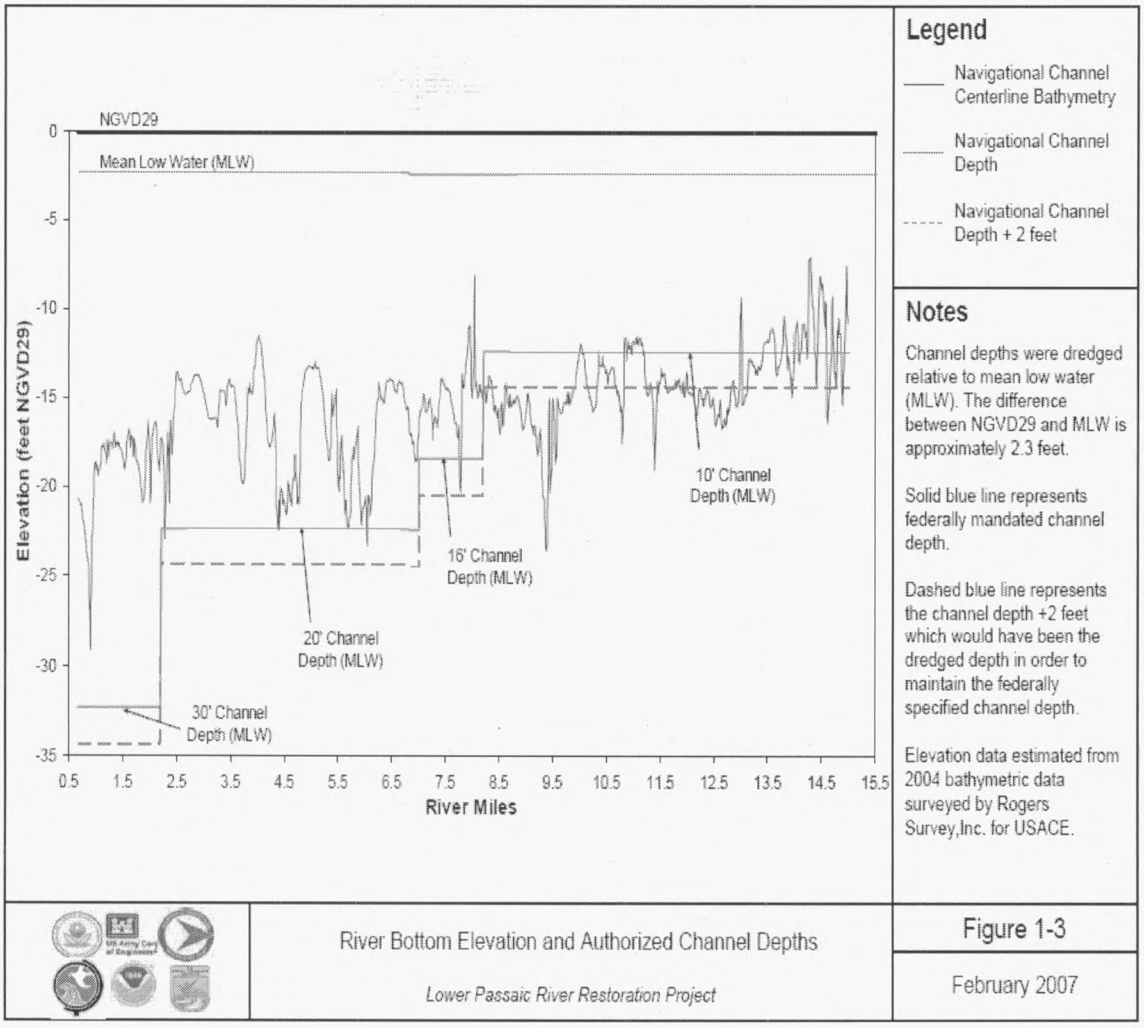

Figure 9. The river depth at the time of the bathymetric survey in 2004 is recorded in red for corresponding river miles (RM). The previous depth to which the channel was dredged to maintain navigation is represented in blue (Malcolm Pirnie, Inc. 2007). This also serves as an example of how the average sedimentation rates were calculated in Figure 4. Note that the greatest change (depth from the previously dredged depth to 2004 depth) occurs below 3 kilometers. This area was last dredged in 1983, while the area upstream of 3 kilometers was last maintained in 1946 or earlier.

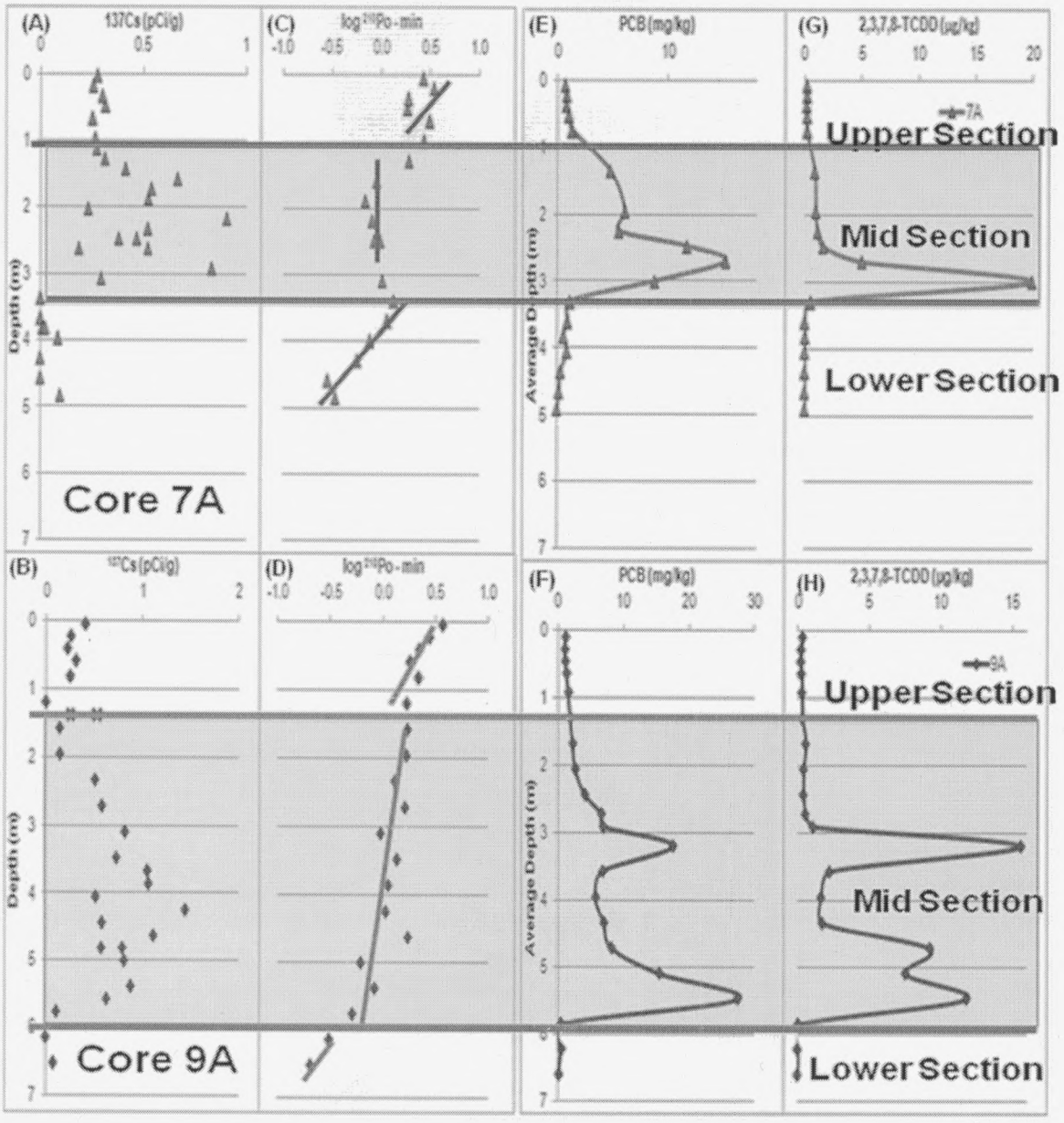

Figure 10. The data for all eight plots were retrieved from the Lower River Restoration Project database accessible online at : http://ourpassaic.org/ (A) & (B) represent ^{137}Cs picocuries/gram (pCi/g) vs. average depth, with Core 7A(A) and Core 9A (B). (C) & (D) represent log10 excess ^{210}Po vs. average depth for Core 7A(C) and Core 9A(D). (E) & (F) represent PCB concentrations (mg/kg) vs. average depth, with Core 7A(E) and Core 9A (F). (G) & (H) represent TCDD dioxin concentration (µg/kg) vs. average depth for Core 7A(G) and Core 9A(H). It should be noted that three distinct sections are hypothesized. The upper and mid sections seem to be affected by reworking of the sediment, particularly in the mid section. The lower section appears to be relatively undisturbed.

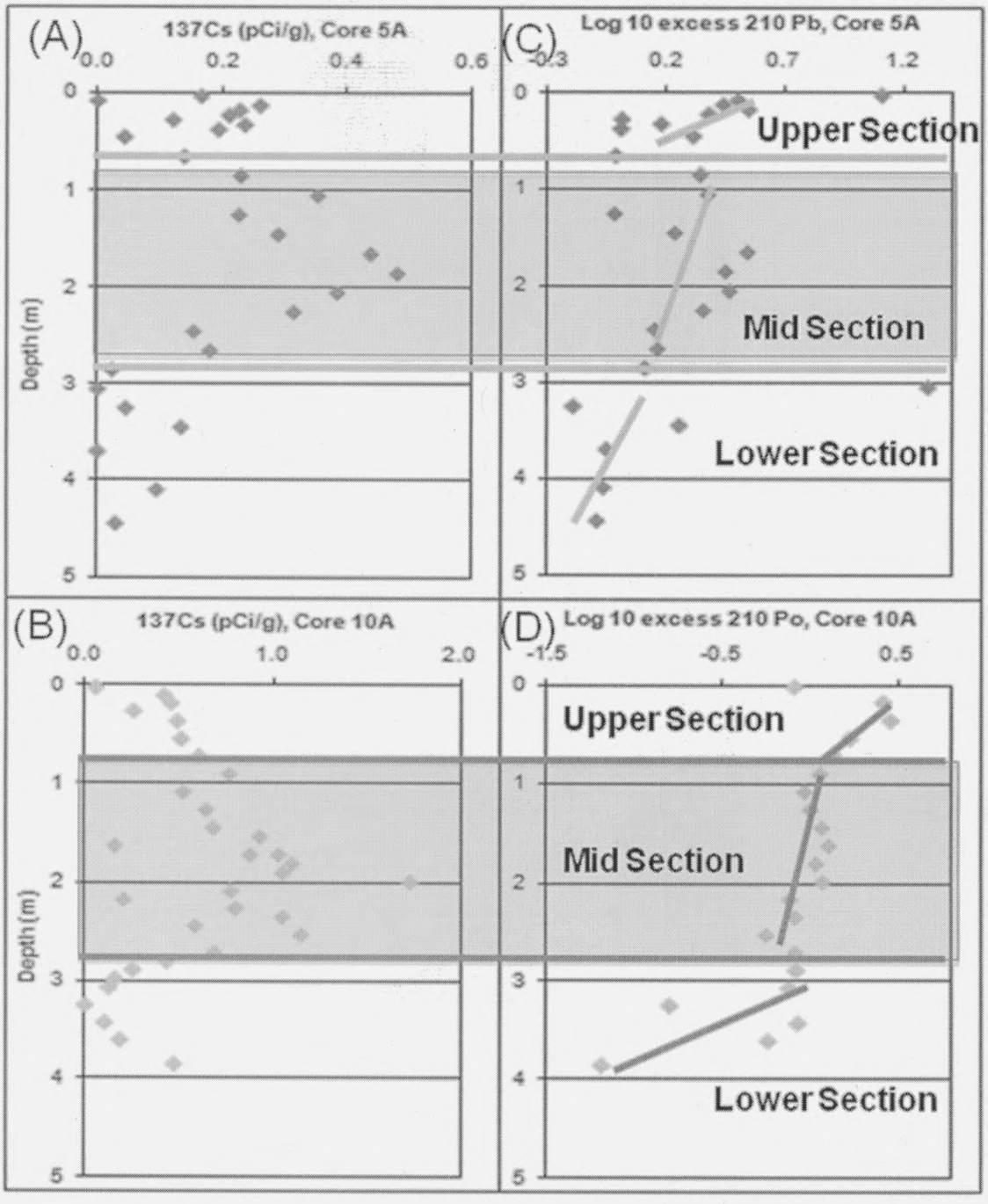

Figure 11. The data for all eight plots were retrieved from the Lower River Restoration Project database accessible online at : http://ourpassaic.org/ (A) & (B) represent ^{137}Cs picocuries/gram (pCi/g) vs. average depth, with Core 5A(A) and Core 10A (B). (C) Represent log10 excess ^{210}Pb vs. average depth for Core 5A(C) and ^{210}Po vs. average depth for Core 10A (D). It should be noted that three distinct sections are hypothesized. The upper and mid sections seem to be affected by reworking of the sediment, particularly in the mid section. The lower section appears to be relatively undisturbed.

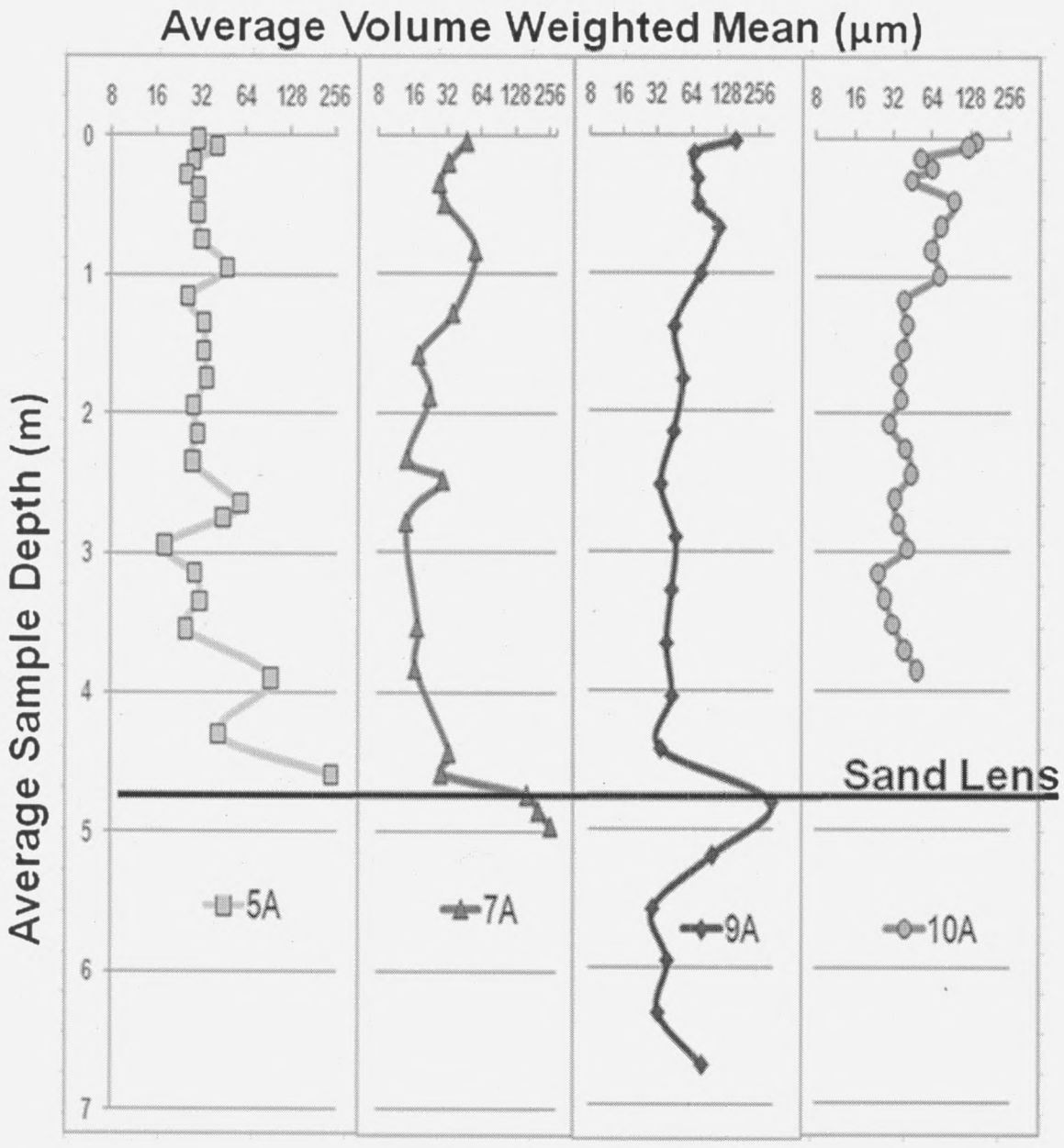

Figure 12. Average volume weighted mean (µm) vs. average depth (m) plot. Data collected from Particle Mastersizer 2000 using standard operating procedure for sediments. The general trend to be noted is a coarsening in grain size as the locations move upstream. Additionally there is a sand lens occurring in core 5A, 7A, and 9A while core 10A begins to coarsen at the bottom.

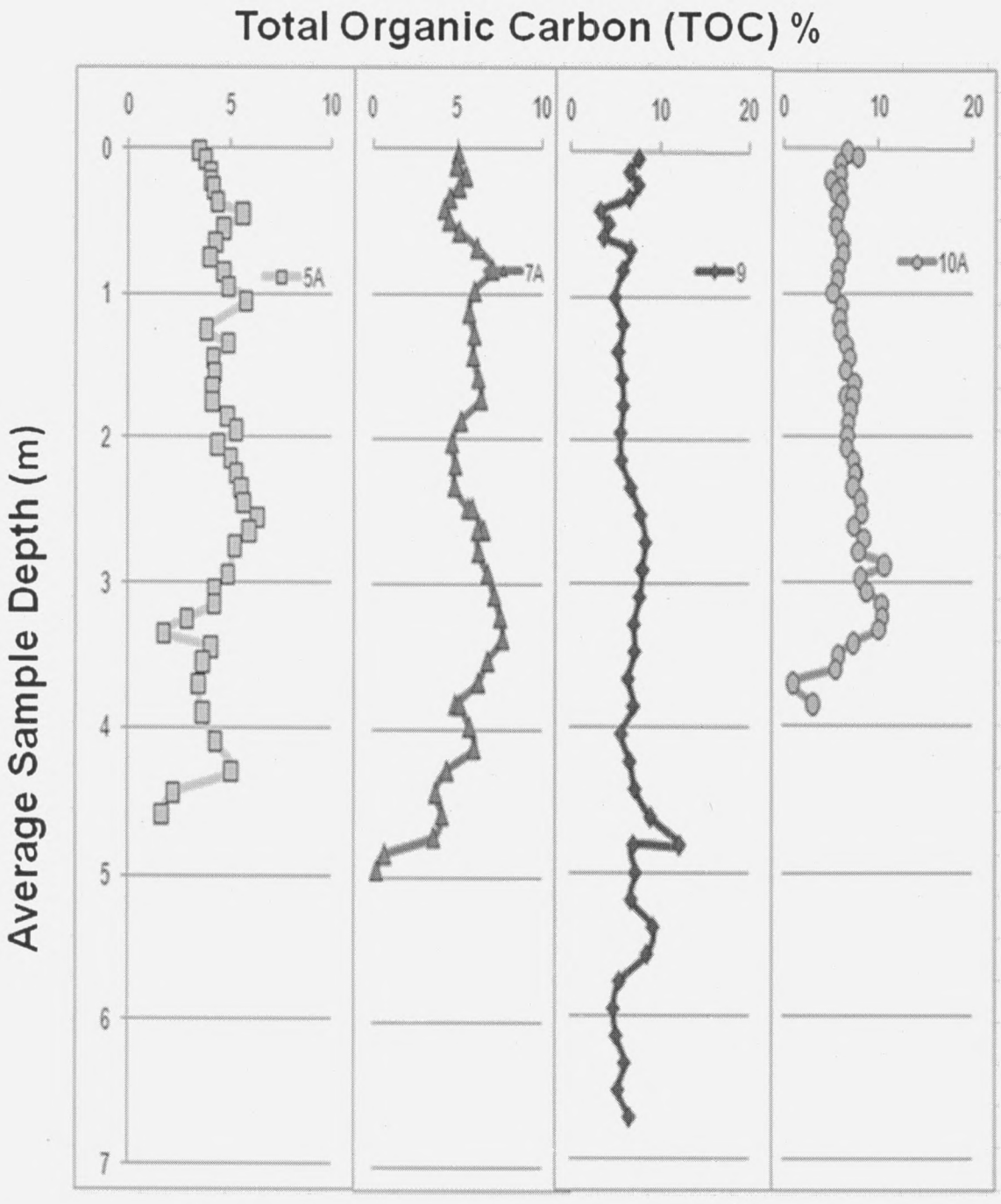

Figure 13. Depth plot of the total organic carbon (%) vs. average sample depth (m). The general trend to be noted is that TOC is relatively high in all samples and increases as the core locations move upstream.

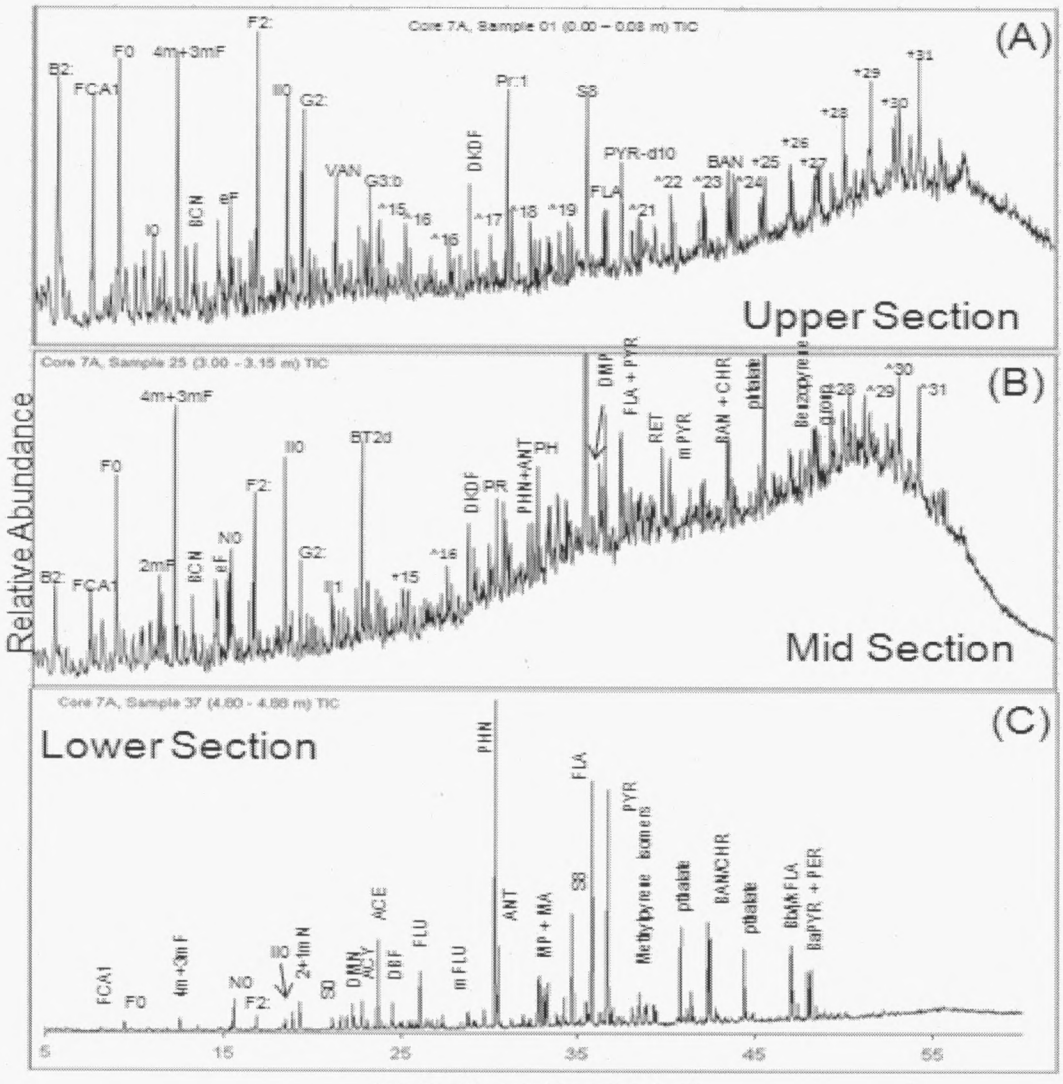

Figure 14. Py-GC/MS total ion current chromatograms from Core 7A (RK 1.8). Data collected in full scan mode: (A) surface sample 01, 0.00 – 0.08 m depth segment; (B) sample 25, 3.00 – 3.15 m depth segment ; (C) sample 37, 4.80 – 4.88 m depth segment. See Table 7 for code translations.

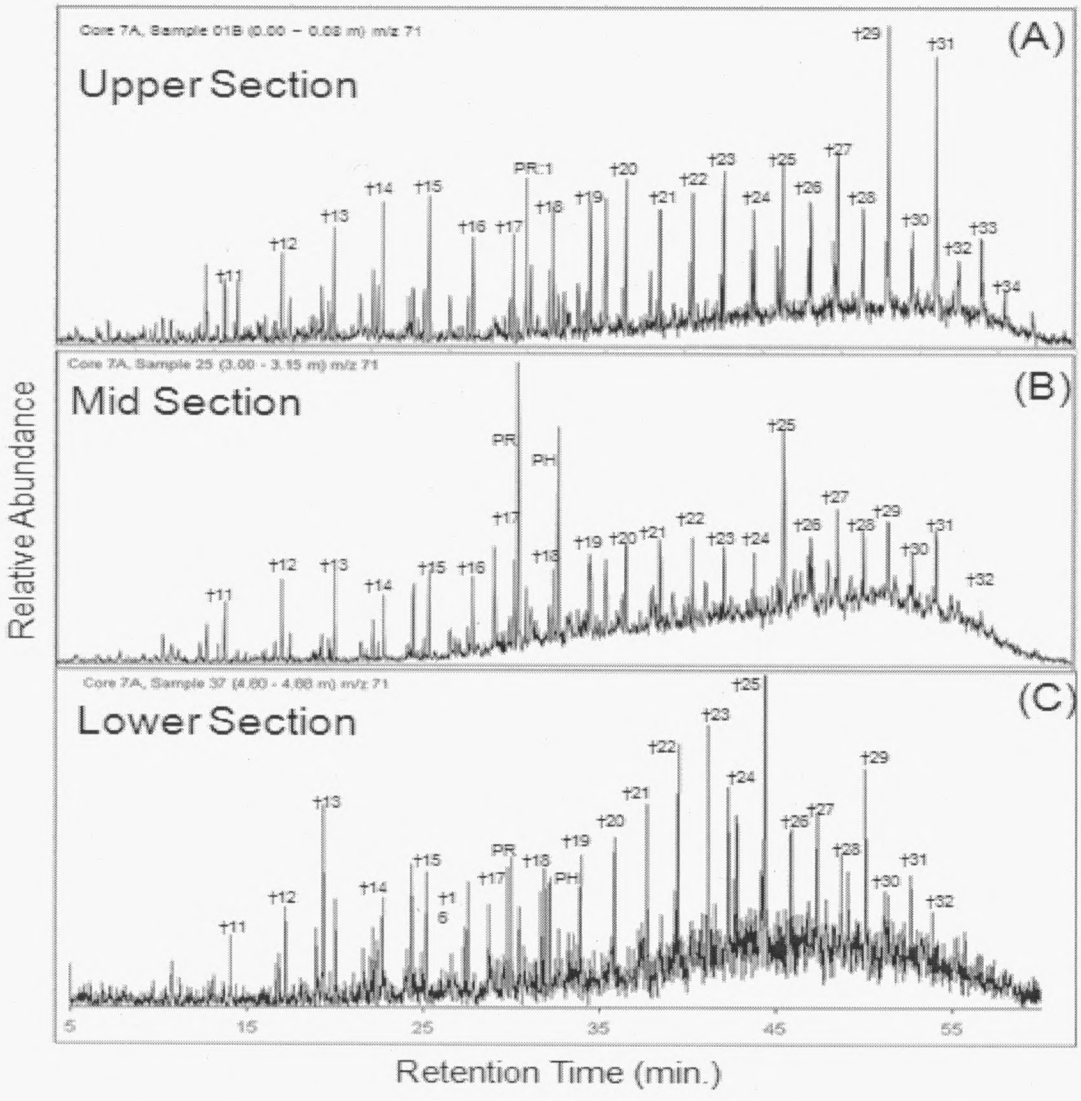

Figure 15. Py-GC/MS *m/z* 71 mass chromatograms from Core 7A (RK 1.8). Data collected in full scan mode: (A) surface sample 01, 0.00 – 0.08 m depth segment; (B) sample 25, 3.00 – 3.15 m depth segment ; (C) sample 37, 4.80 – 4.88 m depth segment. See Table 7 for code translations, *n*-alkanes (†) and *n*-alk-1-enes (^).

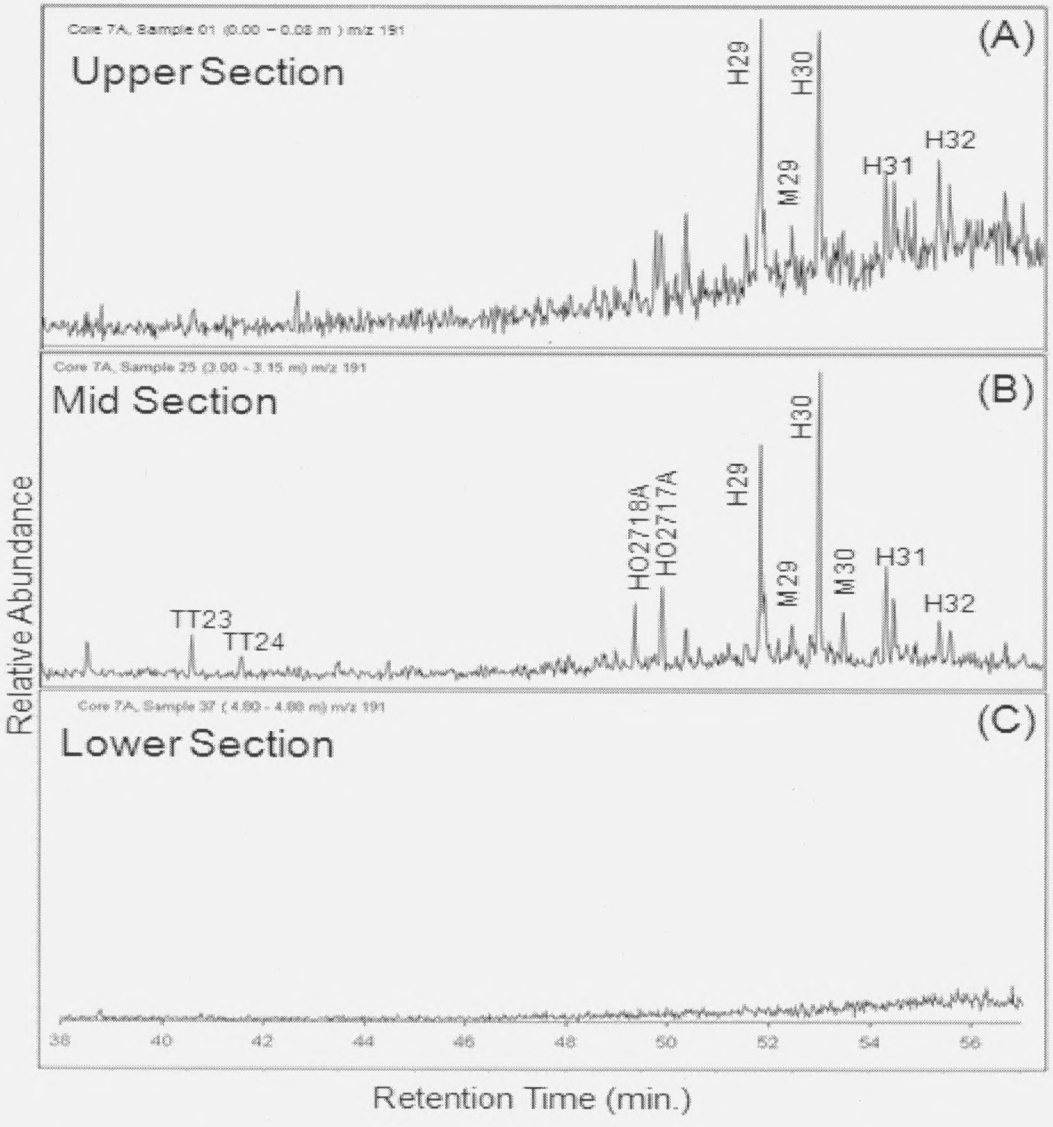

Figure 16. Py-GC/MS *m/z 191* mass chromatograms from Core 7A (RK 1.8). Data collected in full scan mode: (A) surface sample 01, 0.00 – 0.08 m depth segment; (B) sample 25, 3.00 – 3.15 m depth segment ; (C) sample 37, 4.80 – 4.88 m depth segment. Hopanes 29 – 32 are represented as well as moretane 29, see Table 7 for in additional code translations.

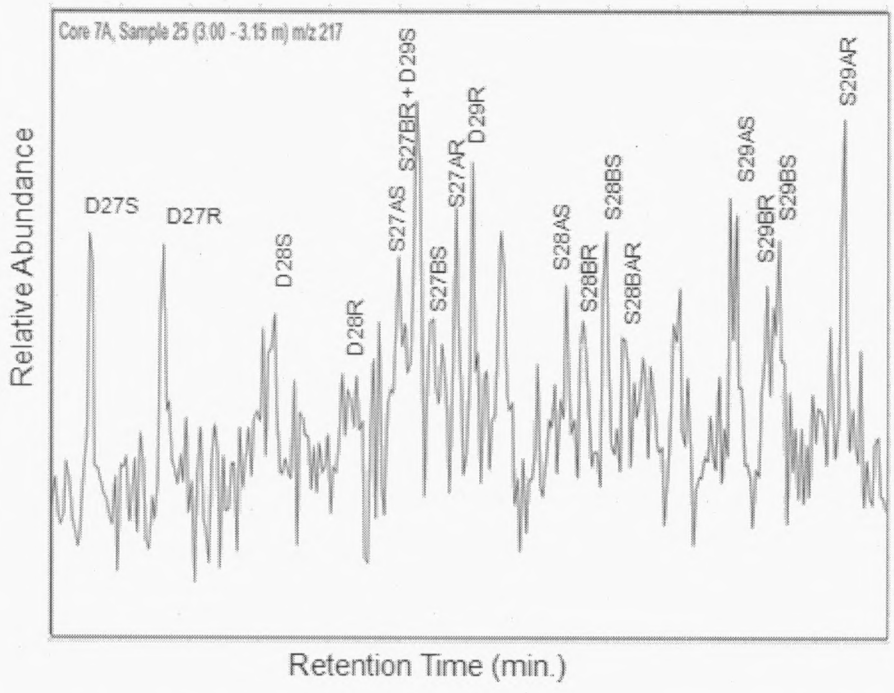

Figure 17. py-GC/MS *m/z 217* mass chromatogram from Core 7A (RK 1.8) illustrating the sterane series. Data collected in full scan mode. Sample 25, 3.00 – 3.15 m depth segment. See Table 7 for code translations.

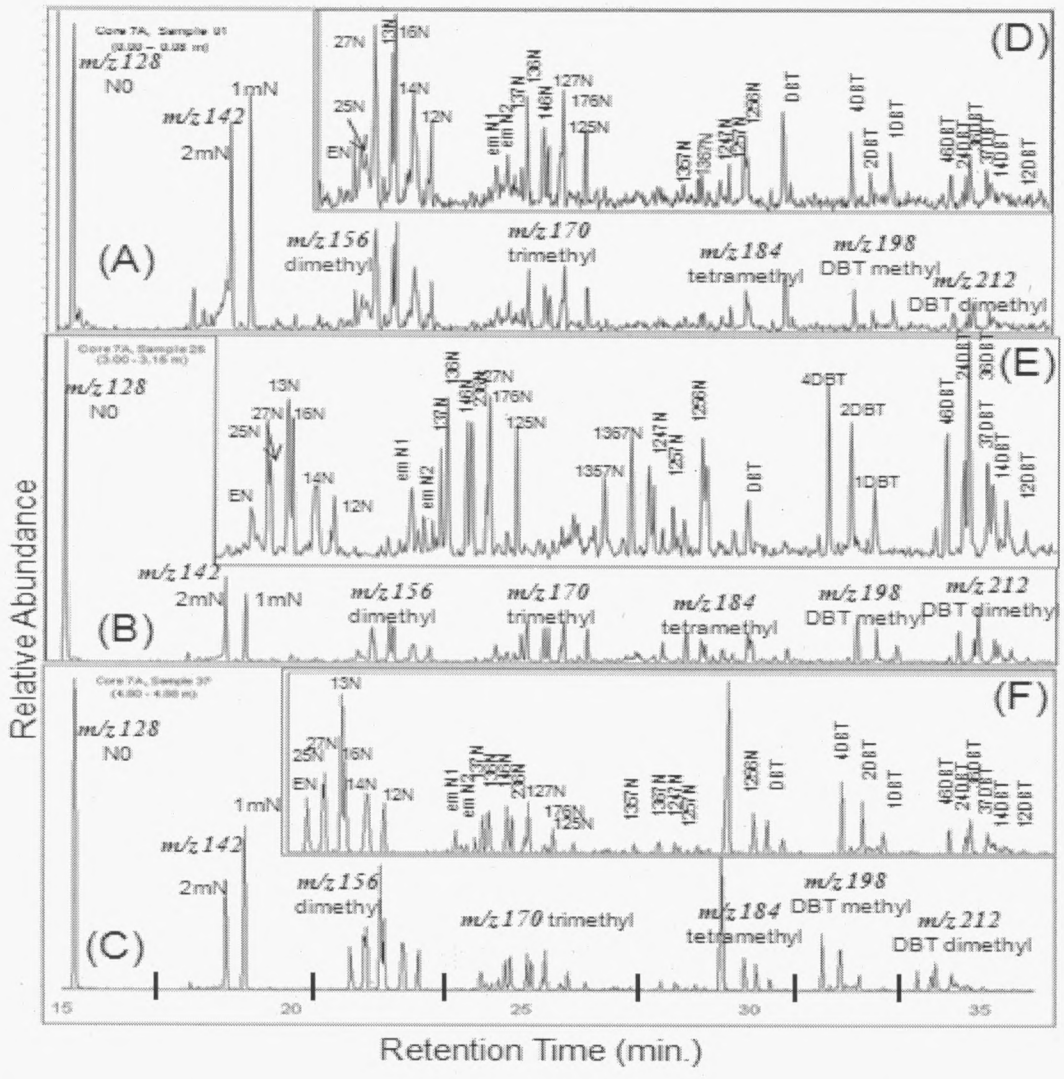

Figure 18. py-GC/MS composite mass chromatograms from Core 7A (RK 1.8) for napthalene and dibenzenethiophene series. *m/z 128* is represented, followed by *m/z 142, m/z 156, m/z 170, m/z 184, m/z 198*, and *m/z 212*. Data collected in full scan mode: (A) surface sample 01, 0.00 – 0.08 m depth segment; (B) sample 25, 3.00 – 3.15 m depth segment; (C) sample 37, 4.80 – 4.88 m depth segment. Chromatograms (D), (E), and (F) are enlarged representations of *m/z 156 – m/z 212* from their respective plots (A), (B), and (C). See Table 7 for code translations.

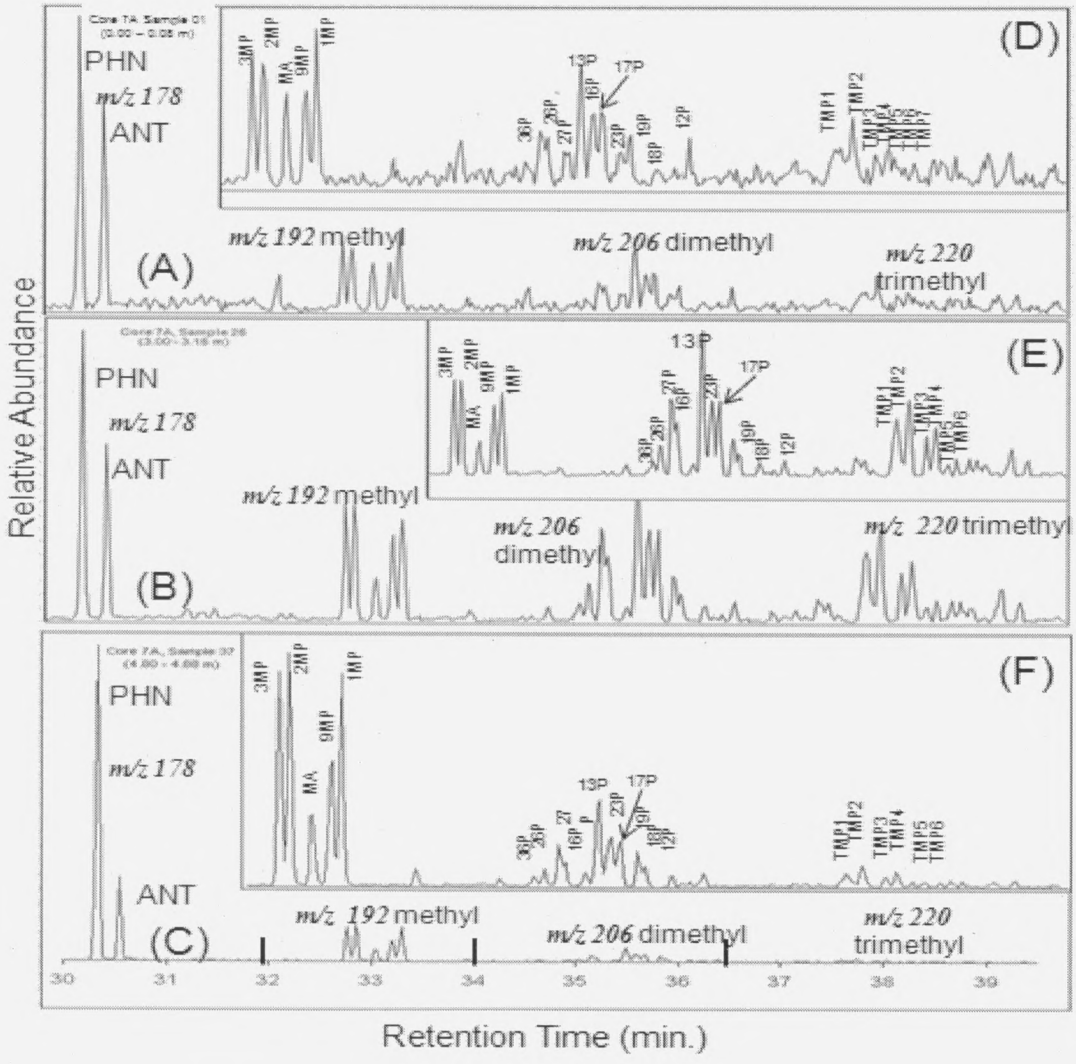

Figure 19. py-GC/MS composite mass chromatograms from Core 7A (RK 1.8) for phenanthrene series. *m/z 178* is represented, followed by *m/z 192, m/z 206,and m/z 220*. Data collected in full scan mode: (A) surface sample 01, 0.00 – 0.08 m depth segment; (B) sample 25, 3.00 – 3.15 m depth segment; (C) sample 37, 4.80 – 4.88 m depth segment. Chromatograms (D), (E), and (F) are enlarged representations of *m/z 192 – m/z 220* from their respective plots (A), (B), and (C). See Table 7 for code translations.

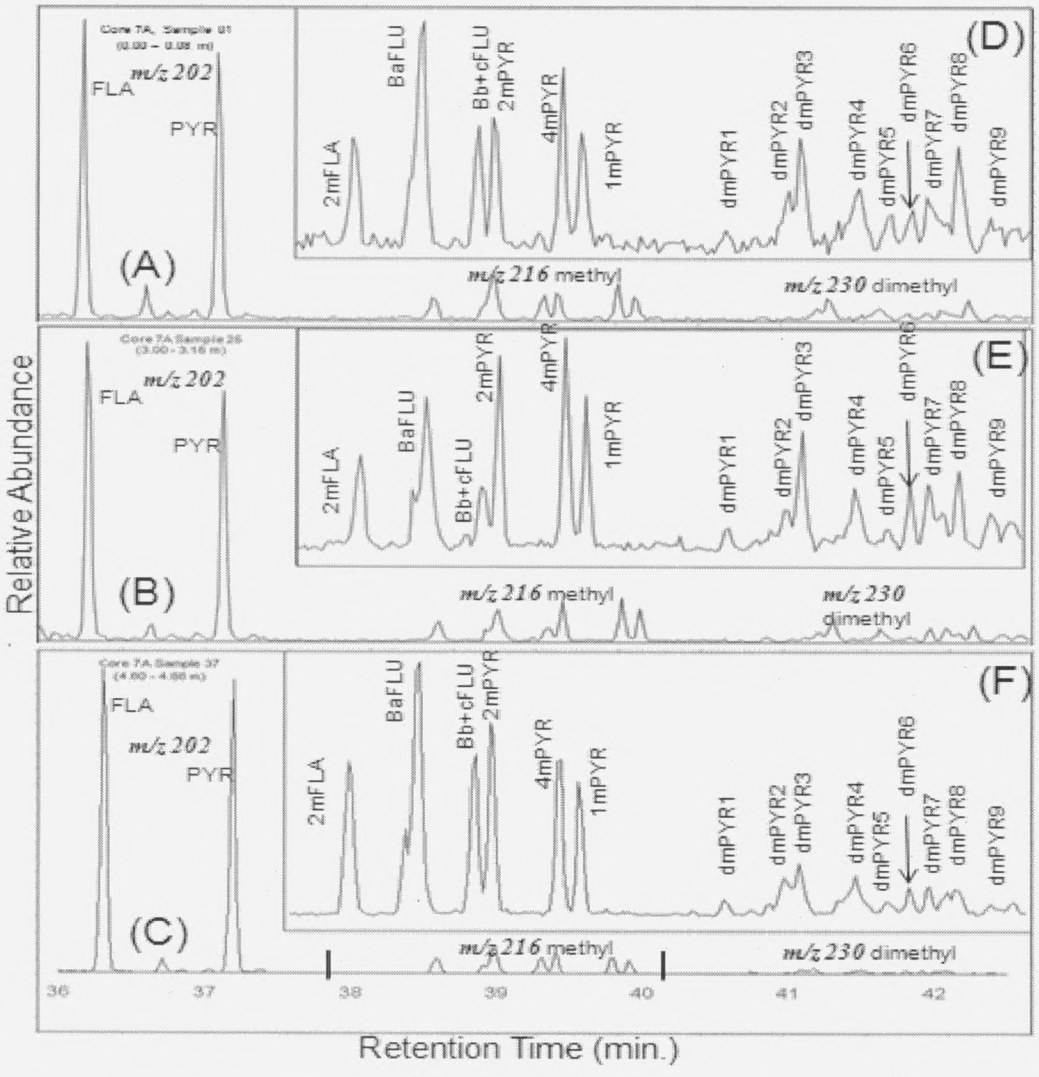

Figure 20. Py-GC/MS composite mass chromatograms from Core 7A (RK 1.8) for pyrene series. *m/z 202* is represented, followed by *m/z 216*, and *m/z 230*. Data collected in full scan mode: (A) surface sample 01, 0.00 – 0.08 m depth segment; (B) sample 25, 3.00 – 3.15 m depth segment; (C) sample 37, 4.80 – 4.88 m depth segment. Chromatograms (D), (E), and (F) are enlarged representations of *m/z 216* and *m/z 230* from their respective plots (A), (B), and (C). See Table 7 for code translations.

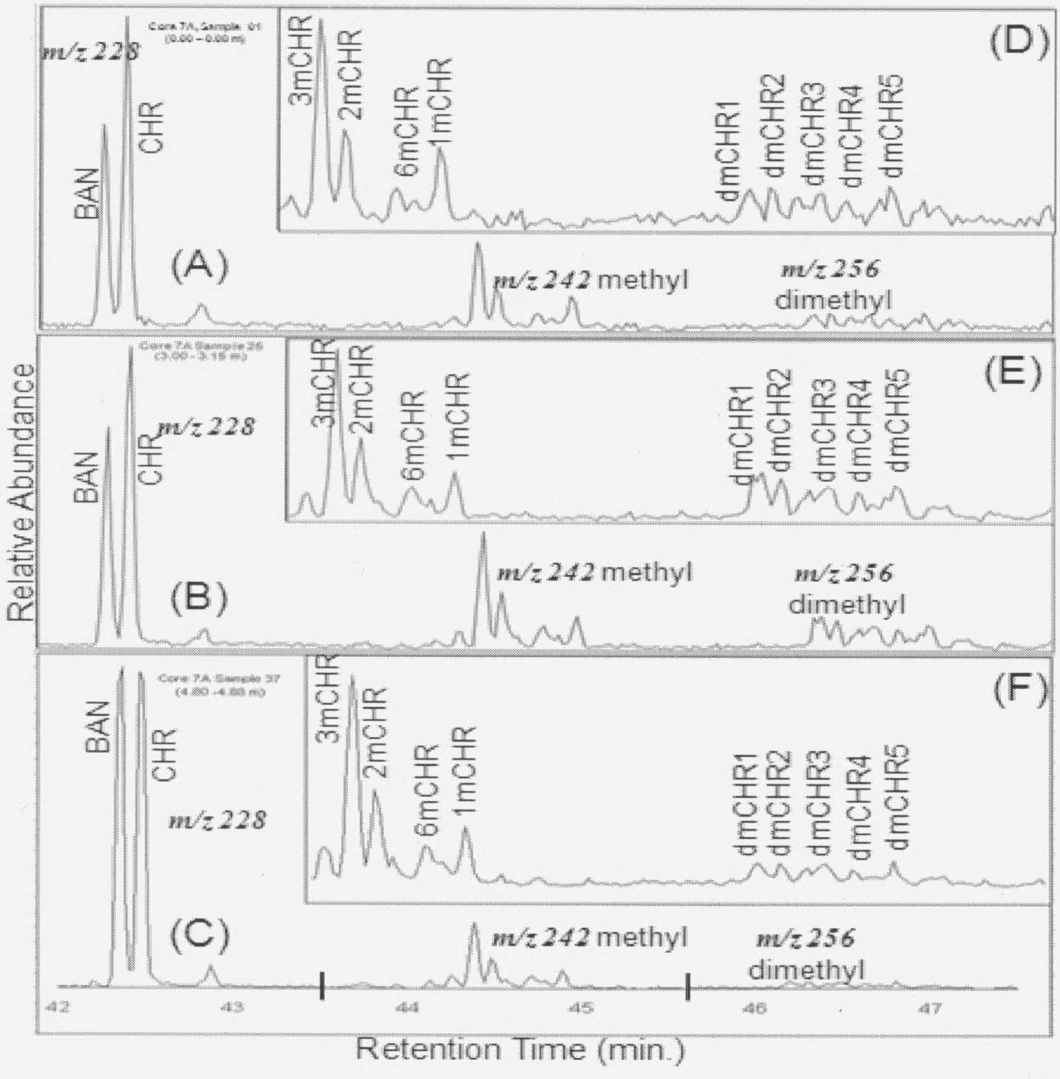

Figure 21. Py-GC/MS composite mass chromatograms from Core 7A (RK 1.8) for chrysene series. *m/z 228* is represented, followed by *m/z 242*, and *m/z 256*. Data collected in full scan mode: (A) surface sample 01, 0.00 - 0.08 m depth segment; (B) sample 25, 3.00 – 3.15 m depth segment; (C) sample 37, 4.80 – 4.88 m depth segment. Chromatograms (D), (E), and (F) are enlarged representations of *m/z 242* and *m/z 256* from their respective plots (A), (B), and (C). See Table 7 for code translations.

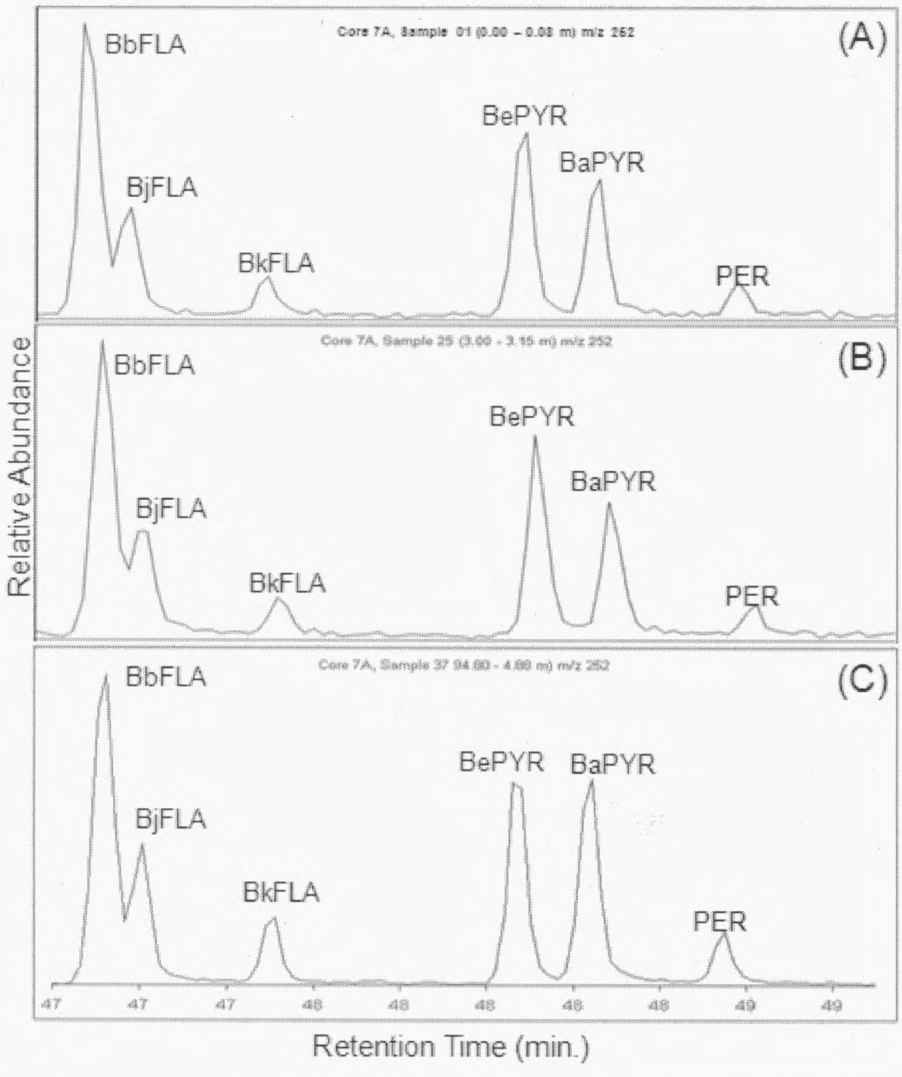

Figure 22. Py-GC/MS *m/z 252* mass chromatograms from Core 7A (RK 1.8) illustrating the benzopyrene series. Data collected in full scan mode: (A) surface sample 01, 0.00 - 0.08 m depth segment; (B) sample 25, 3.00 – 3.15 m depth segment ; (C) sample 37, 4.80 – 4.88 m depth segment. See Table 7 for code translations.

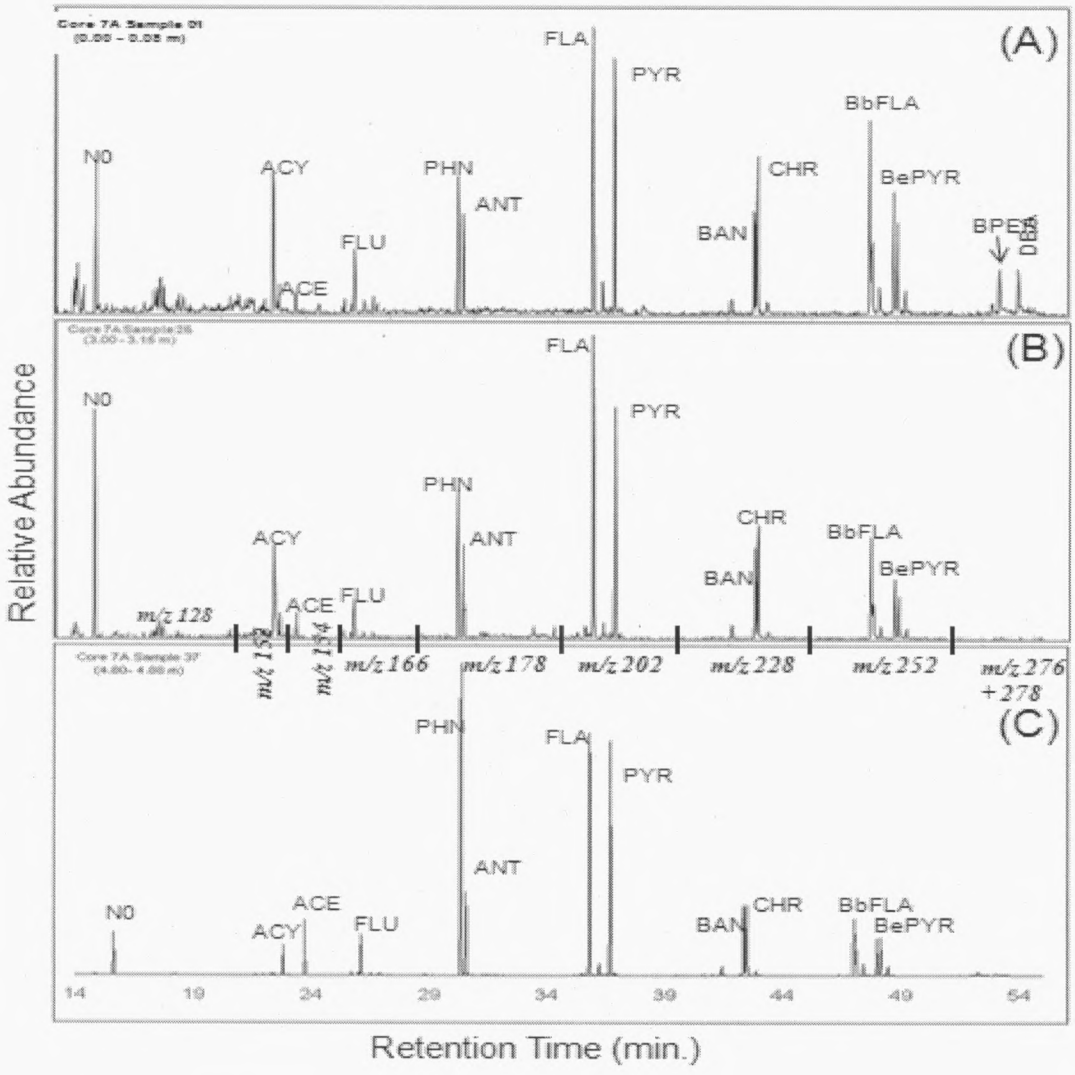

Figure 23. Py-GC/MS composite mass chromatograms from Core 7A (RK 1.8) illustrating the16 PAHs listed on the USEPA priority pollutant list. *m/z 128* is represented, followed by *m/z 152, m/z 154, m/z 178, m/z 202, m/z 228*, and *m/z 276 +278* (summed). Data collected in full scan mode: (A) surface sample 01, 0 -0.75 m depth segment; (B) sample 25, 3.00 – 3.15 m depth segment; (C) sample 37, 4.80 – 4.88 m depth segment. See Table 7 for code translations.

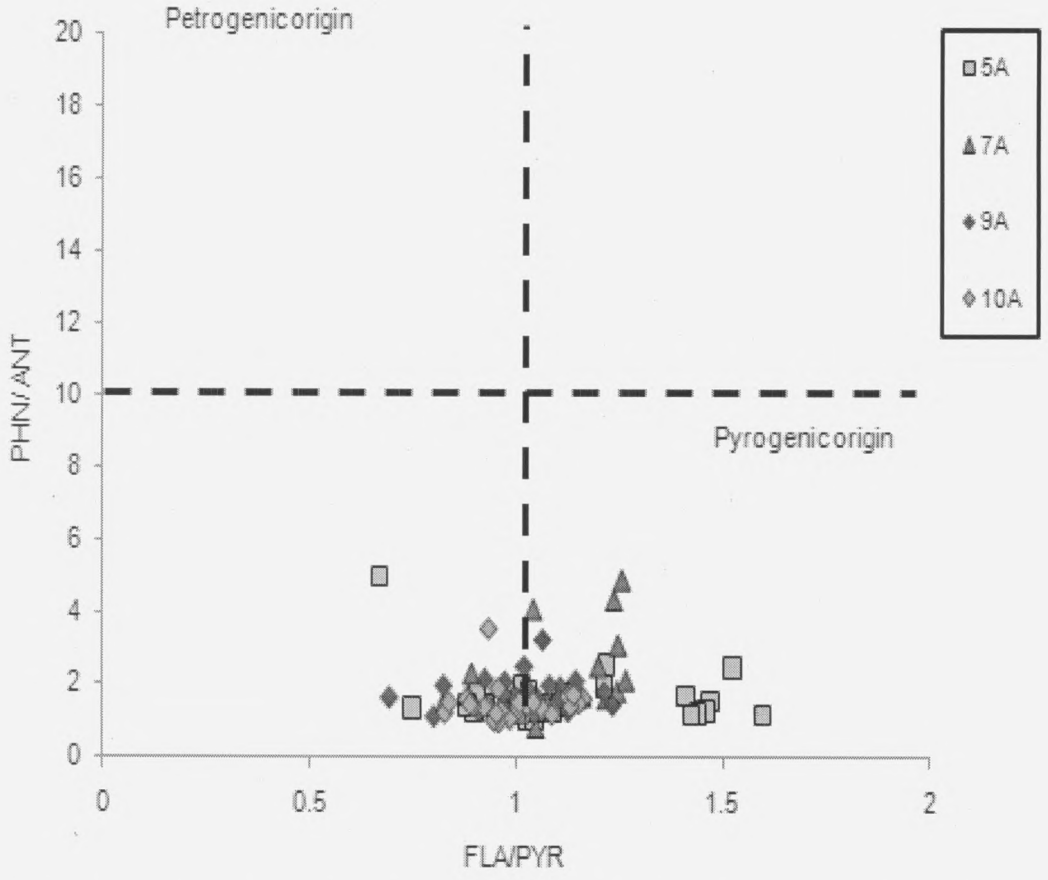

Figure 24. PAH Cross Plot : FLA/PYR & PHN/ANT. Core 5A is located at RK 1.8, Core 7A is located at RK 2.3, Core 9A is located at RK 3.5, and RK for Core 10A 2.6 RK.

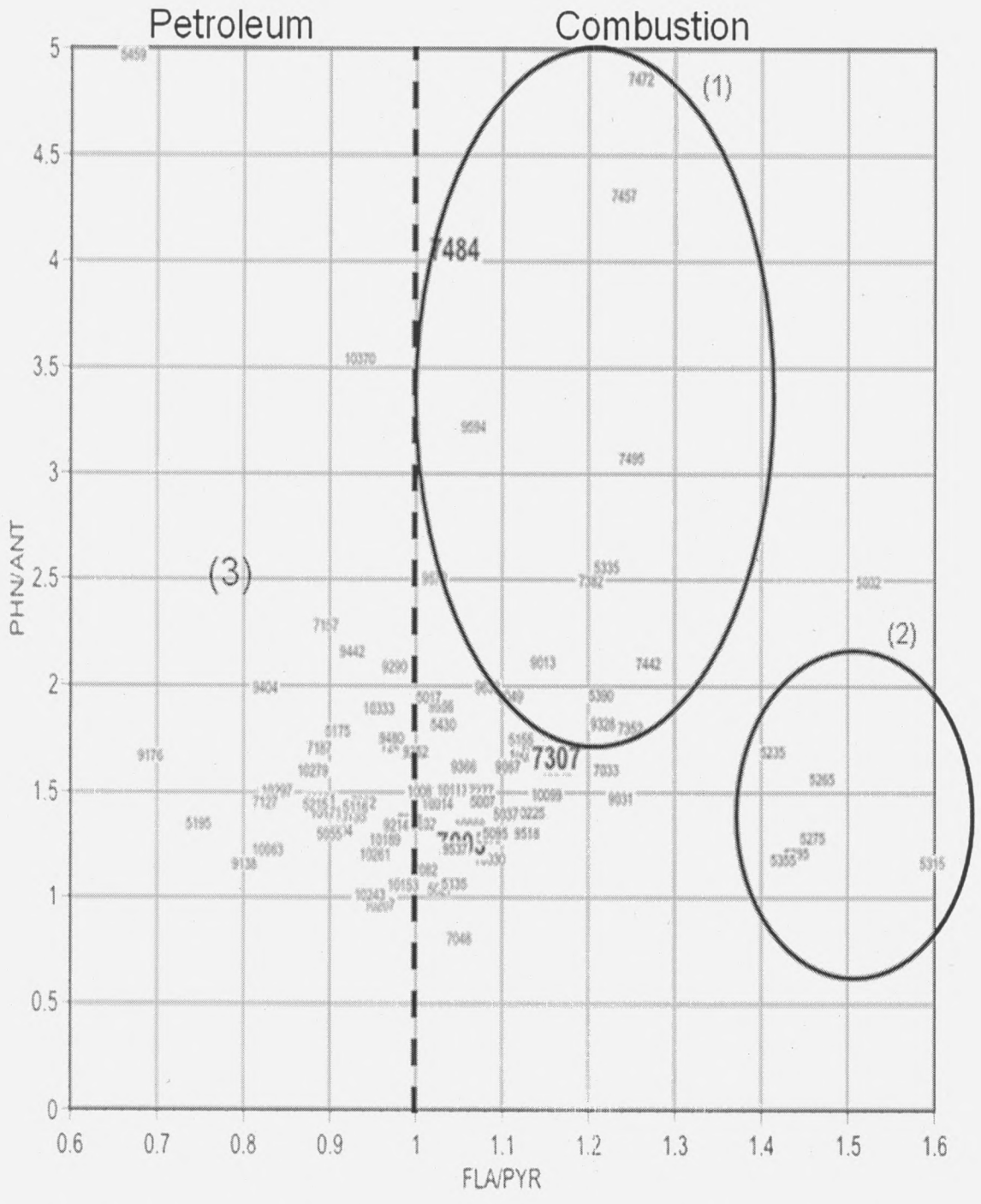

Figure 25. Detail of Figure 24. PAH Cross Plot: FLA / PYR & PHN/ANT, additionally displaying core number and depth per data point. Group (1) and (2) represent samples which have been observed to contain high concentrations of PAH compounds. Plot done in delta graph.

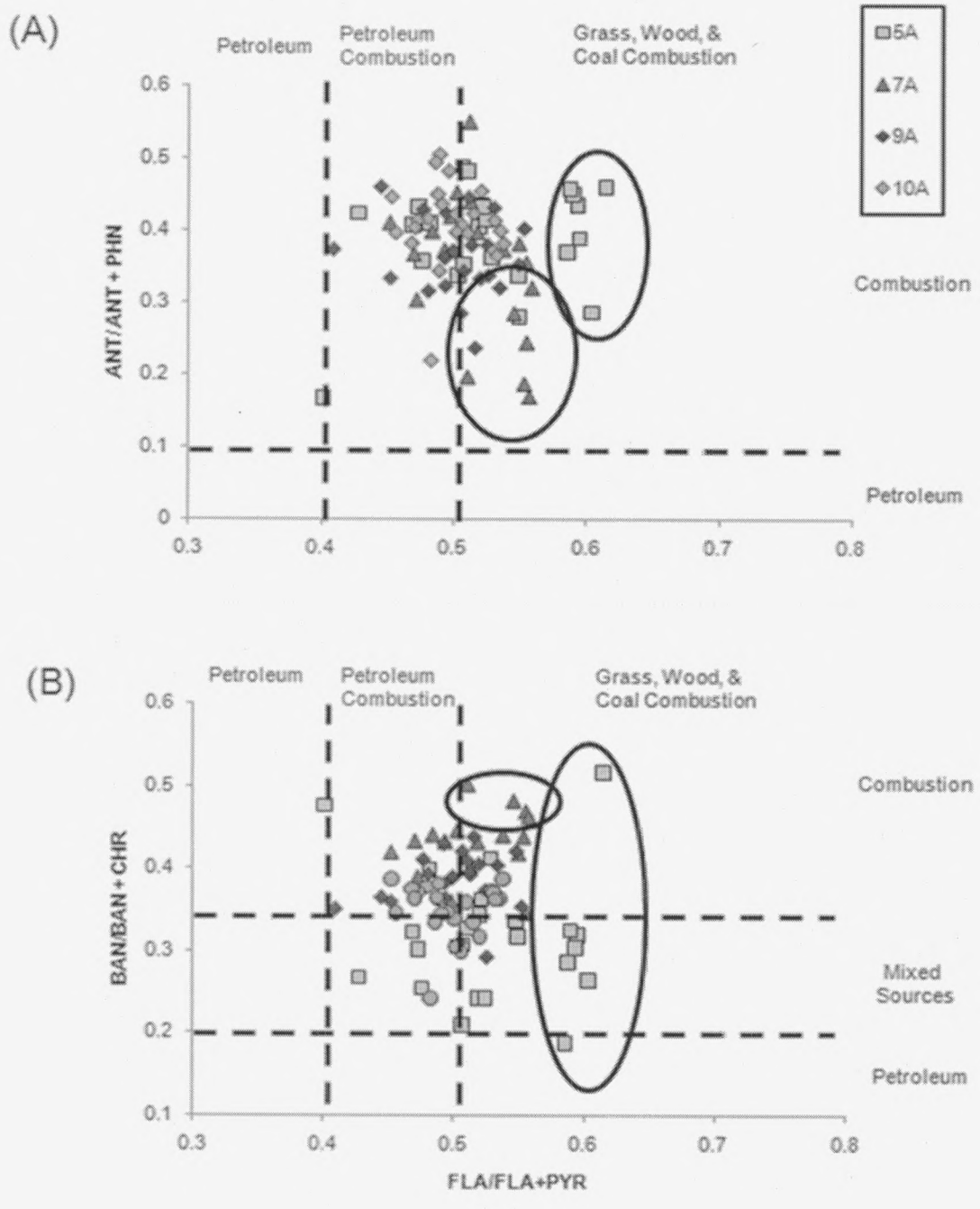

Figure 26. PAH Cross Plot: FLA/ (FLA + PYR) & (A): PHN/ ANT; (B): BAN/ (BAN + CHR)

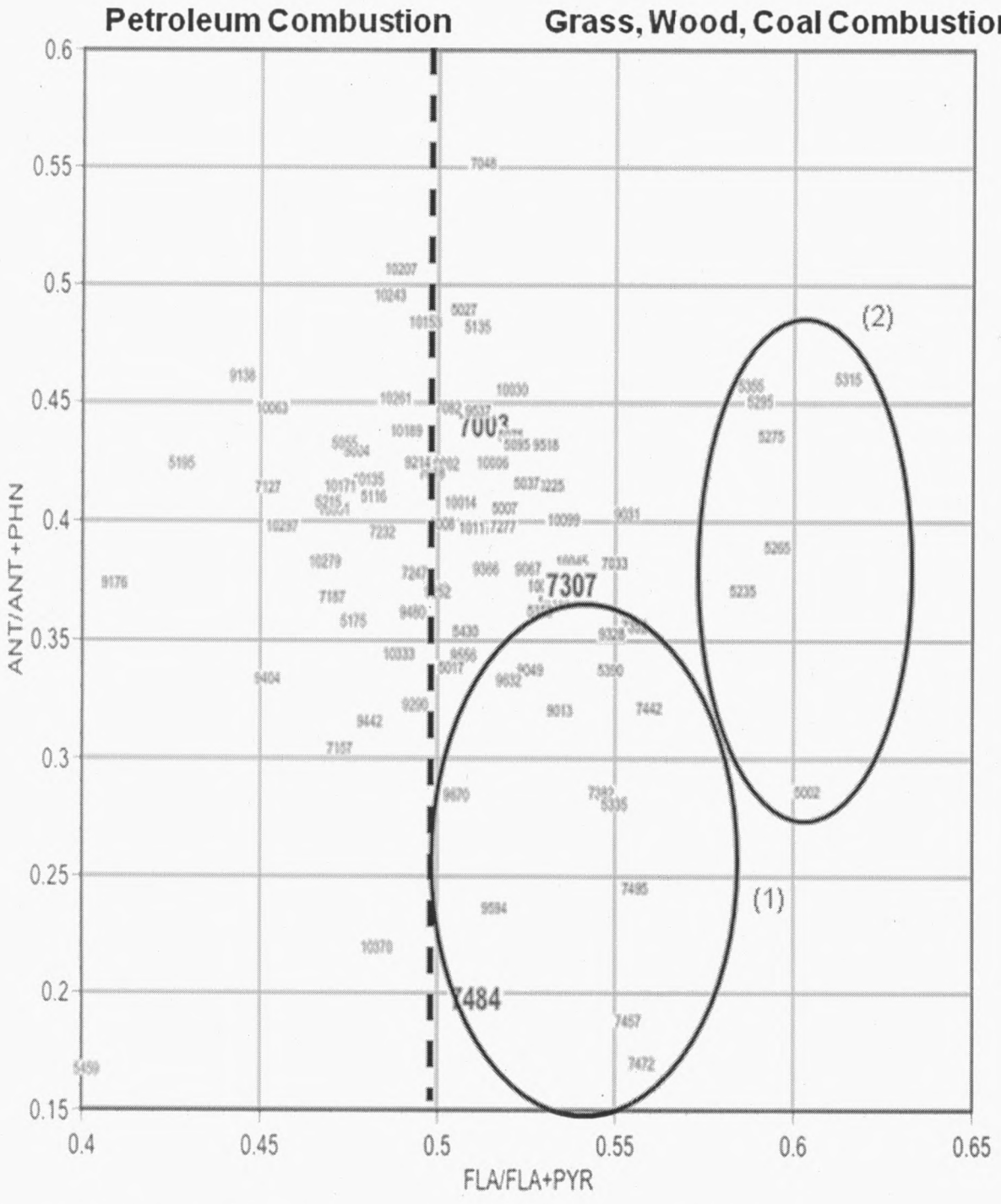

Figure 27. Detail of Figure 26A. PAH Cross Plot: FLA/ (FLA + PYR) & (PHN/ ANT) additionally displaying core number and depth per data point. Group (1) and (2) represent samples which have been observed to contain high concentrations of PAH compounds. Plot done in delta graph.

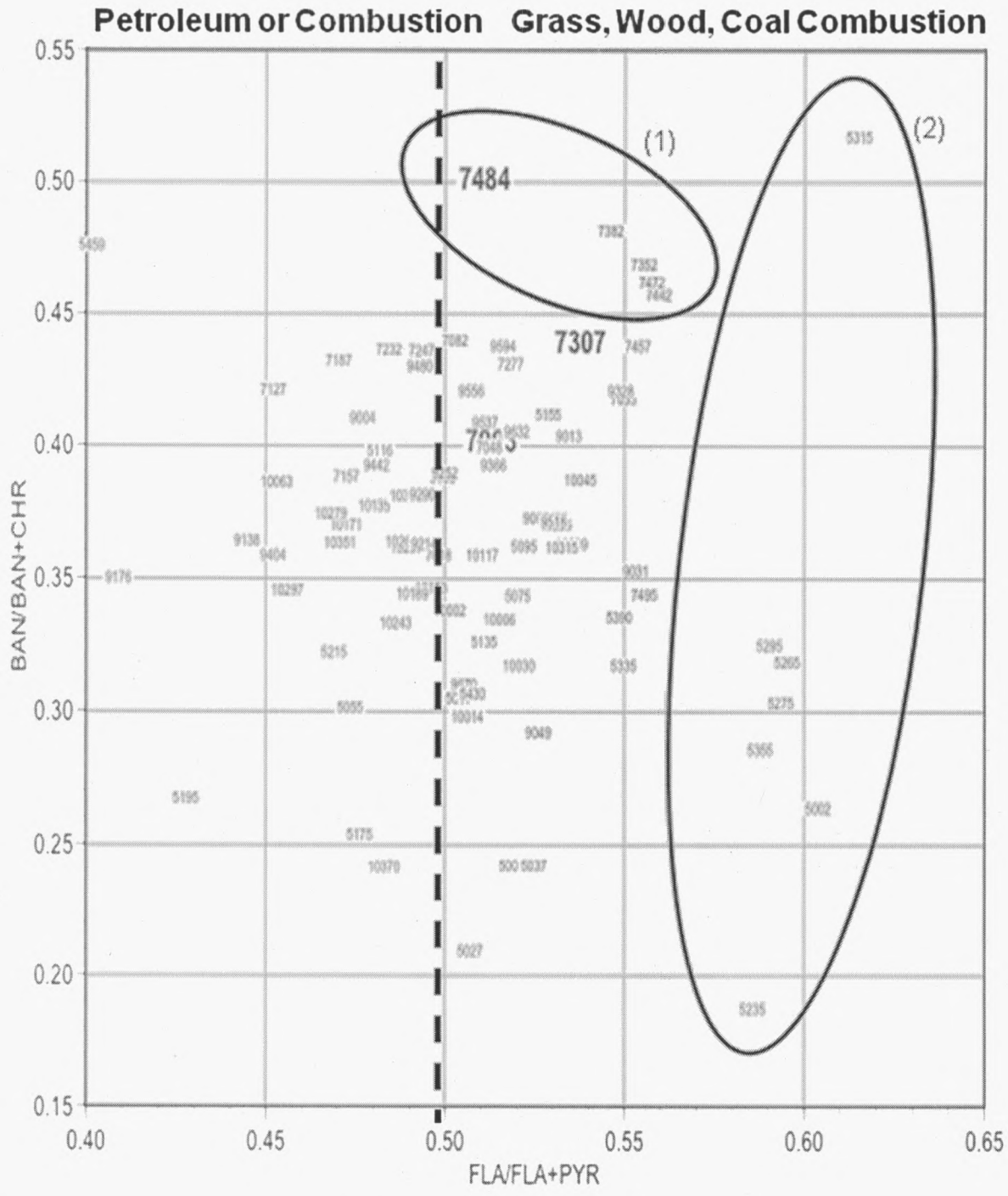

Figure 28. Detail of Figure 26B. PAH Cross Plot: FLA/ (FLA + PYR) & BAN/ (BAN + CHR) additionally displaying core number and depth per data point. Group (1) and (2) represent samples which have been observed to contain high concentrations of PAH compounds. Plot done in delta graph.

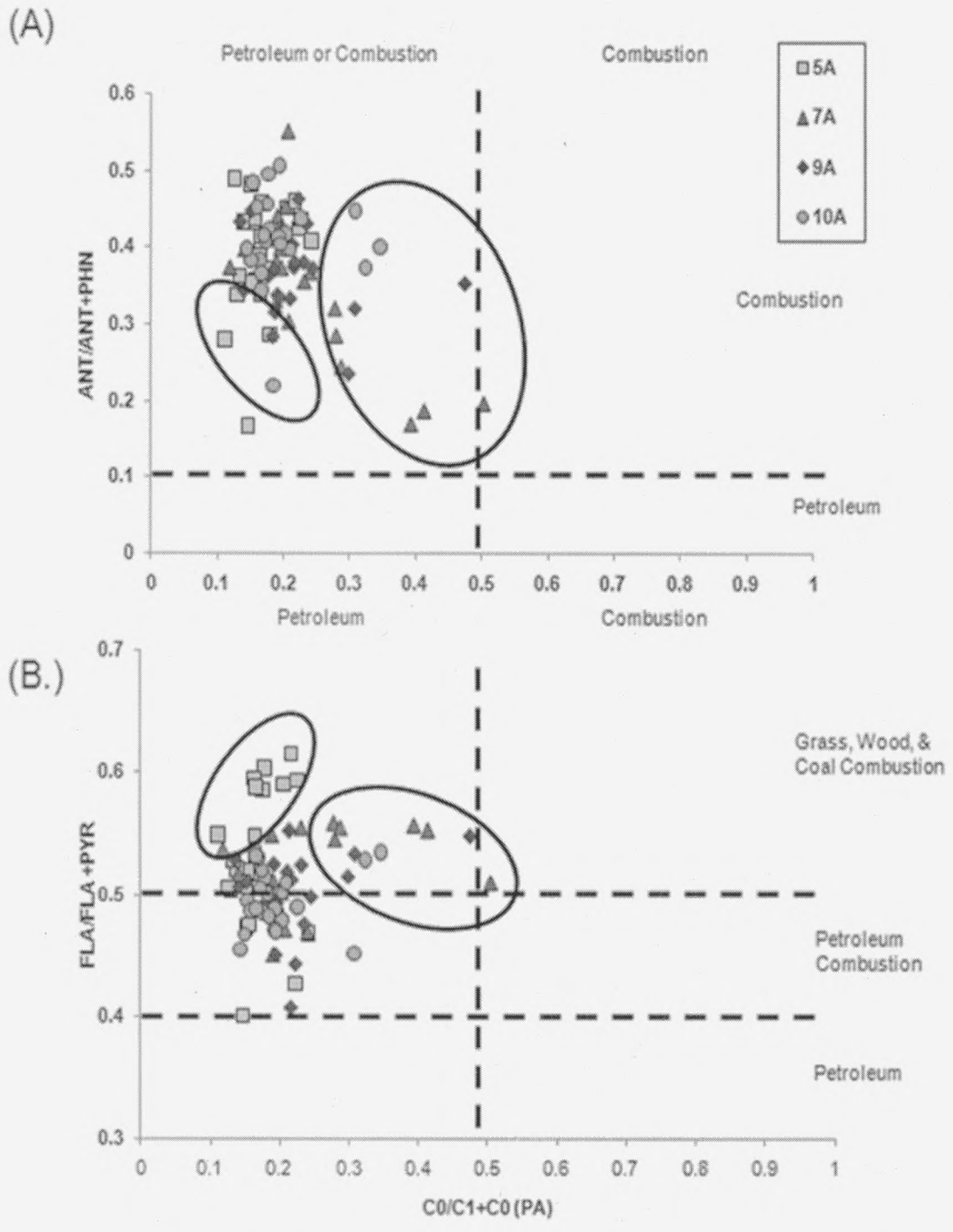

Figure 29. PAH Cross Plot (PHN + ANT) /(PHN + ANT + + C_1-PHN + C_1-ANT) vs. (A):ANT/(PHN + ANT); (B): FLA/ (FLA + PYR)

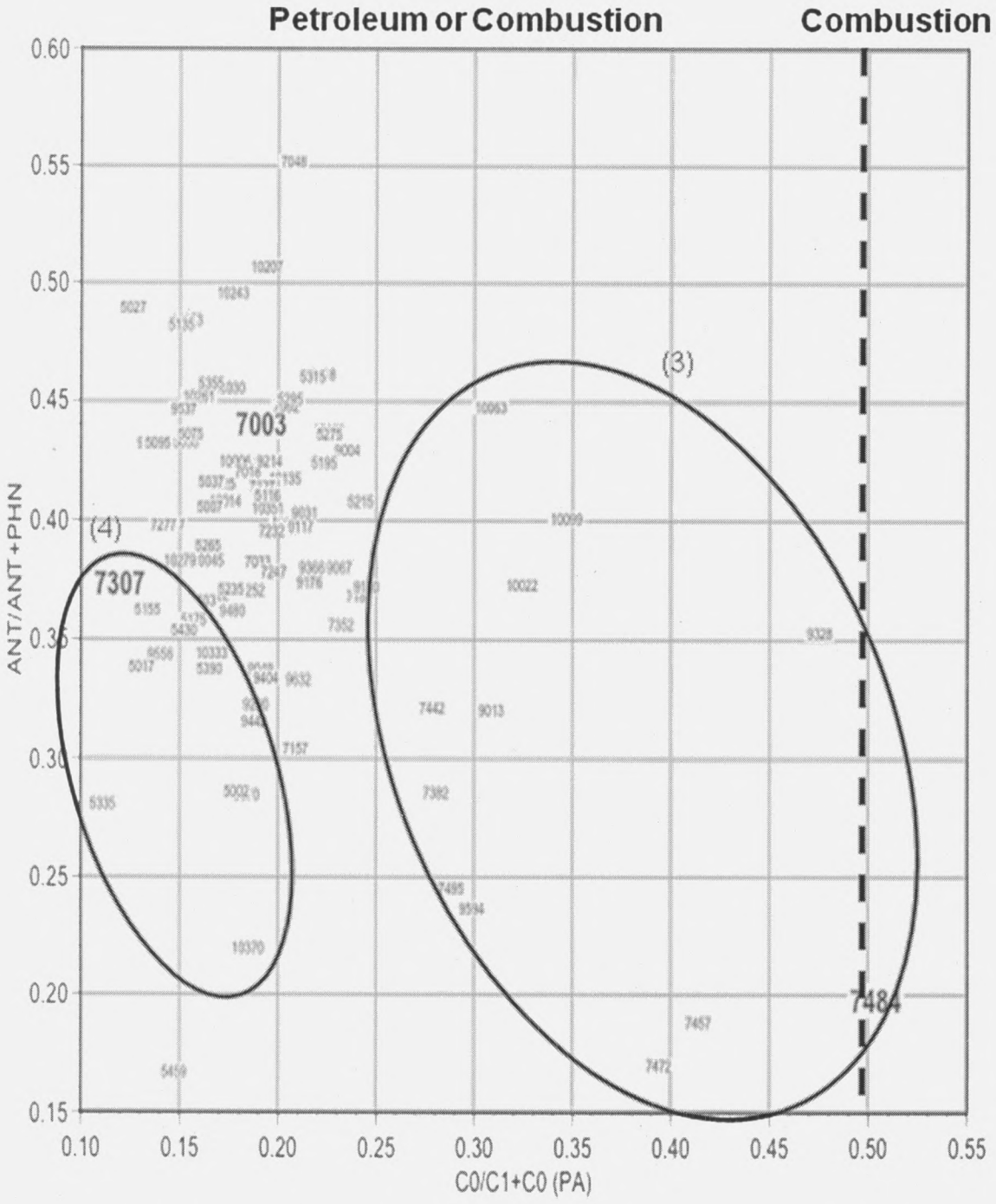

Figure 30. Detail of Figure 29A. PAH Cross Plot (PHN + ANT) /(PHN + ANT + C_1-PHN + C_1-ANT) vs. ANT/(PHN + ANT), additionally displaying core number and depth per data point. Group (3) represent samples which have been observed to contain high concentrations of PAH compounds. Group (4) represents samples which have displayed a petroleum signature. Plot done in delta graph.

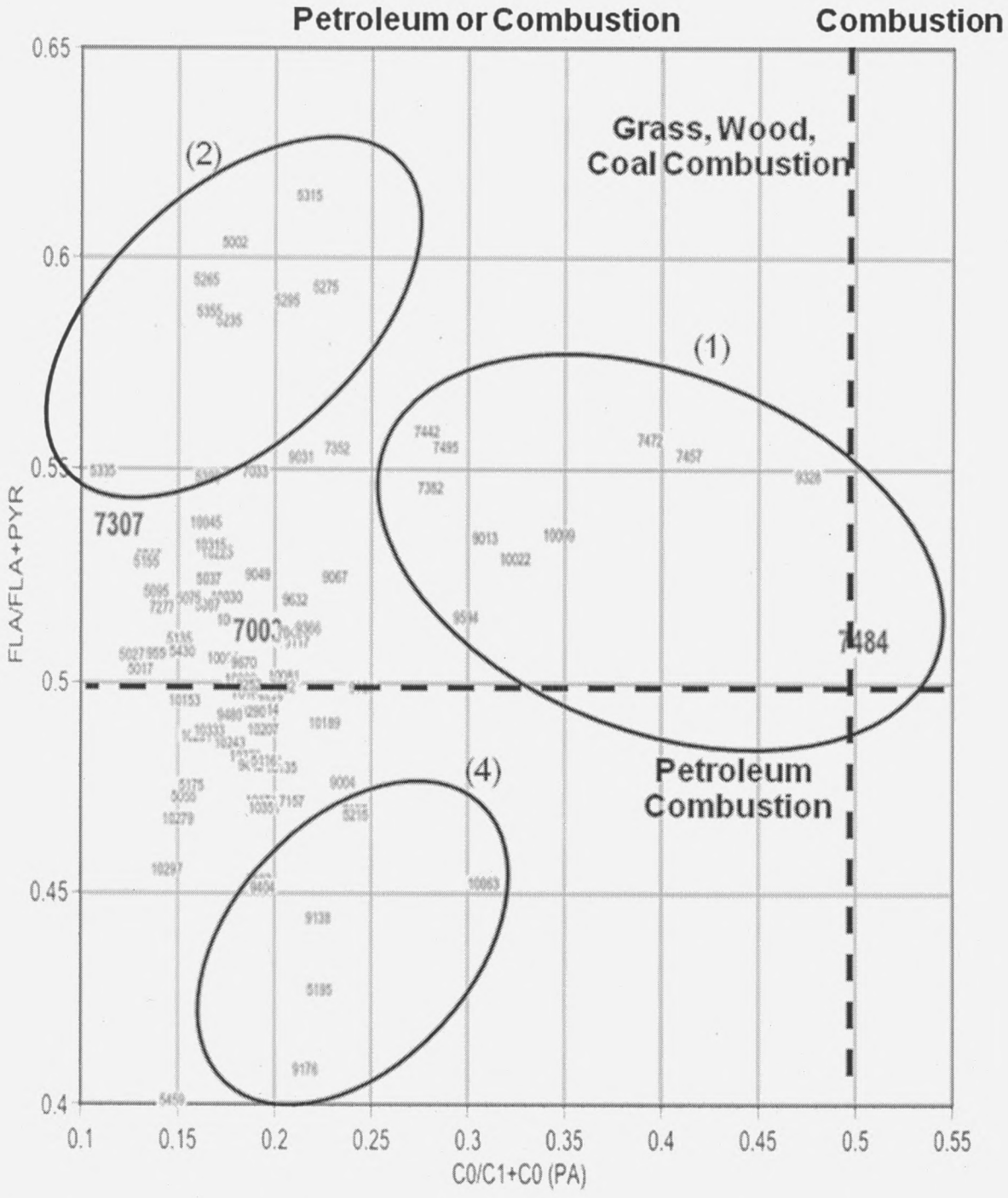

Figure 31. Detail of Figure 29B. PAH Cross Plot (PHN + ANT) / (PHN + ANT + C_1-PHN + C_1-ANT) vs. FLA / (FLA + PYR), additionally displaying core number and depth per data point. Group s (1) & (2) represent samples which have been observed to contain high concentrations of PAH compounds. Group (4) represents samples which have displayed a petroleum signature. Plot done in delta graph.

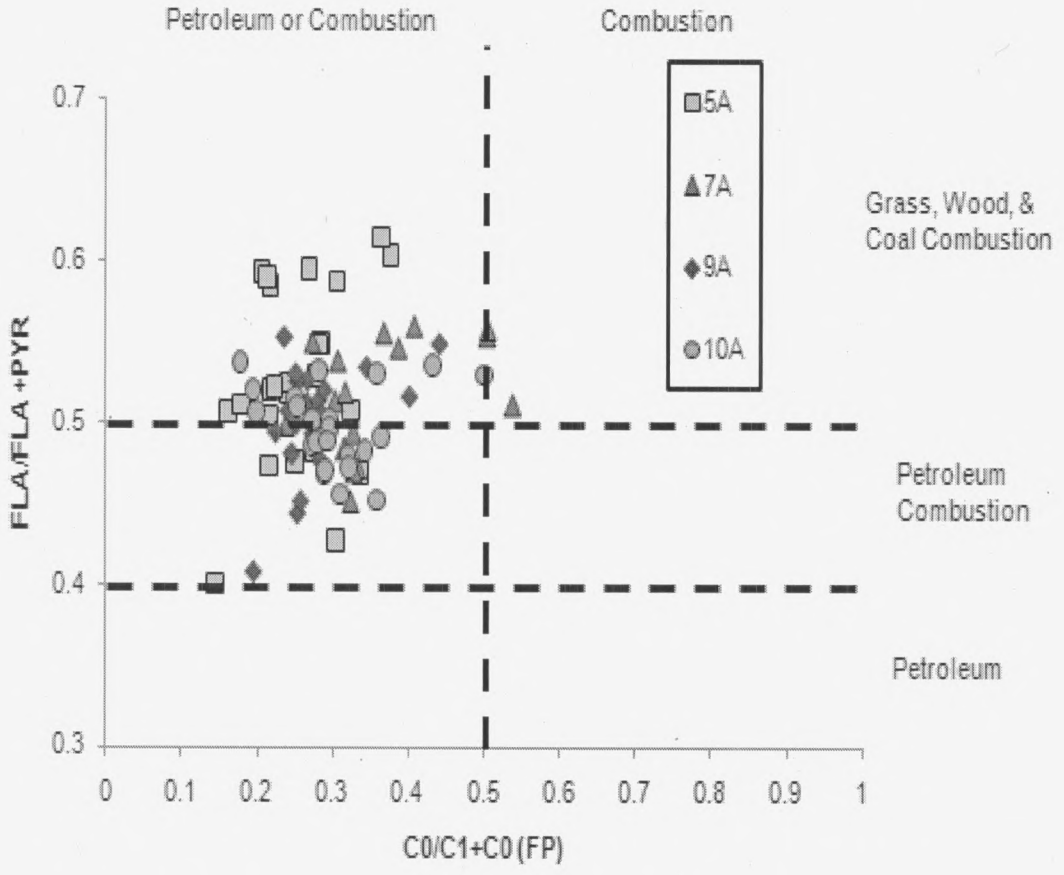

Figure 32. PAH Cross Plot (FLA + PYR) / (FLA + PYR + C_1-PYR) vs. FLA/ (FLA + PYR)

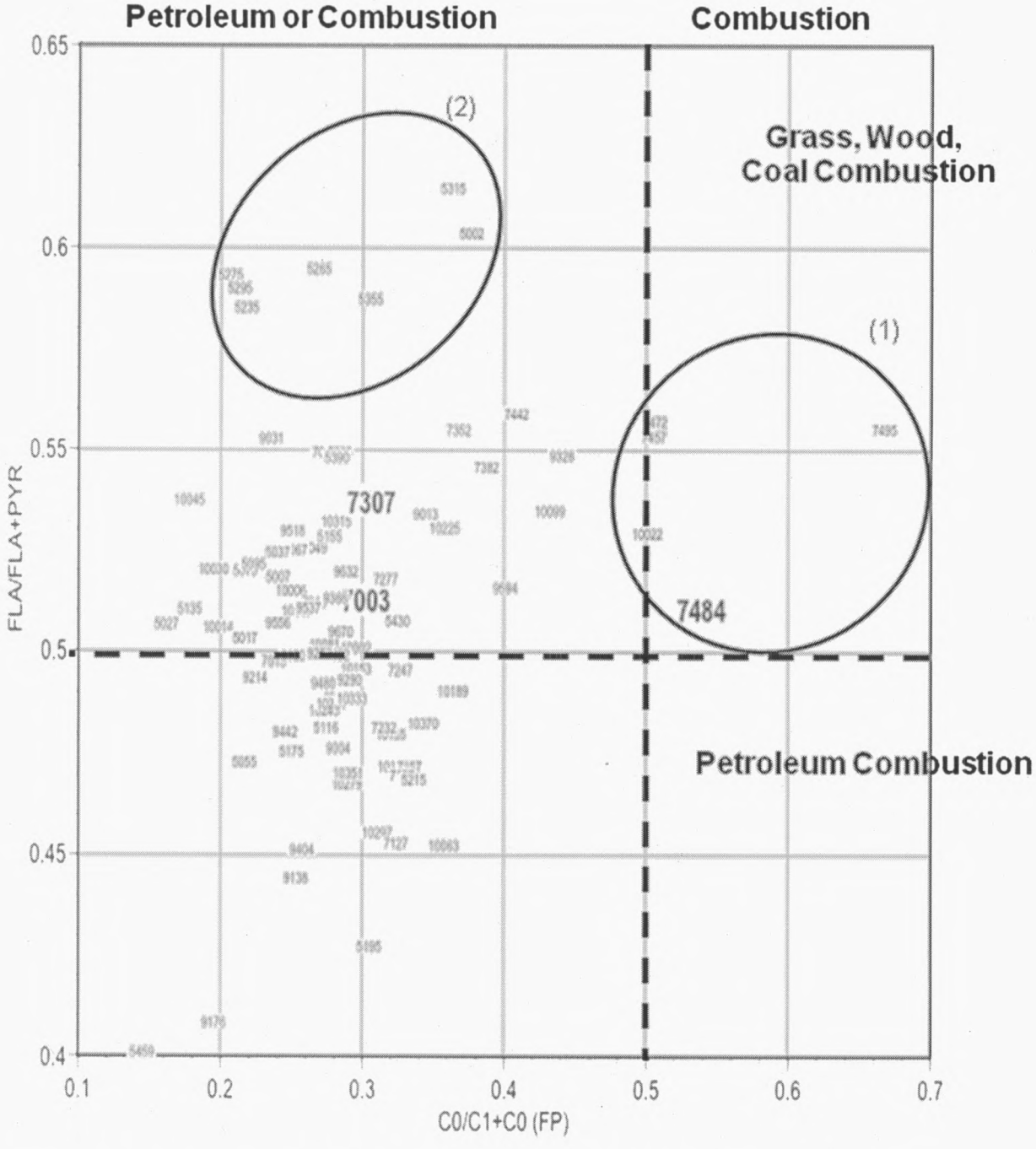

Figure 33. Detail of Figure 32. PAH Cross Plot (FLA + PYR) / (FLA + PYR + C1) vs. FLA/ (FLA + PYR), additionally displaying core number and depth per data point. Group(1) and (2) represent samples which have been observed to contain high concentrations of PAH compounds. Plot done in delta graph.

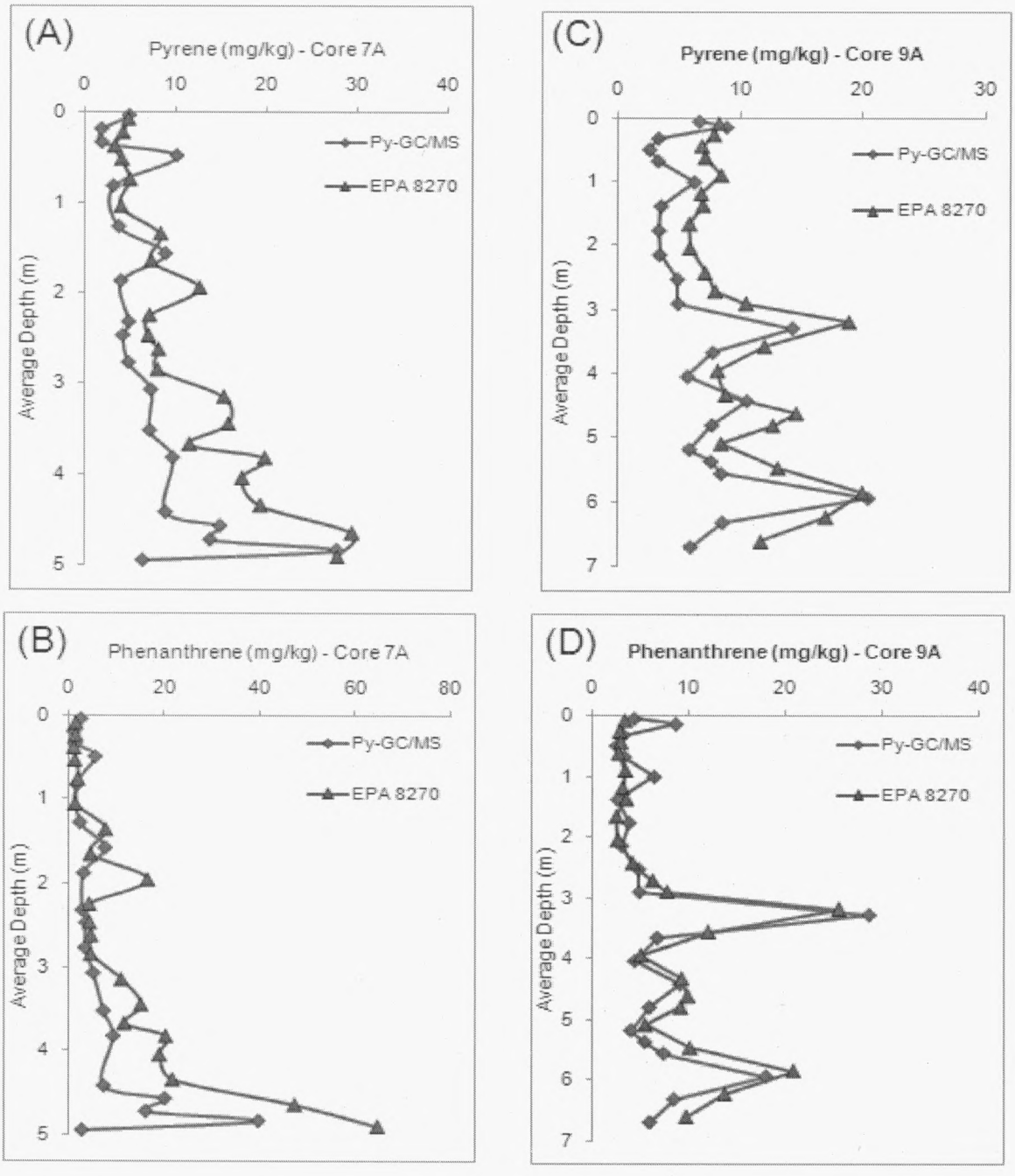

Figure 34. Comparison of pyrene and phenanthrene concentrations analyzed by Py-GC/MS & the EPA 8270 method (EPA method data from LPRRP, 2008).(A) & (B) represent core 7A with pyrene(A) and phenanthrene (B) vs. average depth. (C) & (D) represent core 9A with pyrene(C) and phenanthrene (D) vs. average depth. A correlating trend occurring between the two methods should be noted.

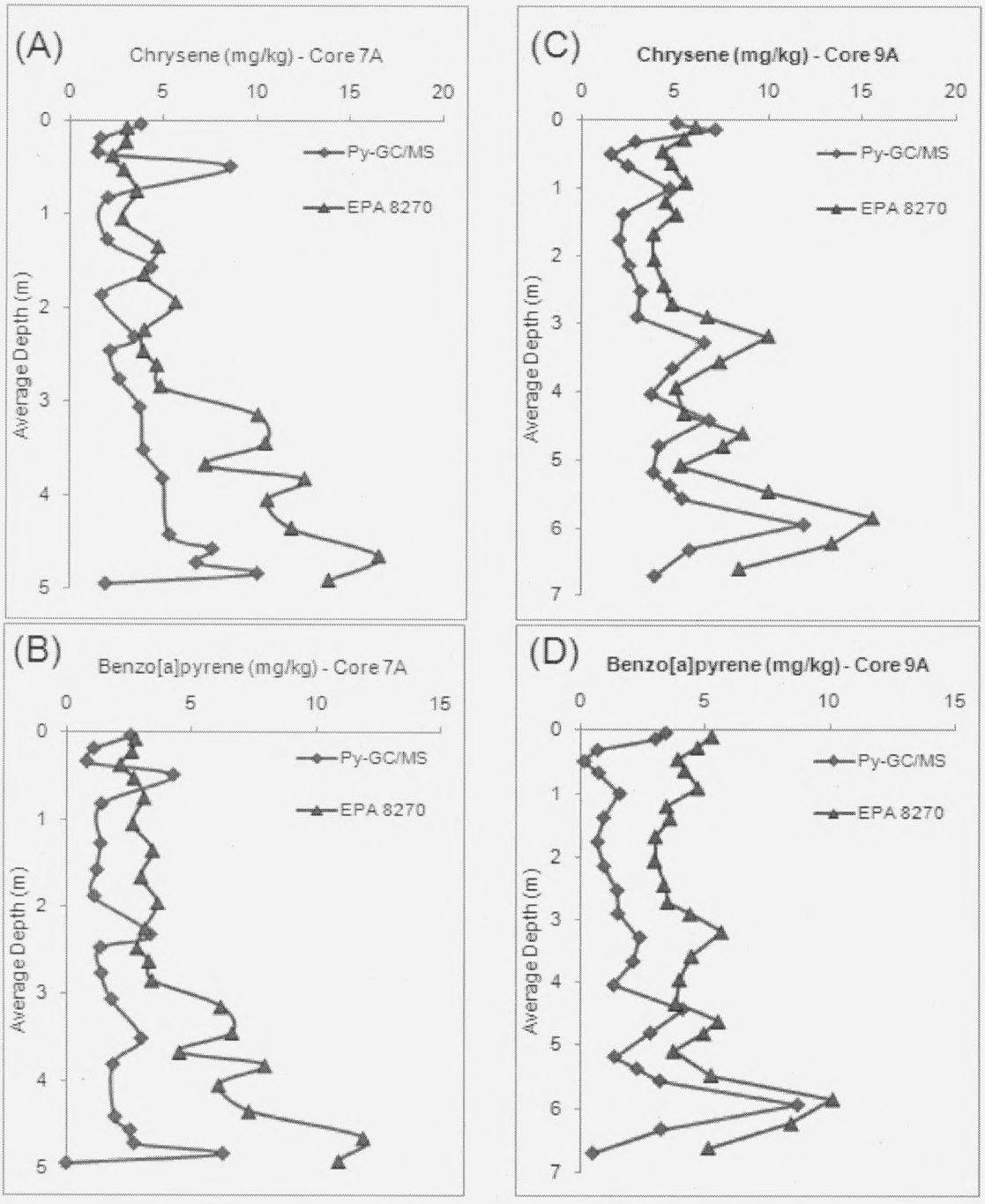

Figure 35. Comparison of chrysene and benzo(a)pyrene concentrations analyzed by Py-GC/MS & the EPA 8270 method (EPA method data from LPRRP, 2008).((A) & (B) represent core 7A chrysene (A) and benzo(a)pyrene (B) vs. average depth. (C) & (D) represent core 9A .chrysene (C) and benzo(a)pyrene (D) vs. average depth. A correlating trend occurring between the two methods should be noted.

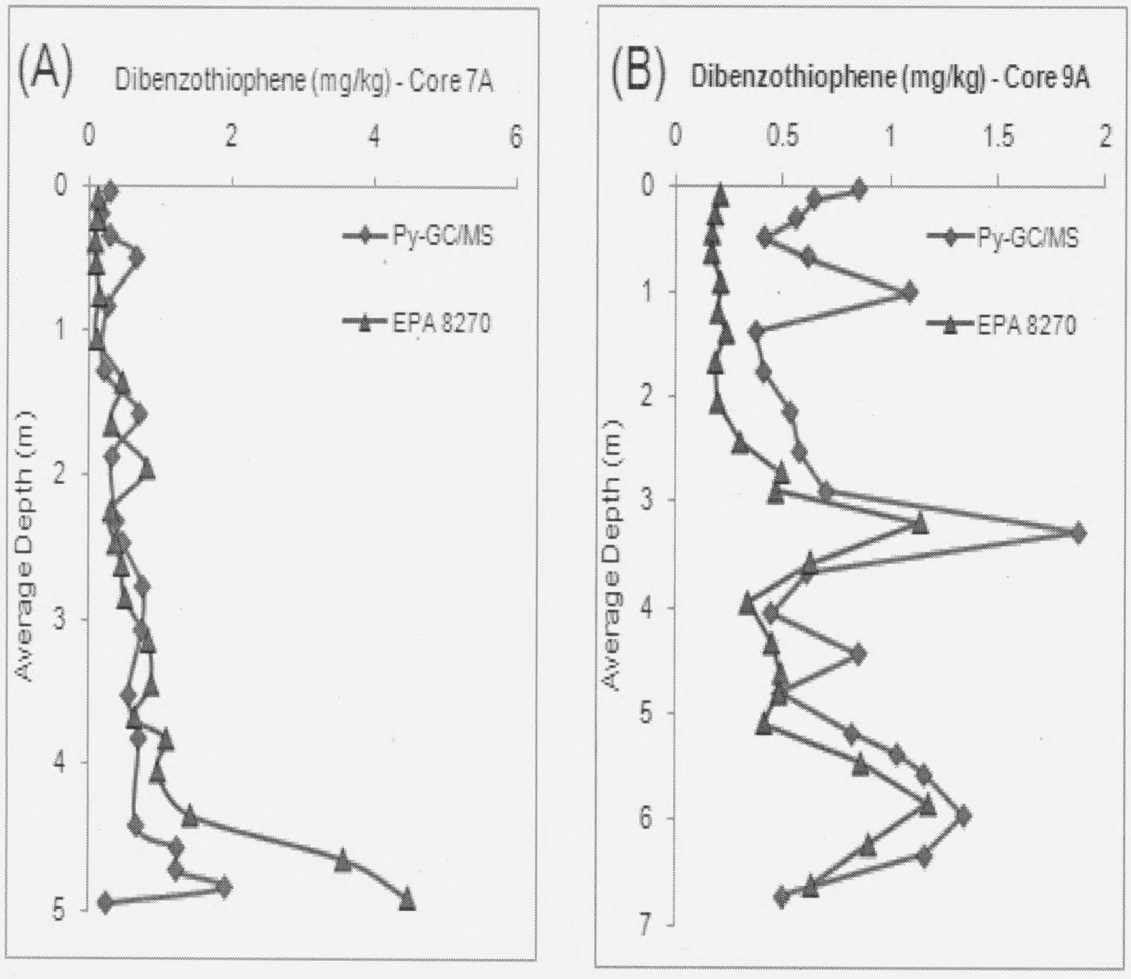

Figure 36. Comparison of dibenzothiophene concentrations analyzed by Py-GC/MS & the EPA 8270 method (EPA method data from LPRRP, 2008). (A) represents core 7A (B) represents core 9A. A correlating trend occurring between the two methods should be noted.

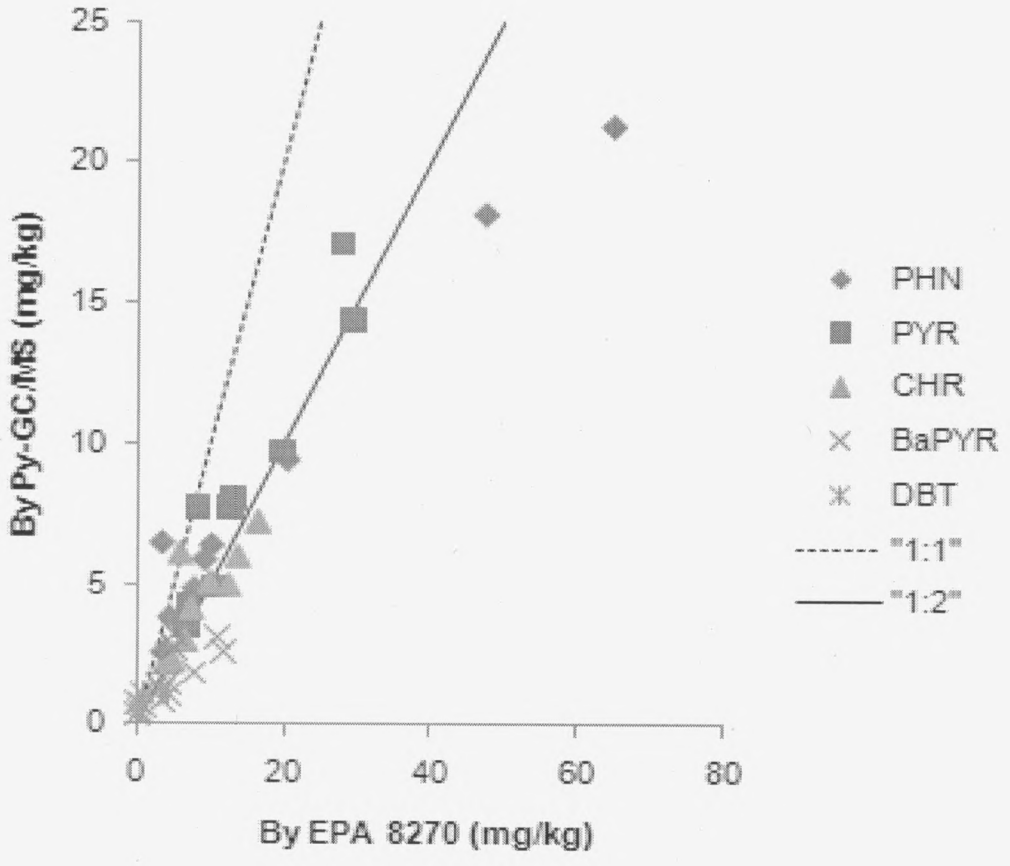

Figure 37. Concentration data : Py-GC/MS method vs. the EPA 8270 method (EPA method data from LPRRP, 2008)

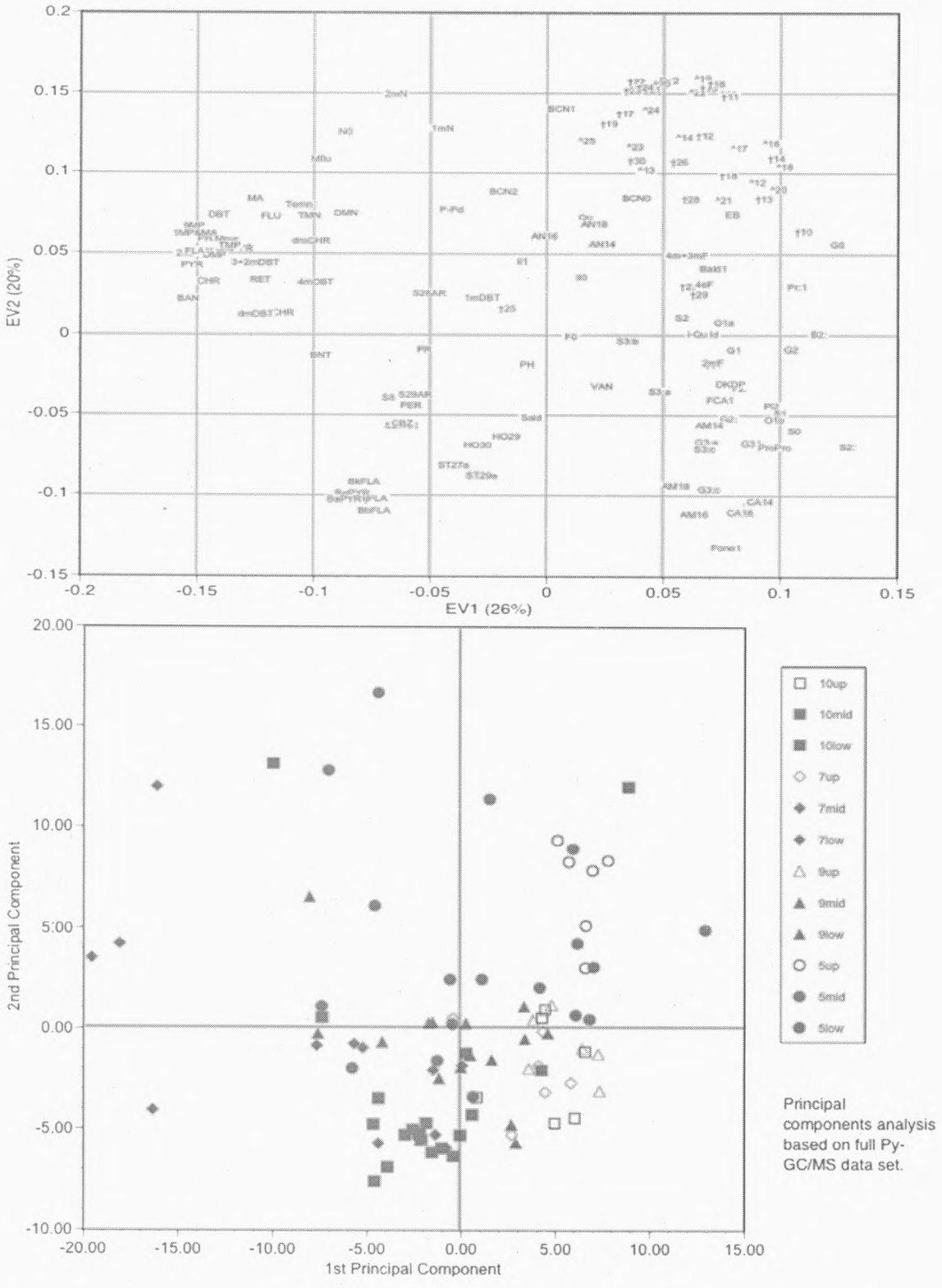

Figure 38. (A) Cross-plot of the first and second principal components generated from the full Py-GC/MS data set. (B) Cross-plot for the corresponding first and second eigenvectors.

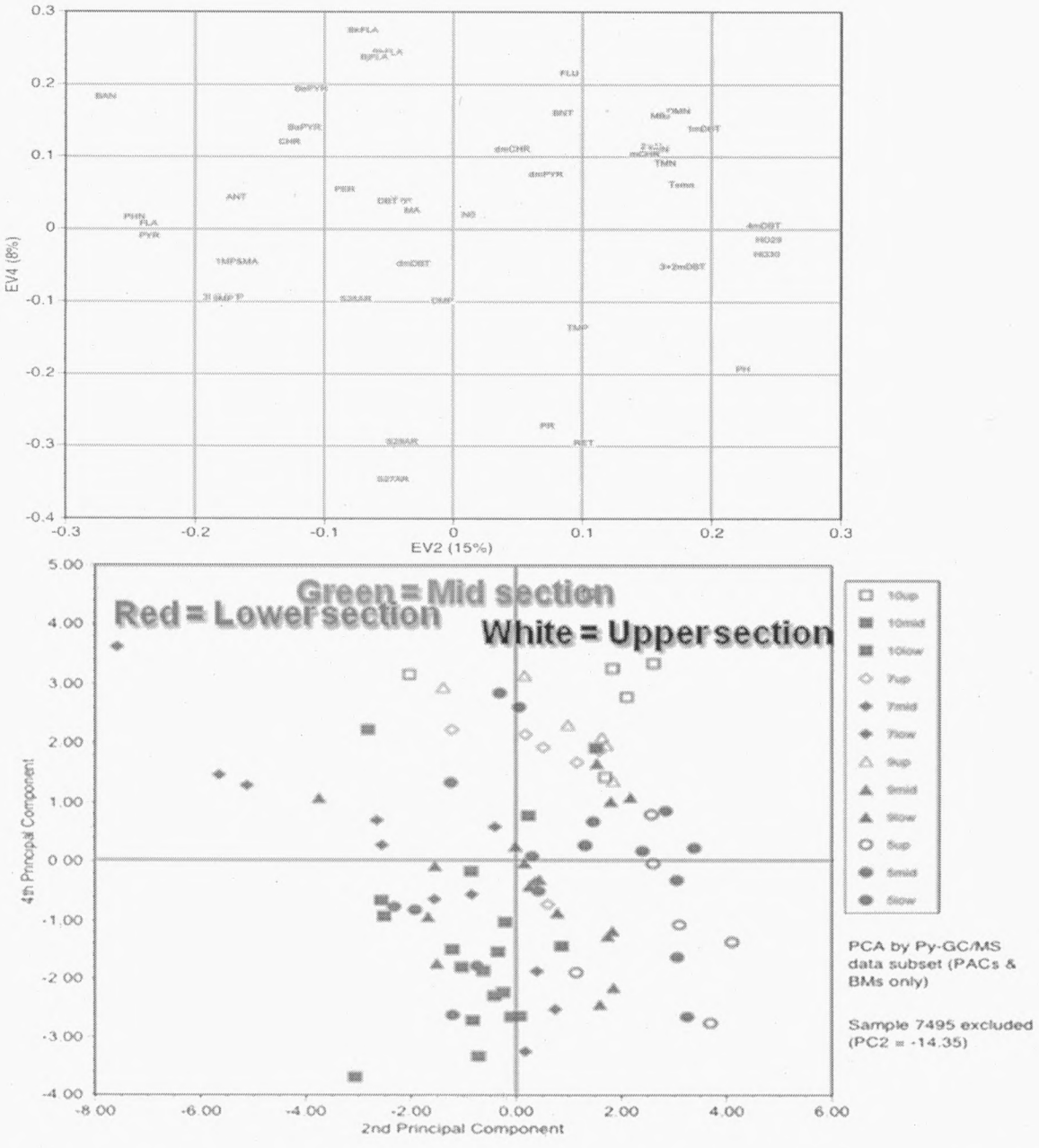

Figure 39. (A) Cross-plot of the second and fourth principal components generated from the Py-GC/MS data subset containing only polyaromatic compounds and petroleum biomarkers. (B) Cross-plot for the corresponding second and fourth eigenvectors.

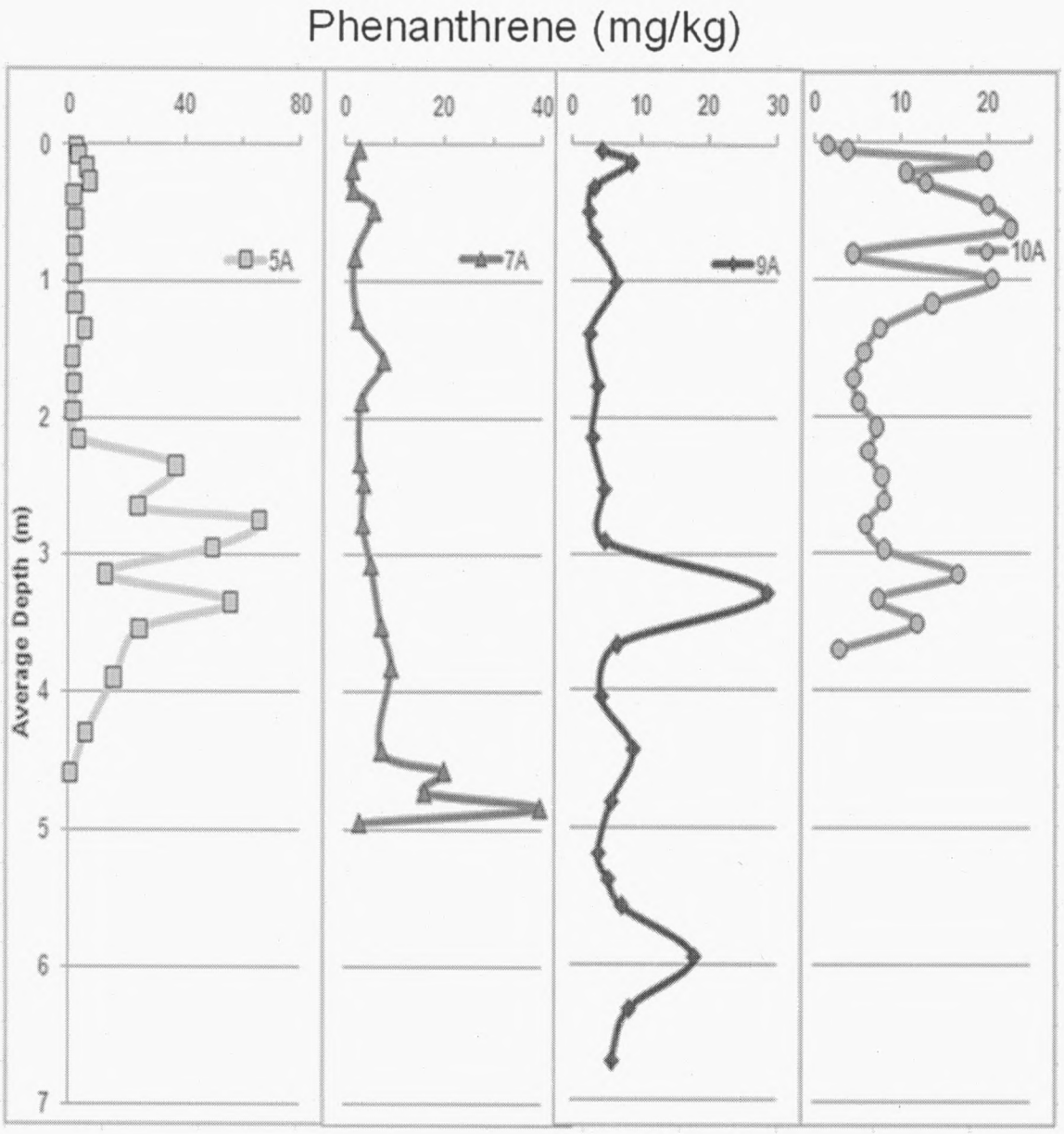

Figure 40. Plot of phenanthrene concentrations (mg/kg) determined by Py-GC/MS vs. average depth (m).

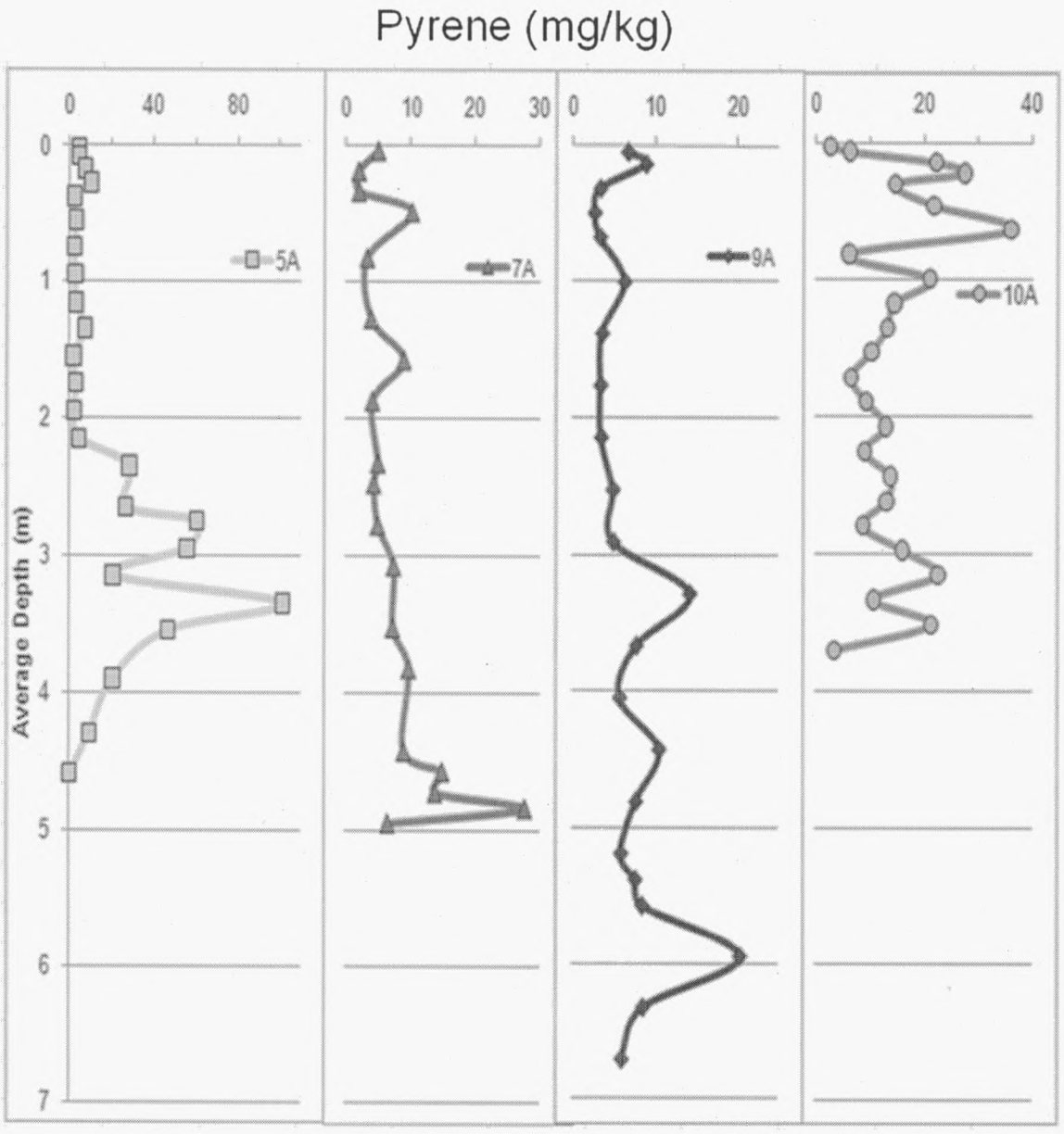

Figure 41. Plot of pyrene concentrations (mg/kg) determined by Py-GC/MS vs. average depth (m).

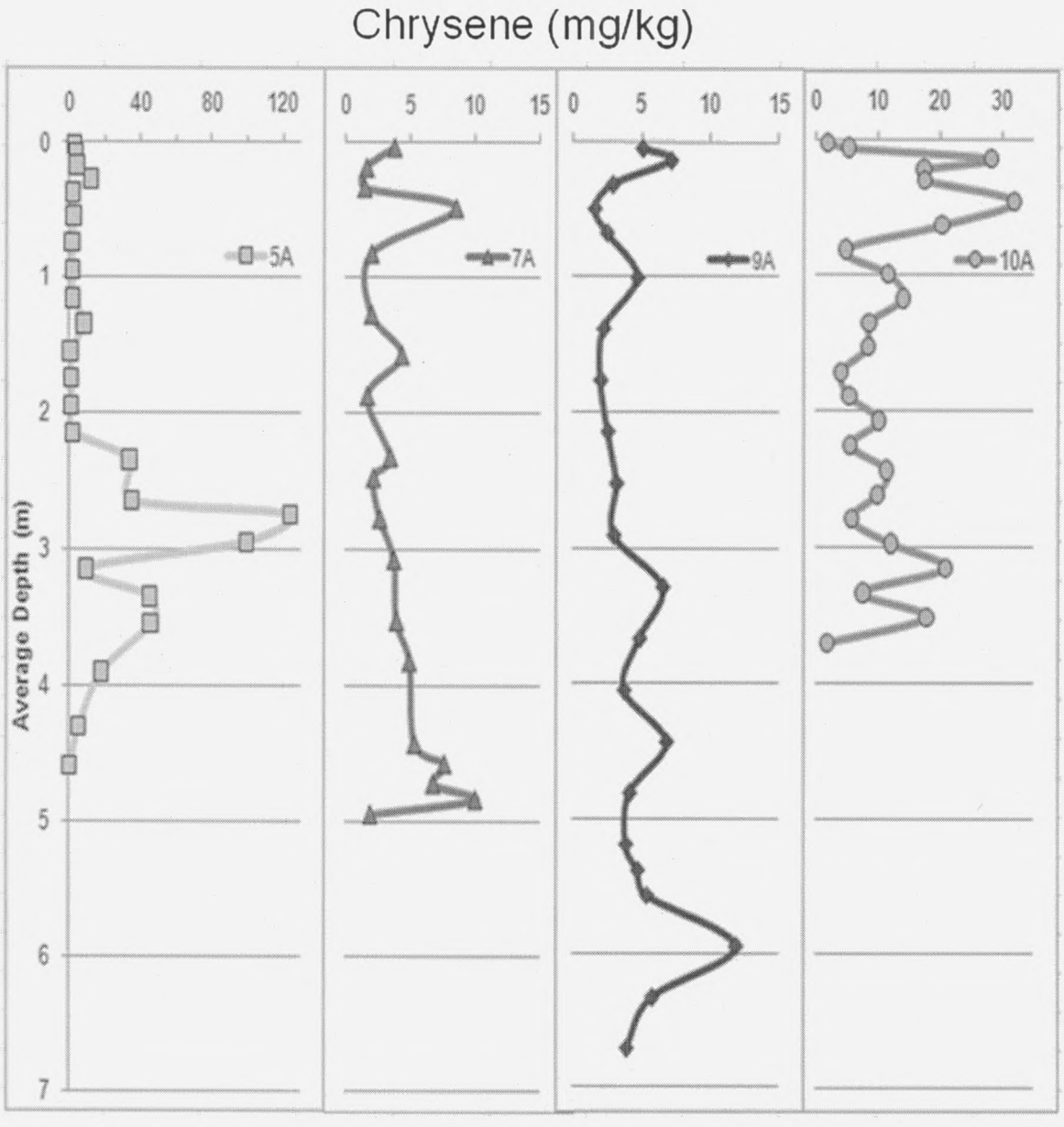

Figure 42. Plot of chrysene concentrations (mg/kg) determined by Py-GC/MS vs. average depth (m).

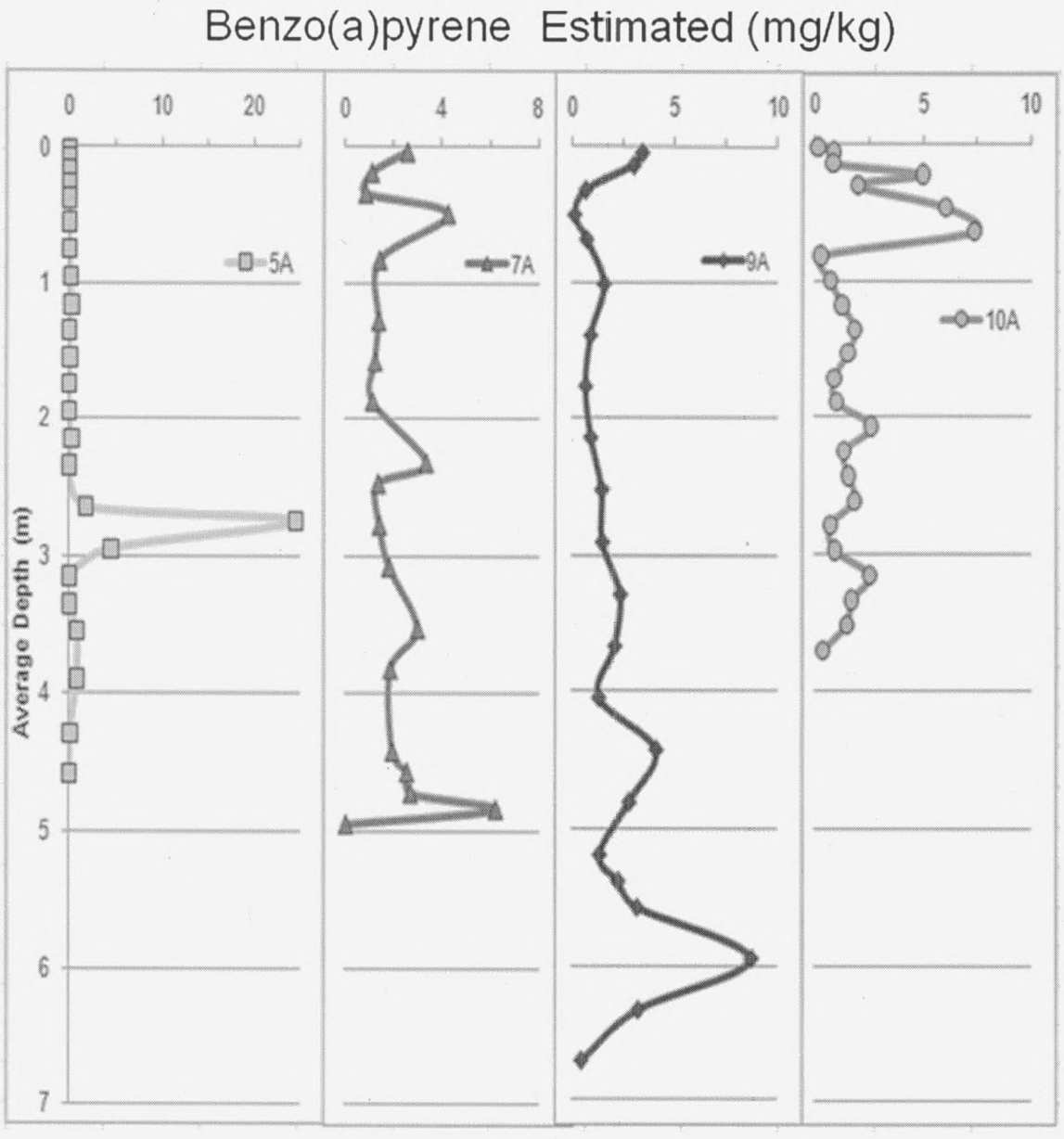

Figure 43. Plot of benzo[*a*]pyrene concentrations (mg/kg) determined by Py-GC/MS vs. average depth (m).

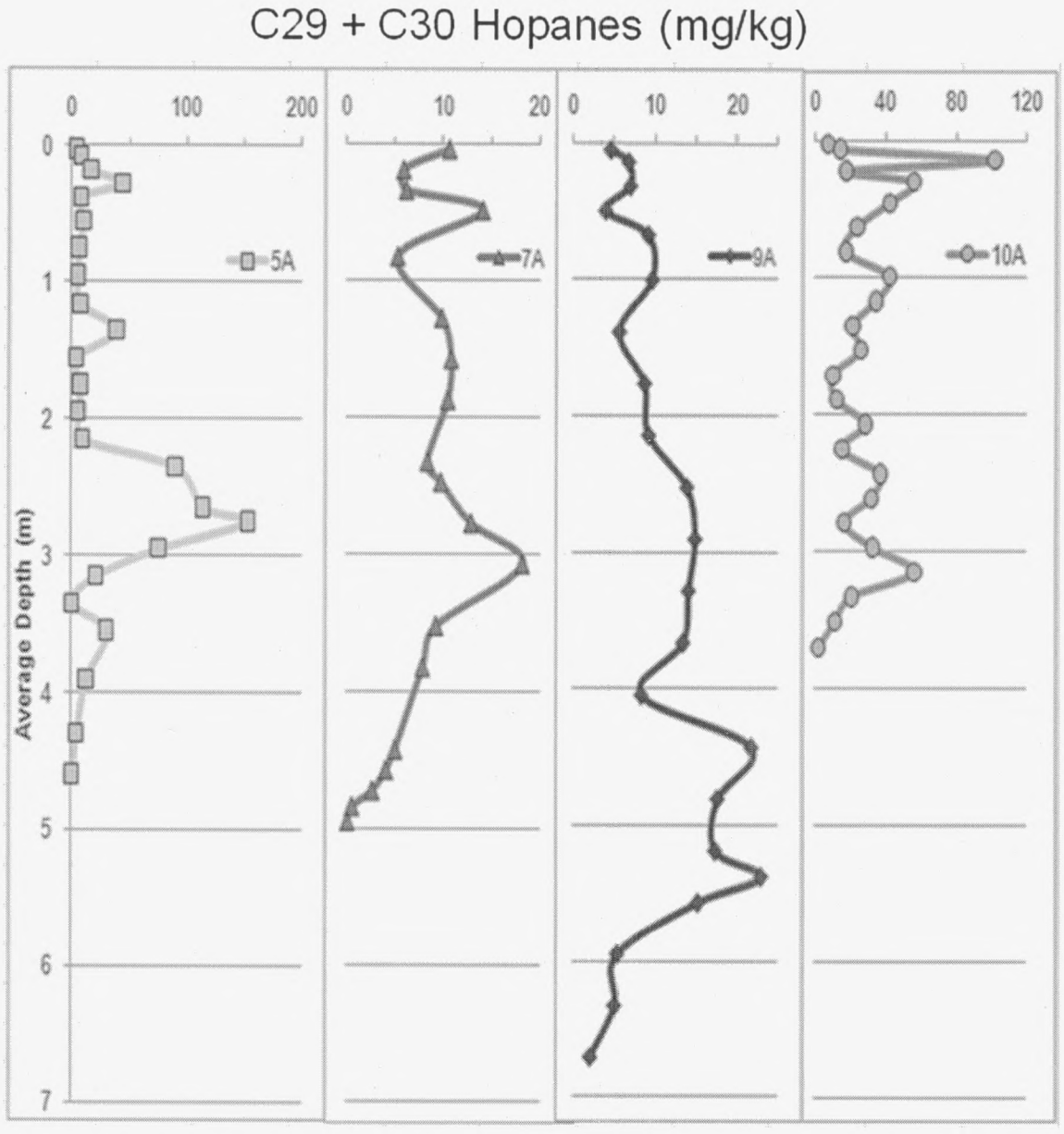

Figure 44. Plot of the summed concentration of C_{29} and C_{30} hopanes (mg/kg) determined by Py-GC/MS vs. average depth (m).

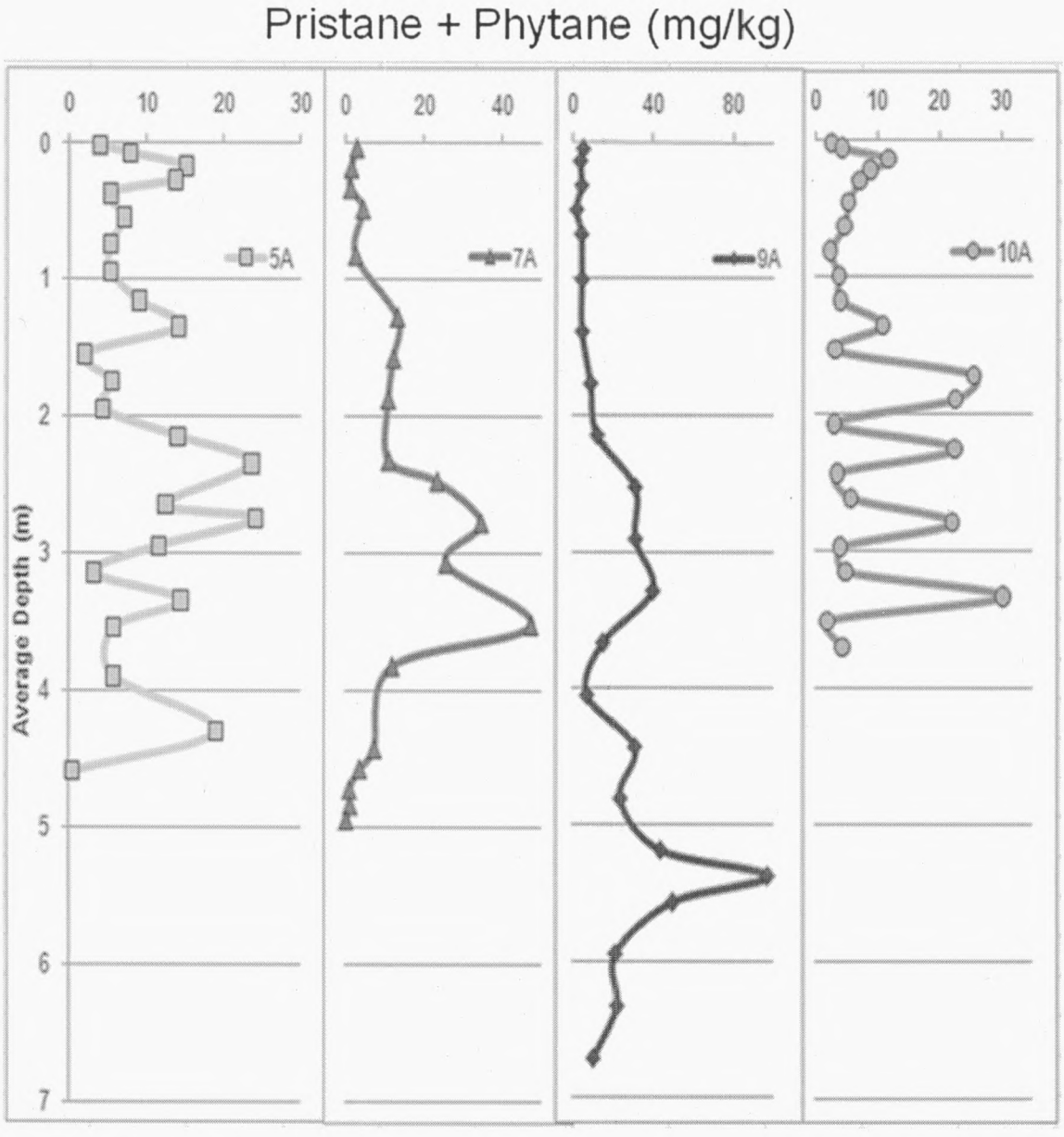

Figure 45. Plot of the summed concentrations of pristane and phytane determined by Py-GC/MS (mg/kg) vs. average depth (m).

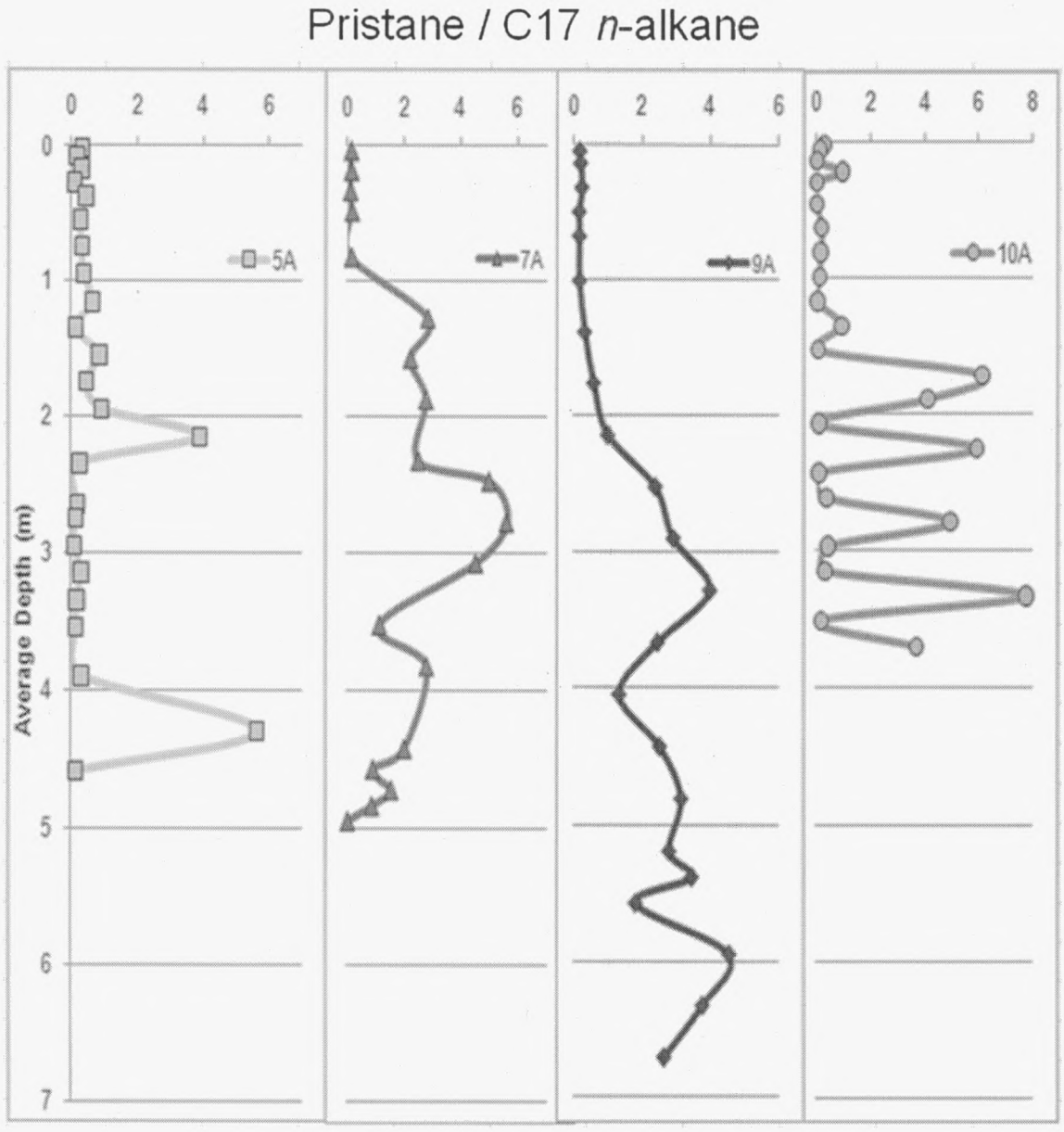

Figure 46. Plot of the pristane/ C_{17} *n*- alkane ratio vs. average depth (m).

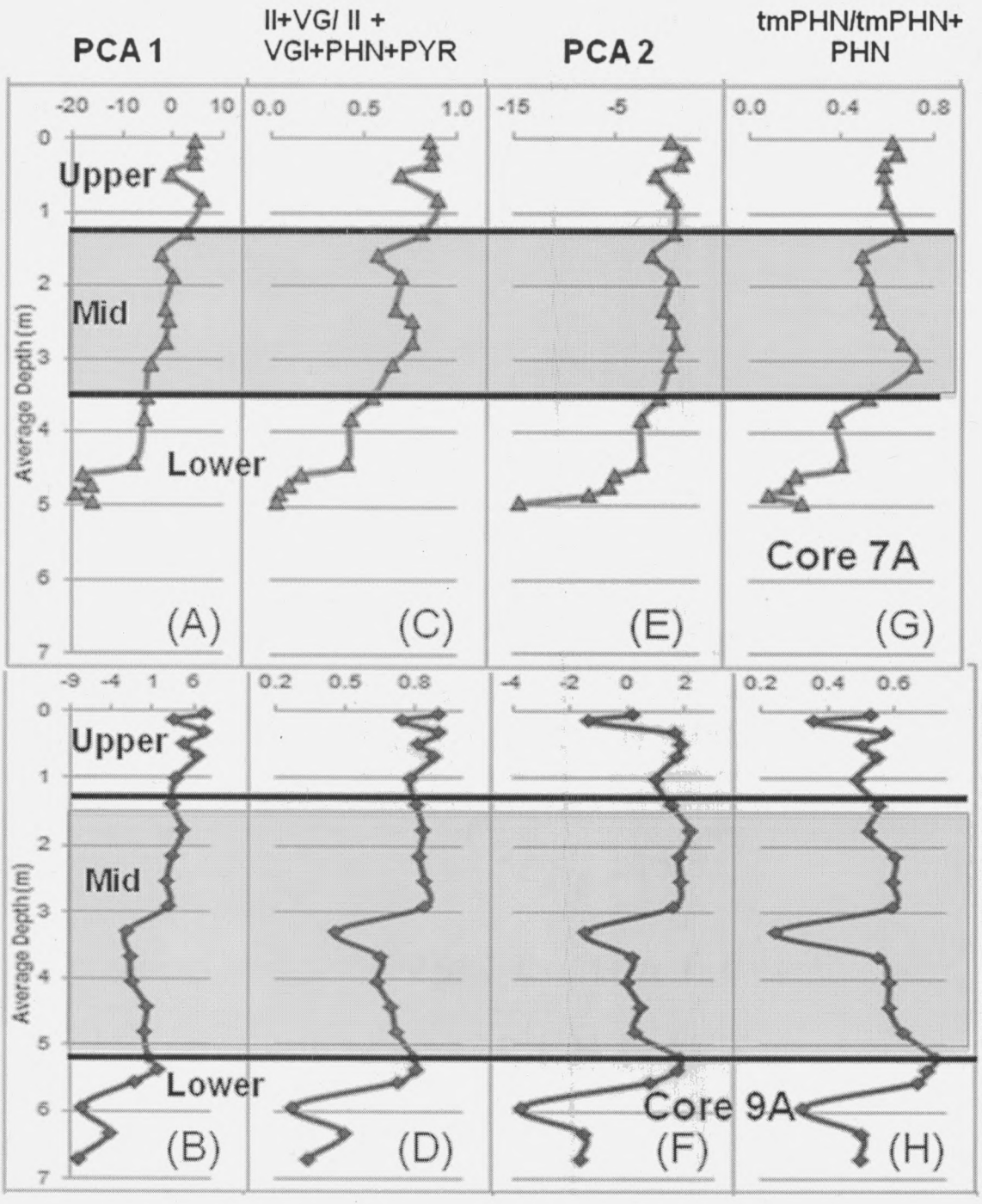

Figure 47. (A) Core 7A and (B) Core 9A are plots of the first principal component plotted against average sediment depth. (C) Core 7A and (D) Core 9A represent the ratio of indole plus vinyl guaiacol (biomarkers) plotted against average sediment depth. (E) Core 7A and (F) Core 9A represent the second principal component plotted against average sediment depth. (G) Core 7A and (H) Core 9A represent the ratio of trimethyl phenanthrene divided by the sum of trimethyl phenanthrene and phenanthrene. The general decreasing trend should be noted from surface downward, with an additional spike occurring at 3.15 m in core 9A. in all plots .

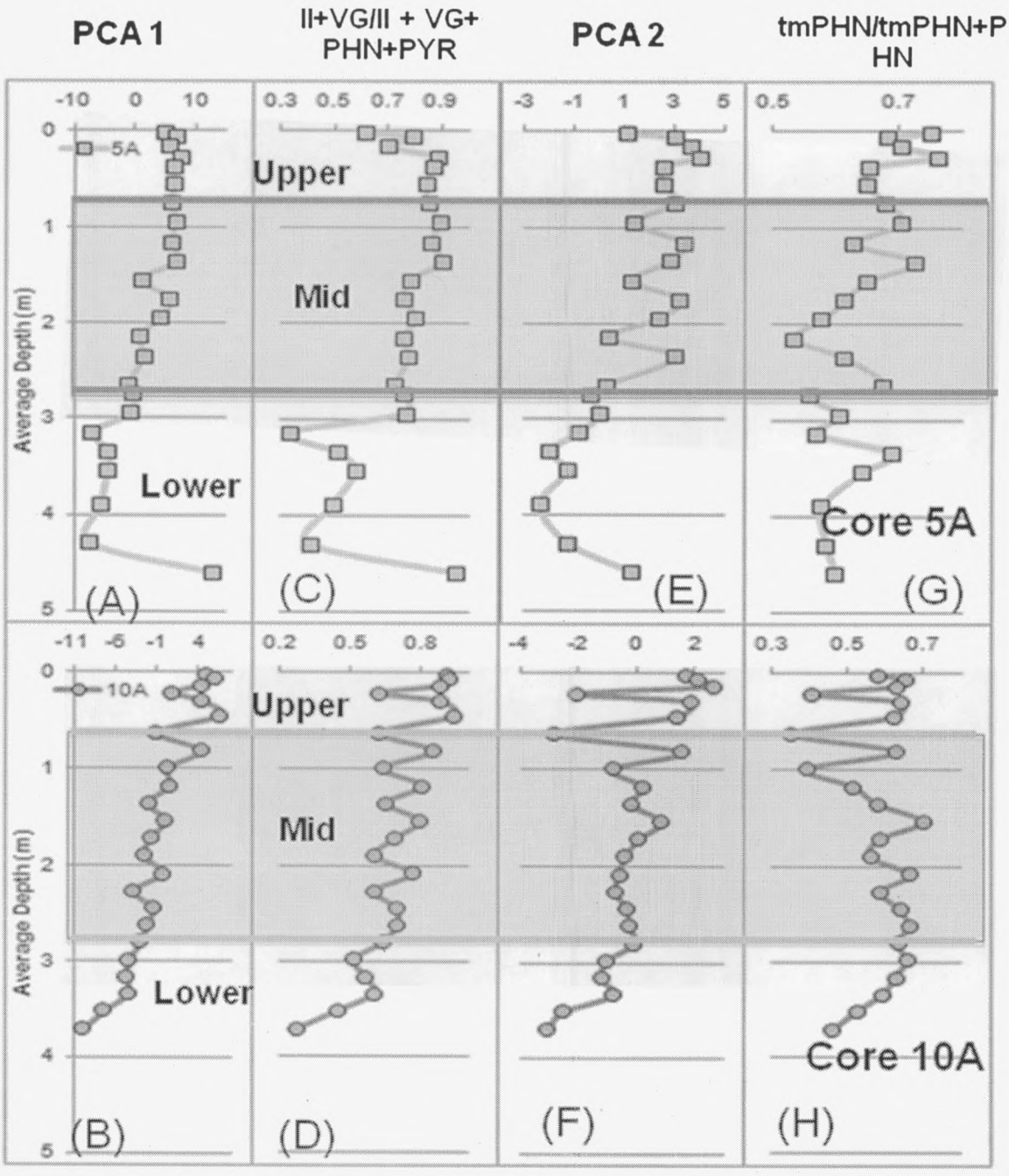

Figure 48. (A) Core 5A and (B) Core 10A are plots of the first principal component plotted against average sediment depth. (C) Core 5A and (D) Core 10A represent the ratio of indole plus vinyl guaiacol (biomarkers) plotted against average sediment depth. (E) Core 5A and (F) Core 10A represent the second principal component plotted against average sediment depth. (G) Core 5A and (H) Core 10A represent the ratio of trimethyl phenanthrene divided by the sum of trimethyl phenanthrene and phenanthrene. The general decreasing trend should be noted from surface downward, with an additional oscillating pattern occurring in the mid section of Core 5A in (E) and (G) and the upper portion of Core 10A (B, D, F, H).

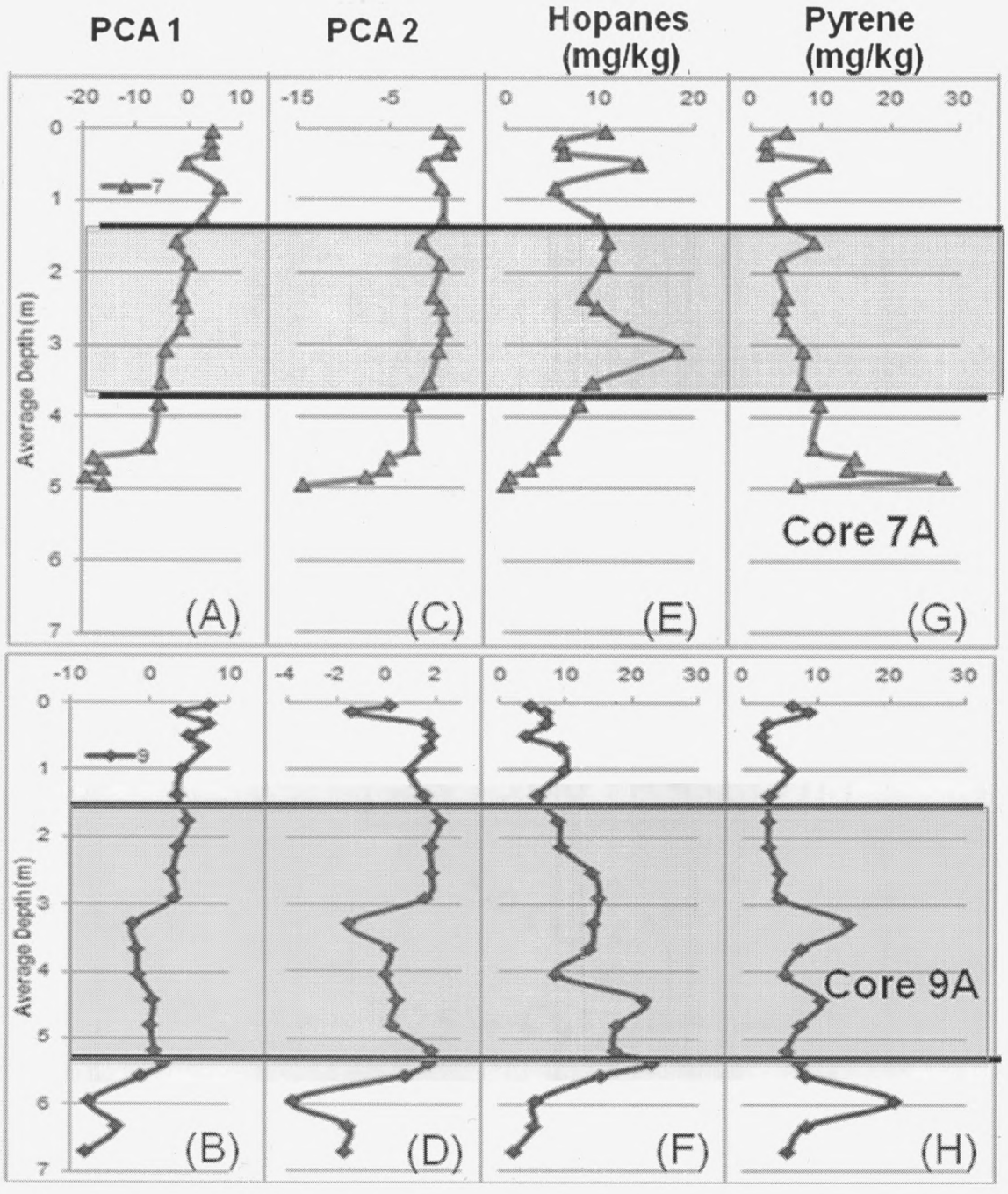

Figure 49. (A) Core 7A and (B) Core 9A are plots of the first principal component plotted against average sediment depth. (C) Core 7A and (D) Core 9A represent the second principal component plotted against average sediment depth. (E) Core 7A and (F) Core 9A represent the concentration of the sum of C_{29} and C_{30} hopanes plotted against average sample depth. (G) Core 7A and (H) Core 9A represent the concentration of pyrene plotted against average sample depth. The general negative correlation occurring between the principal components and pyrene concentration should be noted as well as the increase in hopane concentration occurring in a separate depth section from that of peak pyrene concentrations.

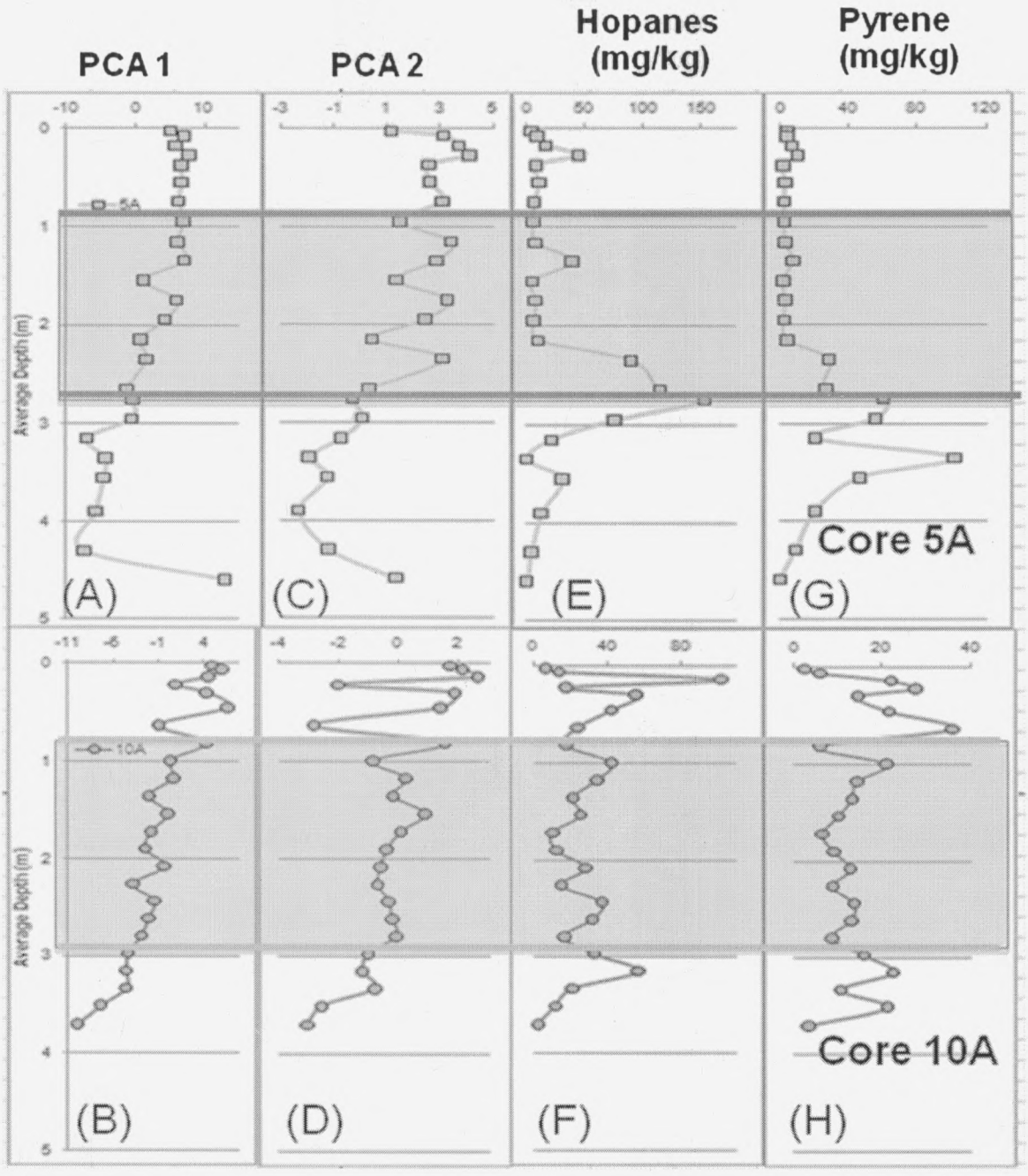

Figure 50. (A) Core 5A and (B) Core 10A are plots of the first principal component plotted against average sediment depth. (C) Core 5A and (D) Core 10A represent the second principal component plotted against average sediment depth. (E) Core 5A and (F) Core 10A represent the concentration of the sum of C_{29} and C_{30} hopanes plotted against average sample depth. (G) Core 5A and (H) Core 10A represent the concentration of pyrene plotted against average sample depth. The general negative correlation occurring between the principal components and pyrene concentration should be noted as well as the increase in hopane concentration occurring in similar depth sections from that of peak pyrene concentrations.

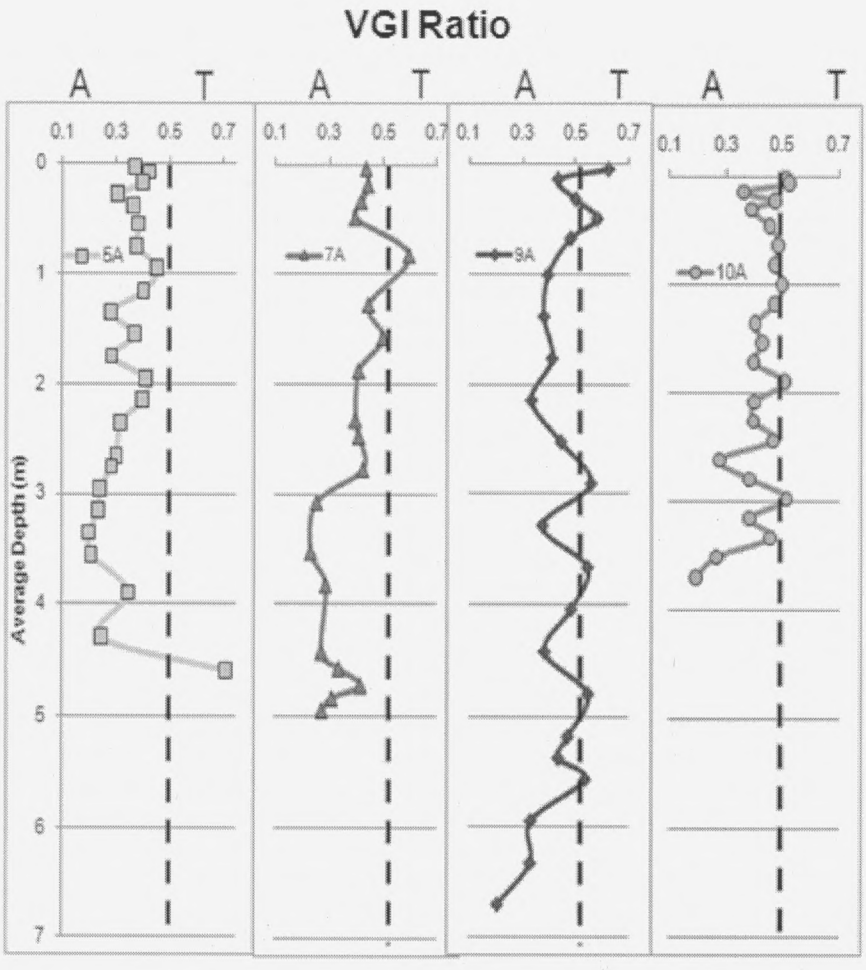

Figure 51. Plot of the VGI ratio vs. average depth (m). See text for ratio definition.

Passaic River Reaches	Dredging History (*Iannuzzi, et. al. 2002*)	
Kearny Point Reach: RM 0-1.2 Authorized Depth: 30 feet	1884 – Constructed to 10 Feet 1906 – Deepened to 12 Feet 1913 – Deepened to 16 Feet 1914 – Deepened to 20-22 Feet 1916 – Maintained at 16-17 Feet 1917 – Maintained at 21-22 Feet 1921 – Maintained at 20 Feet 1932 – Constructed to 30 Feet 1933 – Maintained at 30 Feet 1941 – Maintained at 30 Feet	1946 – Maintained at 30 Feet 1951 – Maintained at 30 Feet 1957 – Maintained at 30 Feet 1962 – Maintained at 30 Feet 1965 – Maintained at 30 Feet 1971 – Maintained at 30 Feet 1972 – Maintained at 30 Feet 1977 – Maintained at 30 Feet 1983 – Maintained at 30 Feet
Point No Point Reach: RM 1.2-2.5 Authorized Depth: 30 feet	1884 – Constructed to 10 Feet 1899 – Maintained at 10 Feet (from RM 1.9) 1906 – Deepened to 12 Feet 1913 – Deepened to 16 Feet 1914 – Deepened to 20-22 Feet (to RM 1.9) 1916 – Maintained at 16-17 Feet 1917 – Maintained to 21-22 Feet (to RM 2.0) 1921 – Maintained at 20 Feet 1922 – Maintained at 20 Feet (from RM 1.4) 1932 – Constructed to 30 Feet 1933 – Maintained at 30 Feet	1941 – Maintained at 30 Feet 1946 – Maintained at 30 Feet 1951 – Maintained at 30 Feet (to RM 1.3) 1957 – Maintained at 30 Feet (to RM 2.1) 1965 – Maintained at 30 Feet (to RM 1.8) 1971 – Maintained at 30 Feet (to RM 1.5) 1972 – Maintained at 30 Feet (to RM 1.8) 1983 – Maintained at 30 Feet (to RM 1.9)
Harrison Reach: RM 2.5-4.6 Authorized Depth: 30 feet to RM 2.6 Authorized Depth: 20 feet From RM 2.6	1884 – Constructed to 10 Feet 1899 – Maintained at 10 Feet 1906 – Deepened to 12 Feet 1913 – Deepened to 16 Feet 1916 – Maintained at 16-17 Feet 1916 – Deepened to 20-21 Feet (RM 2.6-4.5) 1921 – Maintained at 20 Feet 1922 – Maintained at 20 Feet (to RM 4.2) 1923 – Maintained at 20 Feet (RM 4.2-4.6) 1932 – Constructed to 30 Feet (to RM 2.6) 1937 – Maintained to 20 Feet (starting at RM 2.6)	

Table 1. Dredging history from 1884 to present for the Passaic River as recorded by the USACE 2008 and also presented by Iannuzzi et al. 2002.

Passaic River Reaches	Dredging History (*Iannuzzi, et. al. 2002*)
Newark Reach: RM 4.6-6.1 Authorized Depth: 20 feet (Constructed Depth: 16 feet)	1884 – Constructed to 10 Feet (to RM 5.4) 1899 – Maintained at 10 Feet (to RM 5.4) 1906 – Deepened to 12 Feet 1913 – Deepened to 16 Feet (to RM 5.8) 1916 – Maintained at 16-17 Feet 1919 – Maintained at 16 Feet (starting at RM 4.6) 1933 – Maintained at 10 Feet (from RM 6.0) 1950 – Maintained at 16 Feet (from RM 5.5)
Kearny Reach: RM 6.1-7.1 Authorized Depth: 20 feet (Constructed Depth: 16 feet)	1883 – Constructed to 6 Feet 1906 – Deepened to 12 Feet (to RM 6.5) 1906 – Deepened to 12 Feet (from RM 6.5) 1913 – Deepened to 16 Feet (to RM 5.8) 1916 – Maintained/Deepened at 16-17 Feet 1919 – Maintained at 16 Feet (to RM 6.4) 1933 – Maintained at 16 Feet (to RM 6.3) 1950 – Maintained at 16 Feet (to RM 7.0)
Arlington Reach: RM 7.1-8.1 Authorized Depth: 16 feet	1883 – Constructed to 6 Feet 1906 – Deepened to 10 Feet (to RM 8.0) 1915 – Constructed to 6-7 Feet (from RM 8.0) 1916 – Deepened to 16-17 Feet (to RM 8.0) 1927 – Maintained to 6 Feet (from RM 8.0) 1929 – Maintained to 6 Feet (from RM 8.0) 1930 – Constructed to 10 Feet (from RM 8.0)
Belleville Reach: RM 8.1-8.3 (Partial Reach) Authorized Depth: 16 feet	1915 – Constructed to 6-7 Feet 1927 – Maintained to 6 Feet 1929 – Maintained to 6 Feet 1930 – Constructed to 10 Feet 1931 – Maintained to 10 Feet 1932 – Maintained to 10 Feet
Above Erie/Montclair & Greenwood Lake Railroad Bridge: RM 8.3 – 15.4 Authorized Depth: 10 feet	1915 – Constructed to 6-7 Feet (to RM 13.2) 1927 – Maintained to 6 Feet (to RM 9.0) 1929 – Maintained to 6 Feet (to RM 9.0) 1930 – Constructed to 10 Feet (to RM 9.0) 1931 – Maintained to 10 Feet (to RM 9.0) 1931 – Constructed to 10 Feet (RM 9.0 to 15.4) 1932 – Maintained to 10 Feet (to RM 15.4) 1950 – Maintained to 10 Feet (RM 14.3-15.4) 1976 – Maintained to 10 Feet (RM 9.0-10.2)

Table 1(continued). Dredging history from 1884 to present for the Passaic River as recorded by the USACE 2008 and also presented by Iannuzzi et al. 2002.

CoreNumber	5A - primary	7A - primary	9A - primary	10A Primary
RiverMile	1.05	1.4	2.2	2.6
Location_ID	G0000002	G0000004	G0000005	G0000006
Longitude	-74.1190867	-74.1176732	-74.1193834	-74.1273059
Latitude	40.72549996	40.73018836	40.74040062	40.74216963
Core_Id	54	56	57	58
Coring_Method	Vibracore	Vibracore	Vibracore	Vibracore
Coring_Datetime	16-Sep-05	20-Sep-05	21-Sep-05	22-Sep-05
Core_Length (cm)	609.6	579.1	680	533.4
TubeDiameter (cm)	8.73125	8.73125	8.73125	8.73125
PercentRecField	69.0	66.7	76.9	94.6
SliceLength (cm)	13.9	13.2	15.5	12.1
NumSlices	44	44	44	44
BulkDensity (g/cm3)	1.21	1.27	1.45	1.27

Table 2. Core information.

Core	Sample ID1	Sample ID2	Sample ID3	Upper Depth (cm)	Lower Depth (cm)	Average Depth (cm)
5A	5A_S01	5003	SA0000003	0	5	3
5A	5A_S02	5008	SA0000009	5	10	8
5A	5A_S04	5018	SA0000018	15	20	18
5A	5A_S06	5028	SA0000027	25	30	28
5A	5A_S08	5038	SA0000038	35	40	38
5A	5A_S10	5055	SA0000047	50	60	55
5A	5A_S12	5075	SA0000059	70	80	75
5A	5A_S14	5095	SA0000087	90	100	95
5A	5A_S16	5116	SA0000078	112	120	116
5A	5A_S18	5135	SA0000079	130	140	135
5A	5A_S20B	5155	SA0000106	150	160	155
5A	5A_S22	5175	SA0000112	170	180	175
5A	5A_S24	5195	SA0000127	190	200	195
5A	5A_S26	5215	SA0000141	210	220	215
5A	5A_S28	5235	SA0000136	230	240	235
5A	5A_S30	5265	SA0000156	260	270	265
5A	5A_S32	5275	SA0000169	270	280	275
5A	5A_S34	5295	SA0000179	290	300	295
5A	5A_S36	5315	SA0000194	310	320	315
5A	5A_S38	5335	SA0000201	330	340	335
5A	5A_S40	5355	SA0000221	350	360	355
5A	5A_S42	5390	SA0000227	380	400	390
5A	5A_S44	5430	SA0000235	420	440	430
5A	5A_S46	5460	SA0000244	449.5	469.5	460

Table 3. Core 5A information on sample slices. Sample ID1 was used for pyrolysis analysis, sample ID2 represents the code used for the samples in the PAH ratio plots, and sample ID3 corresponds to the identification code used by Malcolm Pirnie, Inc.

Core	Sample ID1	Sample ID2	Sample ID3	Upper Depth (cm)	Lower Depth (cm)	Average Depth (cm)
7A	7A_S01	7004	SA000259	0	7.5	4
7A	7A_S03	7019	SA000268	15	22.5	19
7A	7A_S05	7034	SA000297	30	37.5	34
7A	7A_S07	7049	SA000283	45	52.5	49
7A	7A_S10	7083	SA000302	75	90	83
7A	7A_S13	7128	SA000316	120	135	128
7A	7A_S15	7158	SA000327	150	165	158
7A	7A_S17	7188	SA000339	180	195	188
7A	7A_S20	7233	SA000349	225	240	233
7A	7A_S21	7248	SA000364	240	255	248
7A	7A_S23	7278	SA000371	270	285	278
7A	7A_S25	7308	SA000403	300	315	308
7A	7A_S28	7353	SA000409	345	360	353
7A	7A_S30	7383	SA000429	375	390	383
7A	7A_S34	7443	SA000464	435	450	443
7A	7A_S35B	7458	SA000470	450	465	458
7A	7A_S36	7473	SA000446	465	480	473
7A	7A_S37	7484	SA000474	480	488	484
7A	7A_S38	7495	SA000454	488	502	495

Table 4. Core 7A information on sample slices. Sample ID1 was used for pyrolysis analysis, sample ID2 represents the code used for the samples in the PAH ratio plots, and sample ID3 corresponds to the identification code used by Malcolm Pirnie, Inc.

Core	Sample ID1	Sample ID2	Sample ID3	Upper Depth (cm)	Lower Depth (cm)	Average Depth (cm)
9A	9A_S01	9005	SA0000477	0	9	5
9A	9A_S02	9014	SA0000485	9	18	14
9A	9A_S04	9032	SA0000498	27	36	32
9A	9A_S06	9050	SA0000489	45	54	50
9A	9A_S08	9068	SA0000516	63	72	68
9A	9A_S10	9101	SA0000532	91	110	101
9A	9A_S12	9139	SA0000546	129	148	139
9A	9A_S14	9177	SA0000557	167	186	177
9A	9A_S16	9215	SA0000565	205	224	215
9A	9A_S18B	9253	SA0000577	243	262	253
9A	9A_S20B	9291	SA0000583	281	300	291
9A	9A_S22B	9329	SA0000607	319	338	329
9A	9A_S24	9367	SA0000614	357	376	367
9A	9A_S26	9405	SA0000636	395	414	405
9A	9A_S28	9443	SA0000641	433	452	443
9A	9A_S30	9481	SA0000713	471	490	481
9A	9A_S32	9519	SA0000654	509	528	519
9A	9A_S33		SA0000673	528	547	538
9A	9A_S34	9557	SA0000677	547	566	557
9A	9A_S36	9595	SA0000681	585	604	595
9A	9A_S38	9633	SA0000700	623	642	633
9A	9A_S40	9671	SA0000710	661	680	671

Table 5. Core 9A information on sample slices. Sample ID1 was used for pyrolysis analysis, sample ID2 represents the code used for the samples in the PAH ratio plots, and sample ID3 corresponds to the identification code used by Malcolm Pirnie, Inc.

Core	Sample ID1	Sample ID2	Sample ID3	Upper Depth (cm)	Lower Depth (cm)	Average Depth (cm)
10A	10A_S01	10002	SA000763	0	4	2
10A	10A_S02	10006	SA000758	4	8	6
10A	10A_S04	10014	SA000724	12	16	14
10A	10A_S06	10022	SA000752	20	24	22
10A	10A_S08	10030	SA000736	28	32	30
10A	10A_S10	10046	SA000769	41	50	46
10A	10A_S12	10064	SA000742	59	68	64
10A	10A_S14B	10082	SA000755	77	86	82
10A	10A_S16	10100	SA000781	95	104	100
10A	10A_S18	10118	SA000790	113	122	118
10A	10A_S20	10136	SA000799	131	140	136
10A	10A_S22	10154	SA000807	149	158	154
10A	10A_S24	10172	SA000859	167	176	172
10A	10A_S26	10190	SA000821	185	194	190
10A	10A_S28	10208	SA000833	203	212	208
10A	10A_S30	10226	SA000860	221	230	226
10A	10A_S32	10244	SA000845	239	248	244
10A	10A_S34	10262	SA000881	257	266	262
10A	10A_S36	10280	SA000868	275	284	280
10A	10A_S38	10298	SA000890	293	302	298
10A	10A_S40	10316	SA000898	311	320	316
10A	10A_S42	10334	SA000920	329	338	334
10A	10A_S44	10352	SA000907	347	356	352
10A	10A_S46	10371	SA000933	365	376	371

Table 6. Core 10A information on sample slices. Sample ID1 was used for pyrolysis analysis, sample ID2 represents the code used for the samples in the PAH ratio plots, and sample ID3 corresponds to the identification code used by Malcolm Pirnie, Inc.

Compound	Code	mass	*RT*
HYDROCARBONS			
normal & isoprenoid alkenes			
C8 n-alk-1-ene	^8	55	*3.83*
C9 n-alk-1-ene	^9	69	*6.75*
C10 n-alk-1-ene	^10	69	*10.30*
C11 n-alk-1-ene	^11	69	*13.68*
C12 n-alk-1-ene	^12	69	*16.79*
C13 n-alk-1-ene	^13	69	*19.67*
C14 n-alk-1-ene	^14	69	*22.35*
C15 n-alk-1-ene	^15	69	*24.87*
C16 n-alk-1-ene	^16	69	*27.25*
C17 n-alk-1-ene	^17	69	*29.53*
C18 n-alk-1-ene	^18	69	*31.67*
C19 n-alk-1-ene	^19	69	*33.71*
C20 n-alk-1-ene	^20	69	*35.65*
C21 n-alk-1-ene	^21	69	*37.51*
C22 n-alk-1-ene	^22	69	*39.29*
C23 n-alk-1-ene	^23	69	*40.98*
C24 n-alk-1-ene	^24	69	*42.63*
C25 n-alk-1-ene	^25	69	*44.20*
C26 n-alk-1-ene	^26	69	*45.72*
C27 n-alk-1-ene	^27	69	*47.03*
C28 n-alk-1-ene	^28	69	*48.59*
C29 n-alk-1-ene	^29	69	*49.94*
prist-1-ene	Pr:1	69	*30.43*
prist-2-ene	Pr:2	69	*30.65*
normal & isoprenoid alkanes			
C8 n-alkane	†8	55	*3.83*
C9 n-alkane	†9	71	*7.20*
C10 n-alkane	†10	71	*10.71*
C11 n-alkane	†11	71	*14.05*
C12 n-alkane	†12	71	*17.13*
C13 n-alkane	†13	71	*19.98*
C14 n-alkane	†14	71	*22.63*
C15 n-alkane	†15	71	*25.14*
C16 n-alkane	†16	71	*27.50*

C17 n-alkane	†17	71	*29.73*
C18 n-alkane	†18	71	*31.86*
C19 n-alkane	†19	71	*33.88*
C20 n-alkane	†20	71	*35.81*
C21 n-alkane	†21	71	*37.66*
C22 n-alkane	†22	71	*39.42*
C23 n-alkane	†23	71	*41.12*
C24 n-alkane	†24	71	*42.75*
C25 n-alkane	†25	71	*44.31*
C26 n-alkane	†26	71	*45.83*
C27 n-alkane	†27	71	*47.28*
C28 n-alkane	†28	71	*48.68*
C29 n-alkane	†29	71	*50.04*
C30 n-alkane	†30	71	*51.35*
C31 n-alkane	†31	71	*52.62*
C32 n-alkane	†32	71	*53.86*
C33 n-alkane	†33	71	*55.10*
nor-pristane	NP	71	*28.66*
pristane	PR	71	*29.94*
phytane	PH	71	*32.13*
monoaromatic hydrocarbons			
simple benzenes			
benzene	B0	78	*<3*
ethylbenzene	EB	91	*5.36*
styrene	B2:	104	*6.36*
n-propylbenzene	B-n3	91	*8.48*
1-ethyl-3-methylbenzene	B-1E3M	105	*8.73*
1-ethyl-4-methylbenzene	B-1E4M	105	*8.80*
1,3,5-trimethylbenzene	B-135TrM	105	*9.03*
1-ethyl-2-methylbenzene	B-1E2M	105	*9.33*
1,2,4-trimethylbenzene	B-124TrM	105	*9.85*
1,2,3-trimethylbenzene	B-123TrM	105	*10.74*
indenes			
indene	I0	116	*11.19*
methylindene isomer	I1a	130	*14.68*
methylindene isomer	I1b	130	*14.80*
methylindene isomer	I1c	130	*14.84*
dimethylindene isomer	I2a	144	*17.90*
dimethylindene isomer	I2b	144	*18.02*

dimethylindene isomer	I2c	144	*18.16*
naphthalenes			
naphthalene	N0	128	*15.60*
methylnaphthalenes	N1		
2-methylnaphthalene	2mN	142	*18.88*
1-methylnaphthalene	1mN	142	*19.29*
C2-alkylnaphthalenes	N2		
ethylnaphthalene	eN	156	*21.59*
2,5-dimethylnaphthalene	25DMN	156	*21.87*
2,7-dimethylnaphthalene	27DMN	156	*21.93*
1,3-dimethylnaphthalene	13DMN	156	*22.25*
1,6- & 1,7-dimethylnaphthalenes	16+17DMN	156	*22.33*
1,4- & 1,5- & 2,3-dimethylnaphthalenes	14++DMN	156	*22.74*
1,2-dimethylnaphthalene	12DMN	156	*23.07*
C3-alkylnaphthalenes	N3		
methylethylnaphthalene	meNa	170	*24.46*
methylethylnaphthalene	meNb	170	*24.84*
1,3,7-trimethylnaphthalene	137TMN	170	*24.99*
1,3,6-trimethylnaphthalene	136TMN	170	*25.10*
1,4,6- & 1,3,5-trimethylnaphthalenes	146+135TMN	170	*25.45*
2,3,6-trimethylnaphthalene	236TMN	170	*25.55*
1,2,7-trimethylnaphthalene	127TMN	170	*25.80*
1,6,7- & 1,2,6-trimethylnaphthalenes	167+126TMN	170	*25.87*
1,2,5-trimethylnaphthalene	125TMN	170	*26.35*
C4-alkylnaphthalenes	N4		
1,3,5,7-tetramethylnaphthalene	1357TeMN	184	*27.88*
1,3,6,7-tetramethylnaphthalene	1367TeMN	184	*28.38*
1,2,4,7-tetramethylnaphthalene	1247TeMN	184	*28.68*
1,2,5,7-tetramethylnaphthalene	1257TeMN	184	*28.75*
2,3,6,7-tetramethylnaphthalene	2367TeMN	184	*29.11*
1,2,6,7-tetramethylnaphthalene	1267TeMN	184	*29.18*
1,2,3,6-tetramethylnaphthalene	1236TeMN	184	*29.30*
1,2,5,6-tetramethylnaphthalene	1256TeMN	184	*29.63*
fluorenes			
fluorene	FLU	166	*26.08*
2- & 3-methylfluorenes	2+3-mFLU	165	*28.73*
1-methylfluorene	1-mFLU	165	*28.85*
4-methylfluorene	4-mFLU	165	*29.08*

miscelaneous aromatic hydrocarbons			
acenaphthylene	ACY	152	*22.78*
acenaphthene	ACE	154	*23.70*
biphenyl	BB	154	*22.40*
2-methylbiphenyl	2mBB	168	*23.90*
3- & 4-methylbiphenyls	3+4mBB	168	*24.11*
phenylnaphthalene	BN	204	*31.99*
phenanthrenes			
phenanthrene	PHN	178	*30.31*
anthracene	ANT	178	*30.53*
methylphenanthrene group	PHN1		
3-methylphenanthrene	3MP	192	*32.74*
2-methylphenanthrene	2MP	192	*32.83*
methylanthracene	MA	192	*33.02*
9-methylphenanthrene	9MP	192	*33.18*
1-methylphenanthrene & methylanthracene	1MP&MA	192	*33.27*
C2-alkylphenanthrenes	PHN2		
3,6-dimethylphenanthrene	36DMP	206	*34.99*
2,6-dimethylphenanthrene	26DMP	206	*35.11*
2,7-dimethylphenanthrene	27DMP	206	*35.15*
1,3- & 2,10- & 3,9- & 3,10-dimethylphenanthrenes	13++DMP	206	*35.43*
1,6- & 2,9-dimethylphenanthrenes	16+29DMP	206	*35.54*
1,7-dimethylphenanthrene	17DMP	206	*35.62*
2,3-dimethylphenanthrene	23DMP	206	*35.78*
1,9-dimethylphenanthrene	19DMP	206	*35.84*
1,8-dimethylphenanthrene	18DMP	206	*36.07*
1,2-dimethylphenanthrene	12DMP	206	*36.33*
C3-alkylphenanthrenes	PHN3		
trimethylphenanthrene isomer	TMP1	220	*37.59*
trimethylphenanthrene isomer	TMP2	220	*37.70*
trimethylphenanthrene isomer	TMP3	220	*37.90*
trimethylphenanthrene isomer	TMP4	220	*37.98*
trimethylphenanthrene isomer	TMP5	220	*38.10*
trimethylphenanthrene isomer	TMP6	220	*38.23*
trimethylphenanthrene isomer	TMP7	220	*38.35*
trimethylphenanthrene isomer	TMP8	220	*38.43*
trimethylphenanthrene isomer	TMP9	220	*38.55*
trimethylphenanthrene isomer	TMP10	220	*38.82*
trimethylphenanthrene isomer	TMP11	220	*39.00*
C4-alkylphenanthrene	PHN4		

retene (1-methyl-7-(1-methylethyl)-phenanthrene)	RET	219	*38.82*
pyrene group			
fluoranthene	FLA	202	*35.73*
pyrene	PYR	202	*36.64*
methylpyrene isomers	PYR1		
2-methylfluoranthene	2mFLA	216	*38.10*
benzo[a]fluorene	BaFLU	216	*38.49*
benzo[b] & [c]fluorenes	Bb+cFLU	216	*38.82*
2-methylpyrene	2mPYR	216	*38.91*
4-methylpyrene	4mPYR	216	*39.30*
1-methylpyrene	1mPYR	216	*39.42*
dimethylpyrene isomers	PYR2		
dimethylpyrene isomer	dmPYR1	230	*40.18*
dimethylpyrene isomer	dmPYR2	230	*40.50*
dimethylpyrene isomer	dmPYR3	230	*40.60*
dimethylpyrene isomer	dmPYR4	230	*40.92*
dimethylpyrene isomer	dmPYR5	230	*21.23*
dimethylpyrene isomer	dmPYR6	230	*41.35*
dimethylpyrene isomer	dmPYR7	230	*41.43*
dimethylpyrene isomer	dmPYR8	230	*41.70*
dimethylpyrene isomer	dmPYR9	230	*41.83*
chrysene group			
benzo[a]anthracene	BAN	228	*42.30*
chrysene	CHR	228	*42.43*
methylchrysene isomers	CHR1		
3-methylchrysene	3mCHR	242	*42.34*
2-methylchrysene	2mCHR	242	*44.44*
6-methylchrysene	6mCHR	242	*44.66*
4-methylchrysene	4mCHR	242	*44.74*
1-methylchrysene	1mCHR	242	*44.85*
dimethylchrysene isomers	CHR2		
dimethylchrysene isomer	dmCHR1	256	*46.15*
dimethylchrysene isomer	dmCHR2	256	*46.25*
dimethylchrysene isomer	dmCHR3	256	*46.44*
dimethylchrysene isomer	dmCHR4	256	*46.58*
dimethylchrysene isomer	dmCHR5	256	*46.74*
benzopyrene group			
benzo[b]fluoranthene	BbFLA	252	*46.98*

benzo[j]fluoranthene	BjFLA	252	*47.07*
benzo[k]fluoranthene	BkFLA	252	*47.37*
benzo[e]pyrene	BePYR	252	*47.94*
benzo[a]pyrene	BaPYR	252	*48.11*
perylene	PER	252	*48.41*
6-ring PAHs			
indeno[1,2,3-cd]pyrene	IPYR	276	*52.20*
benzo[ghi]perylene	BPER	276	*52.95*
dibenzoanthacene isomer	DBAx	278	*51.98*
dibenzo[a,h]anthracene	DBA	278	*52.40*
deuterated PAHs (internal standards)			
octadeutero-naphthalene	N-d8	136	*15.51*
decadeutero-anthracene	ANT-d10	188	*30.48*
decadeutero-pyrene	PYR-d10	212	*36.62*
dodecadeutero-chrysene	CHR-d12	240	*42.38*
hopanes			
C27 hopane (18α)	HO2718A	191	*49.13*
C27 hopane (17α)	HO2717A	191	*49.65*
C29 hopane (17α,21β)	HO29	191	*51.51*
C29 hopane (17β,221α) (moretane)	MO29	191	*52.11*
C30 hopane (17α,21β)	HO30	191	*52.61*
C30 hopane (17β,221α) (moretane)	MO30	191	*53.08*
C31 hopane (17α,21β) (22S)	HO3122S	191	*53.89*
C31 hopane (17α,21β) (22R)	HO3122R	191	*54.03*
C32 hopane (17α,21β) (22S)	HO3222S	191	*54.95*
C32 hopane (17α,21β) (22R)	HO3222R	191	*55.16*
sterenes			
cholestene	ST27a	215	*48.14*
cholestene (2-ene?)	ST27b	215	*48.50*
cholestene (2-ene?)	ST27c	215	*48.87*
cholestene	ST27d	215	*49.00*
methylcholestene	ST28a	215	*49.60*
methylcholestene (2-ene?)	ST28b	215	*49.95*
methylcholestene (2-ene?)	ST28c	215	*50.29*
methylcholestene	ST28d	215	*50.41*
ethylcholestene	ST29a	215	*50.81*
ethylcholestene (2-ene?)	ST29b	215	*51.16*

ethylcholestene (2-ene?)	ST29c	215	*51.51*
ethylcholestene	ST29d	215	*51.63*
cholestadiene (3,5?)	ST27::	368	*49.45*
C29 steradiene	ST29::	396	*52.08*
steranes			
C27 diasterane 13β,17α (20S)	D27S	217	*46.20*
C27 diasterane 13β,17α (20R)	D27R	217	*46.72*
C28 diasterane 13β,17α (20S)	D28S	217	*47.52*
C28 diasterane 13β,17α (20R)	D28R	217	*48.06*
C27 sterane 5α,14α,17α (20S)	S27AS	217	*48.41*
C29 diasterane 13β,17α (20S) & C27 sterane 5α,14β,17β (20R)	D29S+S27BR	217	*48.55*
C27 sterane 5α,14β,17β (20S)	S27BS	217	*48.65*
C27 sterane 5α,14α,17α (20R)	S27AR	217	*48.95*
C29 diasterane 13β,17α (20R)	D29R	217	*49.15*
C28 sterane 5α,14α,17α (20S)	S28AS	217	*49.72*
C28 sterane 5α,14β,17β (20R)	S28BR	217	*49.90*
C28 sterane 5α,14β,17β (20S)	S28BS	217	*50.01*
C28 sterane 5α,14α,17α (20R)	S28AR	217	*50.41*
C29 sterane 5α,14α,17α (20S)	S29AS	217	*50.81*
C29 sterane 5α,14β,17β (20R)	S29BR	217	*51.06*
C29 sterane 5α,14β,17β (20S)	S29BS	217	*51.13*
C29 sterane 5α,14α,17α (20R)	S29AR	217	*51.60*
OXYGENATED COMPOUNDS			
phenols			
phenol	F0	94	*9.46*
2-methylphenol	2mF	107	*11.85*
4- & 3-methylphenols	4m+3mF	107	*12.54*
2,6-dimethylphenol	26dmF	107	*13.29*
2-ethylphenol	2eF	107	*14.53*
2,4-dimethylphenol	24dmF	107	*14.80*
2,5-dimethylphenol	25dmF	107	*14.88*
4-ethylphenol	4eF	107	*15.40*
3-ethyl- & 3,5-dimethylphenols	3E+35dmF	107	*15.47*
2,3-dimethylphenol	23dmF	107	*15.67*
3,4-dimethylphenol	34dmF	107	*16.14*
vinylphenol	F2:	120	*16.88*
methoxyphenols (guaiacols - lignin pyrolysis markers)			
guaiacol	G0	124	*12.58*

methylguaiacol	G1	138	*15.92*
ethylguaiacol	G2	152	*18.49*
vinylguaiacol	G2:	150	*19.36*
vanillin	VAN	152	*21.20*
eugenol	G3:a	164	*20.63*
cis iso-eugenol	G3:b	164	*21.93*
trans iso-eugenol	G3:c	164	*22.97*
acetovallinone	AVAN	166	*23.48*
dimethoxyphenols (syringols - angiosperm lignin pyrolysis markers)			
syringol	S0	154	*20.16*
methylsyringol	S1	168	*22.76*
ethylsyringol	S2	182	*24.78*
vinylsyringol	S2:	180	*25.62*
syringaldehyde	Sald	182	*27.43*
prop-1-enyl syringol	S3:a	194	*26.55*
prop-2-enyl syringol (cis)	S3:b	194	*27.65*
prop-2-enyl syringol (trans)	S3:c	194	*28.73*
polysaccharide pyrolysis markers			
methylfurancarboxaldehyde (methylfurfural)	FCA1	110	*8.12*
2-furanmethanol (furfuryl alcohol)	Fol	98	*4.85*
methylfuranone/angelicalactone	Fone1	98	*6.79*
oxy-PAHs			
dibenzofuran	DBF	168	*24.54*
methyldibenzofuran	mDBFa	182	*27.08*
methyldibenzofuran	mDBFb	182	*27.38*
Phthalate plasticizers			
1,2-benzenedicarboxylic acid, dibutyl ester	Xa	149	*34.13*
1,2-benzenedicarboxylic acid,butyl phenylmethyl ester	Xb	149	*40.79*
1,2-benzenedicarboxylic acid, bis(2-ethylhexyl) ester	Xc	149	*44.36*
NITROGEN COMPOUNDS			
aliphatic nitrogen compounds			
C14 alkylnitrile	AN14	110	*28.86*
C16 alkylnitrile	AN16	110	*33.15*
C18 alkylnitrile	AN18	110	*37.11*
C14 alkylamide	AM14	59	*35.64*
C16 alkylamide	AM16	59	*38.23*

C18 alkylamide	AM18	59	*41.77*
n-dodecanamine, N,N-dimethyl	AA14	58	*25.11*
n-tetradecanamine, N,N-dimethyl	AA16	58	*29.71*
n-hexadecanamine, N,N-dimethyl	AA18	58	*33.87*
n-octadecanamine, N,N-dimethyl	AA20	58	*37.66*
one ring nitrogen compounds			
pyrrole	Pl	67	*<3*
2-methylpyrrole	2mPl	80	*4.35*
3-methylpyrrole	3mPl	80	*4.61*
C2-alkylpyrrole	Pl2	94	*7.04*
pyridine	Pd0	79	*<3*
methylpyridine	Pd1a	93	*3.90*
methylpyridine	Pd1b	93	*5.06*
benzonitrile	BCN0	103	*8.56*
benzeneacetonitrile	BCN1	117	*13.50*
benzenepropanenitrile	BCN2	131	*16.53*
two ring nitrogen compounds			
quinoline	Qu	129	*17.57*
isoquinoline	i-Qu	129	*18.14*
indole	Il0	117	*18.47*
methylindole	Il1	131	*21.03*
N-PAHs			
carbazole	CBZ	167	*31.24*
acridine	ACR	179	*30.61*
azapyrene isomer	NPYRa	203	*35.96*
azapyrene isomer	NPYRb	203	*37.27*
benzo[a]carbazole	BaCBZ	217	*42.36*
benzo[b]carbazole	BbCBZ	217	*43.07*
benzo[c]carbazole	BcCBZ	217	*43.26*
benzo[?]acridine isomer	BACRa	229	*41.52*
benzo[?]acridine isomer	BACRb	229	*42.19*
phenanthro[?]isoquinoline or isomer	PIQa	253	*46.33*
phenanthro[?]isoquinoline or isomer	PIQb	253	*46.70*
phenanthro[?]isoquinoline or isomer	PIQc	253	*47.64*
SULFUR COMPOUNDS			
dibenzothiophenes			
dibenzothiophene	DBT	184	*29.69*

methyldibenzothiophenes	DBT1		
4-methyldibenzothiophene	4mDBT	198	*31.85*
3- & 2-methyldibenzothiophenes	3+2mDBT	198	*32.25*
1-methyldibenzothiophene	1mDBT	198	*32.65*
dimethyldibenzothiophenes	dmDBT2	212	*34-35*
other sulfur compounds			
elemental sulfur	S8	256	*34.72*

Table 7. Compound names with corresponding codes used to represent peaks in chromatograms.